

Automated Daylighting Control System based on Sky Luminance Monitoring and Lighting Computing

Thèse N° 9498

Présentée le 3 mai 2019

à la Faculté de l'environnement naturel, architectural et construit
Laboratoire d'énergie solaire et physique du bâtiment
Programme doctoral en énergie

pour l'obtention du grade de Docteur ès Sciences

par

Yujie WU

Acceptée sur proposition du jury

Prof. D. Dujic, président du jury
Prof. J.-L. Scartezzini, Dr. J. H. Kämpf, directeurs de thèse
E. S. Lee, rapporteuse
Prof. J. Mardaljevic, rapporteur
Prof. J. Huang, rapporteur

2019

Acknowledgements

It has been truly fantastic to spend four years in Switzerland working on my doctoral studies and research in the surroundings of beautiful lakes and the magnificent Alps. I would like to give my warmest thanks to all the people without whom this thesis could not have achieved this level:

I am very grateful to my thesis supervisor Prof. Jean-Louis Scartezzini, who gave me the opportunity to work on shading systems and guided me throughout my doctoral studies. His trust and support have encouraged me to keep exploring my research field and to overcome many difficulties along my route.

Furthermore, I would like to thank Dr. Jérôme H. Kämpf, my thesis co-director, who offered a lot of insightful ideas and advices that helped me solve research problems. His rigorous attitude about research inspired me to improve the quality of my thesis.

I sincerely acknowledge the jury committee for reading the thesis and participating the examination: Prof. Drazen Dujic (Power Electronics Laboratory, EPFL), Prof. Jeffrey Huang (Media and Design Laboratory, EPFL), Eleanor S. Lee (Lawrence Berkeley National Laboratory), and Prof. John Mardaljevic (Loughborough University) .

I would like to thank Eleanor S. Lee particularly for hosting me during my four month visit to LBNL and for providing me with many inspiring suggestions, ideas, and feedbacks on my work.

My gratitude also extends to the Swiss Competence Center for Energy Research (SCCER FEEB&D) for providing funding for this project and to the Zeno Karl Schindler Foundation for providing financial support for my four month visit to LBNL as a visiting scholar.

Moreover, I should also thank Dr. Marek Krehel, Dr. Ran Xu, Lars Grobe, and Dr. Roland Shregle for their help and for providing a welcoming atmosphere during my short visit to Lucerne University of Applied Sciences and Arts (HSLU).

I am grateful to Greg Ward, Dr. David Geisler-Moroder, Dr. Tao Luo, and Dr. Jan de Boer for the inspiring and interesting discussions on lighting simulation during the IEA project.

Acknowledgements

I would like to thank Dr. Anothai Thanachareonkit for her kindness and hospitality during my visit to LBNL and Taoning Wang and Christoph Gehbauer for their help with experimental set-up in the 71t module.

I should also express my deep appreciation to my former professor and mentor Prof. Richard Syms at Imperial College London (ICL) who showed me the world of research and helped me develop good habits in conducting experiments before I came to EPFL.

It is my pleasure to thank all of my colleagues at LESO-PB and LIPID for providing me joy and help. Particular thanks go to Dasun Perera for having trips, sharing tasty hot pots, and offering extensive help on my publications, to Marta Benedetti for her support in the subjective study, to Peter Hanson for his kind-hearted help in Smart Living Lab, to Dr. Jan Wienold for discussions on visual comfort, and to Giorgia Chinazzo for sharing DEMONA. It is also a privilege and a sheer joy to have worked with and shared time with Jing Gong, Dan Assouline, Olivia Bouvard, Fleury Jérémy, Anna Krammer, Alina Walch, Silvia Coccolo, Pietro Florio, André Kostro, Dasaraden Mauree, Ali Motamed, Govinda Upadhyay, and Dr. Andreas Schueler.

Moreover, I would like to thank Marlène Muff for helping me arrange comfortable accommodations and flights for conferences, Barbara Smith for providing professional English editing of my thesis and publications, Pierre Loesch for helping me with my experimental set-up and fabrication of many components with 'Swiss quality', Laurent Deschamps for technical support, Claude-Alain for his technical help in the Smart Living Lab, and Dr. Friedrich Linhart and Dr. André Catana for their support in filing patents.

Many warm thanks to my friends in EPFL and ICL for the wonderful journeys, providing support, and sharing cheerful moments together: Jun Ma, Chongqi Yu, Hezhi Zhang, Wei Liu, Chao Liu, Wenjiao Xie, Xifan Tang, Hao Zhuang, Ya Wang, Hengjie Xu, Jun Lu, Yi Hu, Su Li, Xuan Su, Guangbin Dou, Zongxiang Wu, Dixi Liu, Mingyang Sun, Cheng Chen, Yilun Zhou, Shuo Yang, and Chen Wang. Particular thanks go to Chen Yang for his whole-hearted help in debugging FPGA.

Words are not enough to express my gratitude to my beloved parents and grandparents for their care and encouragement, to my aunt and my cousin Minghao Gu for their whole-hearted support during my most difficult times, and to my girl friend Bin Ding for accompanying me on many fabulous journeys and her unwavering support.

Lausanne, 26 Feb. 2019

Yujie Wu

Abstract

Sufficient daylight exposure contributes to occupants' well-being, productivity and health in buildings. However, excessive sunlight ingress induces discomfort glare and increases the cooling load in warm seasons. The performance of manual shading systems is limited by users' low interaction frequency. Since sky conditions are dynamic, frequent adjustments are necessary, but these are impractical for users to manage. Various shading automation systems have been proposed to better foster the utilization of daylight in buildings, the performance of which is limited by a number of factors, including insufficient glare protection, disturbing movement of slats, privacy issues, and commissioning difficulty. In this thesis, an integrated daylighting control system is proposed and demonstrated to regulate daylight in buildings. Based on real-time lighting computation with the monitored luminance distribution of the sky and landscape the proposed system is fully decentralized.

First, an embedded photometric device (EPD) was designed and validated, showing improved accuracy in daylighting simulation, compared to using standard sky models. The EPD is composed of an image sensor and a microprocessor. After calibration, the spectral response of the imaging system is close to the photopic luminosity function $V(\lambda)$, achieving a 8.9% spectral correction error. The luminance detection range spans $1.2 \times 10^2 \sim 3.78 \times 10^9 \text{ cd/m}^2$, covering extremes of both the shadowing landscape and the sun orb luminance. The EPD monitors the luminance distribution of the sky vault and the ground fraction. Based on the generated luminance map, the EPD is able to perform on-board lighting computing. The performance of work-plane illuminance (WPI) simulation was cross validated with a lux-meter array in a daylighting test module under different sky conditions achieving a mismatch of below 10%.

Secondly, since the bidirectional distribution function (BTDF) commonly used in daylighting simulation involves bulky data, a compression scheme based on planar wavelet transform was investigated and generic error and the influence on daylighting simulation were studied at various compression ratios. Results showed that both WPI and daylight glare probability (DGP) are relatively immune to a BTDF compression ratio below 100.

Thirdly, an automated Venetian blind was designed which integrates the EPD both as a sensing unit and a controller based on real-time lighting simulation. The EPD determines an optimal shading position according to the simulation results, to offer sufficient WPI, mitigate excessive solar heat gain (SHG), temper discomfort glare, and maximize outwards view. 'In-situ'

Acknowledgements

experiments demonstrated that the automated Venetian blinds were able to regulate WPI in an efficient way. The expected reduction of cooling loads due to SHG was estimated to reach 47% compared to no shading protection in warm seasons. It was also demonstrated to mitigate discomfort glare timely, including veiling glare from surroundings. A subjective study conducted with 34 subjects showed satisfaction with regulated daylight provision, glare mitigation, and quietness of slat movement.

Finally, the EPD was used to control tint states of a split-pane electrochromic (EC) window to secure occupants' visual satisfaction. Experimental results in a full-scale testbed showed that the WPI was controlled within the confined range with regulated daylighting under clear skies 83% of time and the DGP 95% of the time; under partly cloudy skies, the WPI was within the range 62% ~ 68.2% of the time and for the DGP 85% ~ 94% of the time to achieve visual comfort.

Keywords: Automated shading, Electrochromic glazing, BTDF, HDR, Visual comfort, Discomfort glare, Decentralized system, Open-loop control, Sky luminance map

Résumé

Une exposition suffisante à la lumière naturelle contribue au bien-être, la productivité et la santé des occupants dans les bâtiments. Cependant, un excès de lumière naturelle peut provoquer un éblouissement gênant et augmente le besoin en refroidissement dans les climats chauds. Les performances des protections solaires manuels sont limitées par la faible fréquence d'interaction des utilisateurs. Les conditions du ciel étant dynamiques, de fréquents ajustements sont nécessaires, mais ils ne sont pas pratiques pour les utilisateurs. Différents systèmes automatiques de protection solaire ont été proposés en vue d'une meilleure utilisation de la lumière naturelle dans les bâtiments, dont les performances sont limitées par un certain nombre de facteurs, notamment une protection insuffisante contre l'éblouissement, des mouvements gênants des lames, des problèmes de confidentialité et des difficultés de mise en service. Dans cette thèse, un système intégré de contrôle de l'éclairage naturel est proposé et mis en oeuvre en vue de réguler la lumière naturelle dans les bâtiments. Basé d'un calcul en temps réel de l'éclairage naturel dans un local réalisé à partir de la distribution de luminance du ciel, le système proposé est parfaitement indépendant et décentralisé.

Un dispositif photométrique intégré (DPI) a ainsi été conçu et mis en oeuvre, offrant précision supérieure de la simulation de l'éclairage naturel par rapport aux modèles de ciel. Le DPI est composé d'un capteur imageur numérique et d'un microprocesseur. Après calibration, la réponse spectrale du système d'imagerie est proche de la fonction de luminosité photopique $V(\lambda)$ et caractérisé par une erreur de correction spectrale de 8,9%. La plage de détection de luminance s'étend de 1.2×10^2 à 3.78×10^9 cd/m², couvrant les extrêmes du depuis l'ombre jusqu'à la luminance du disque solaire. Le DPI mesure la distribution en luminance de la voûte céleste et du sol. Sur la base de le champ de de luminance mesuré, le DPI est capable d'effectuer par lui-même des calculs d'éclairage naturel. Les performances de la simulation de l'éclairage sur le plan de travail (EPT) ont été comparées avec un réseau de lux-mètres placé dans un module d'expérimentation en éclairage naturel en vraie grandeur pour différentes conditions de ciel, avec une précision supérieure à 10%.

Deuxièmement, étant donné que la fonction de distribution de transmission bidirectionnelle (BTDF) couramment utilisée dans la simulation d'éclairage naturel nécessitant un important volume de données, un procédé de compression basé sur la transformation en ondelettes planes a été pris en compte, ainsi que son erreur générique et son influence sur la simulation d'éclairage diurne à différents taux de compression. Les résultats montrent que l'EPT et la

Acknowledgements

probabilité d'éblouissement dû à la lumière naturelle sont relativement immuables avec un taux de compression de la BTDF inférieurs à 100.

Troisièmement, un store vénitien autonome a été conçu, qui intègre le DPI à la fois comme unité de détection et contrôleur, basé sur une simulation d'éclairage naturel en temps réel. Le DPI détermine une position de stores optimale en fonction de la simulation numérique afin d'offrir une valeur d'EPT suffisante, d'empêcher un gain de chaleur solaire excessif (GCS), de limiter les reflets gênants et de maximiser la vue vers l'extérieur. Des campagnes de mesure "in situ" ont démontré que les stores vénitiens automatisés étaient capables de réguler efficacement l'EPT. La réduction des gains solaires, conduisant à des besoins inutiles en climatisation, a atteint 47%. Il a également été démontré que l'atténuation de l'éblouissement d'inconfort, y compris l'éblouissement causé par les réflexions totales des environs, était également atténuée. Une campagne d'études menée auprès de 34 sujets a montré une satisfaction vis-à-vis de la lumière naturelle ainsi régulée, de la prévention de l'éblouissement et du mouvement imperceptible des lamelles.

Enfin, le DPI a été appliqué pour contrôler le facteur de transmission d'un vitrage électrochromique (EC) afin de garantir le confort et la performance visuelles des occupants. Un suivi expérimental réalisé sur un module d'essai en lumière naturelle en vraie grandeur ont montré que l'EPT se situait dans la plage de confort avec un éclairage naturel régulé par temps clair 83% du temps et pour le DGP 95% du temps; sous un ciel partiellement nuageux, le WPI était confortable entre 62% et 68% du temps et le DGP entre 85% et 94% du temps.

Mots clés : Ombrage automatisé, Électrochrome, BTDF, HDR, Confort visuel, Éblouissement

Nomenclature

Physical variables of light beam

λ	Wavelength of light	nm
Δt	Integration time	s
E_i	Irradiance of incident beam	W/m^2
E_{av}	Average horizontal illuminance	lux
f'_1	Spectral correction error	
f_t	Bi-directional transmittance distribution function	
gl	Uniformity factor	
L_t	Radiance of exiting beam	$W \cdot sr^{-1} \cdot m^{-2}$
L	Luminance measured by a detector	cd/m^2
S_l	Spectral response of illuminant	
S_n	Normalized spectral response of the detector	
S	Relative spectral response of the detector	
$V(\lambda)$	Photopic luminosity function	
ϕ_i	Azimuth angle of incident beam	
ϕ_t	Azimuth angle of exiting beam	
θ_i	Zenith angle of incident beam	
θ_t	Zenith angle of exiting beam	

Matrices in lighting calculation

C_{ds}	Solar coefficient matrix	sr
D	Daylight matrix	
i_{wp}	Work-plane illuminance vector	lux
s	Sky vector	cd/m^2
s_{sun}	Direct sun vector	cd/m^2
T	Transmission matrix	

Nomenclature

V View matrix sr

Variables in wavelet transformation

$\hat{\phi}_k$ Dual scaling basis function
 $\hat{\psi}_m$ Dual wavelet basis function
w Coefficient vector
 ϕ_k Scaling basis function
 ψ_m Wavelet basis function
u Parameter for quantization
v Parameter for quantization
x Continuous signal in Hilbert space

Other acronyms

ℓ_2 Hilbert vector space
 L_2 Hilbert function space
AC Alternating current
ADC Analog-to-digital converter
B&W Black and white
Bior6.8 Bi-orthogonal basis 6.8
BTDF Bi-directional transmittance distribution function
CCD Charge-coupled device
CDF9.7 Cohen-Daubechies-Feauveau basis 9.7
CFS Complex fenetration system
CIE International Commission on Illumination
CMOS Complementary metal oxide semiconductor
CR Compression ratio
DB10 Daubechies basis 10
DC Direct current
DGI Daylight glare index
DGI_N New daylight glare index
DGP Daylight glare probability
DMA Direct memory access
DSLR Digital single-lens reflex
EC Electrochromic
EPD Embedded photometric device

EPFL	École Polytechnique Fédérale de Lausanne
ERS	Electronic rolling shutter
EVB	External Venetian blind
FOV	Field of view
FPGA	Field programmable gate array
GPIO	General purpose input/output
HDL	Hardware description language
HDR	High dynamic range
HID	High intensity discharge
HPS	Hard core-processor
IO	Input/output
LBNL	Lawrence Berkeley National Laboratory
LED	Light-emitting diode
LT	Local time
MPU	Micro-processing unit
ND	Neutral-density
NIR	Near infra-red
PCB	Printed circuit board
PV	Photovoltaic
RGB	Red green blue
RLC	Rolex learning center
RMSE	Root mean square error
SDRAM	Synchronous dynamic random access memory
SHG	Solar heat gain
SHGC	Solar heat gain coefficient
SoC	System on-chip
SR	Glare subjective rating
SSL	Solid-state lighting
TE	Transmittance error
UGR	Unified glare rating
VCP	Visual comfort probability
WPI	Work-plane illuminance

Contents

Acknowledgements	iii
Abstract (English/Français)	v
Nomenclature	ix
List of figures	xv
List of tables	xix
1 Introduction	1
1.1 Daylight and buildings	1
1.2 Shading devices and switchable glazing	4
1.3 Problem statement	6
1.4 Thesis structure	7
2 State-of-the-art	11
2.1 Limitation of sky models	11
2.2 Image sensors used in luminance monitoring	12
2.3 BTDF data compression	14
2.4 Shading automation	17
2.5 Electrochromic glazing control	20
2.6 Research questions	22
3 Embedded photometric device	23
3.1 Introduction	23
3.2 Device Architecture	24
3.2.1 Image sensor	24
3.2.2 FPGA processor	25
3.2.3 Lens and actuator	26
3.3 Calibration procedure	27
3.3.1 Spectral response	27
3.3.2 Vignetting	32
3.3.3 Response curve	34
3.4 Empirical validation	37

Contents

3.4.1	Image rendering	38
3.4.2	Work-plane illuminance	39
3.4.3	Solar tracking	51
3.5	Conclusion	52
4	Wavelet compression on BTDF data	55
4.1	Introduction	55
4.2	Methodology	55
4.3	Compression on medium-resolution BTDF data	58
4.3.1	BTDF generation	58
4.3.2	Performance assessment	60
4.4	Compression on high-resolution BTDF data	66
4.5	Conclusion	69
5	Automated Venetian blinds	71
5.1	Introduction	71
5.2	Design of automated EVB	72
5.2.1	Embedded photometric device (EPD)	72
5.2.2	Shading actuator	73
5.3	Methodology and control algorithms	74
5.3.1	Modelling and experimental set-up	74
5.3.2	BTDF data generation	75
5.3.3	Simulation method	76
5.3.4	Control algorithm	78
5.4	Empirical validation	81
5.4.1	Cross validation	81
5.4.2	EVB control	83
5.4.3	Veiling glare	91
5.5	Survey on users' satisfaction	93
5.6	Commissioning issues	97
5.7	Conclusion	101
6	Automated electrochromic glazing	105
6.1	Introduction	105
6.2	Design	105
6.2.1	Systematic set-up of the automated EC glazing	105
6.2.2	Embedded photometric device (EPD)	106
6.3	Methodology	107
6.3.1	Daylighting testbed	107
6.3.2	Daylighting simulation	109
6.3.3	Control logics	112
6.4	Empirical validation	115
6.4.1	Cross comparison	115

6.4.2 EC glazing control	117
6.5 Discussion	125
6.6 Conclusion	126
7 Conclusion	129
7.1 Main achievements	129
7.1.1 Embedded photometric device	129
7.1.2 BTDF compression	130
7.1.3 Automated Venetian blinds	130
7.1.4 Automated EC glazing	131
7.2 Perspectives of application	132
7.3 Future outlook	133
A Appendix A	135
A.1 Plans of the daylighting test module (DEMONA)	135
A.2 Questionnaire on visual satisfaction	137
B Appendix B	139
B.1 Daylighting regulation by the automated EVB	139
B.1.1 Clear sky	139
B.1.2 Partly cloudy/clear sky	140
B.1.3 Partly cloudy/overcast sky	143
B.1.4 Overcast	144
B.2 Daylighting regulation by the automated EC glazing	147
B.2.1 Clear sky	147
B.2.2 Partly cloudy/clear sky	148
B.2.3 Partly cloudy/overcast sky	151
References	153
Curriculum Vitae	167

List of Figures

1.1	Highly glazed buildings	2
1.2	Various shading devices	4
1.3	Venetian blinds kept closed under overcast skies	5
1.4	Buildings using electrochromic window [1]	6
2.1	Partly cloudy skies	12
2.2	Camera used as apparatus to monitor spatial luminance distribution	14
2.3	Transforms involved in BTDF compression	17
2.4	A ceiling mounted photo-sensor for shading control [2]	18
2.5	Two approaches in control of tilt angles of Venetian blinds	19
3.1	RGB Bayer pattern of the pixel arrangement of the image sensor	24
3.2	Modules configured in the FPGA chip and connections with external elements	26
3.3	Field of view (FOV) of the imaging system	26
3.4	Protection mask for the imaging system	27
3.5	Experimental calibration set-up	28
3.6	Diagram of experimental set-up	28
3.7	Spectral response of the RGB channels of the image sensor	29
3.8	Spectral transmittance distribution of the color filters	30
3.9	Spectral response of the RGB channels after optical corrections	31
3.10	Synthesised spectral response of the imaging system	32
3.11	Diagram of experimental set-up	33
3.12	Surface of response attenuation due to vignetting	33
3.13	Fitted curve for vignetting effect	34
3.14	Diagram of experimental set-up	35
3.15	Response of RGB channel versus luminance at 6 shutter speed	36
3.16	Luminance monitoring by the calibrated imaging system and its error distribution	37
3.17	Rendering of a office room by a) Perez model b) HDR imaging based sky luminance map	39
3.18	The daylighting test module with unilateral façades (DEMONA)	40
3.19	Sensor position for monitoring horizontal illuminance	41
3.20	Employed equipments and their feature in experiments	41
3.21	The embedded photometric device positioned in front of the unilateral façade	42

List of Figures

3.22	Workplane horizontal illuminance assessed by two daylighting simulation methods compared with lux-meter values for a pre-dominant overcast sky [3]	43
3.23	Relative error of the 5 computed workplane illuminances compared with lux-meter values for a pre-dominant overcast sky [3]	44
3.24	Workplane horizontal illuminance assessed by two daylighting simulation methods compared with lux-meter values for a predominant clear sky [3]	46
3.25	Relative error of the 5 computed workplane illuminances compared with lux-meter values for a predominant clear sky [3]	47
3.26	Workplane horizontal illuminance assessed by two daylighting simulation methods with lux-meters values for a clear sky	49
3.27	Relative error of the 5 computed workplane illuminances compared with lux-meter values for a clear sky	50
3.28	Solar luminance and position monitored by embedded photometric device	52
4.1	BTDF data compression routine based on wavelet transform	57
4.2	CFS panels with different light transmitting behaviour	58
4.3	CCD imaging based Gonio-photometer	59
4.4	Photometric solids of BTDF data of the five samples	60
4.5	RMSE and TE at compression ratio 20	62
4.6	RMSE and TE at various compression ratios of Lumitop	63
4.7	Floor plan of an office room	63
4.8	Image rendering of daylighting in an office at various compression ratios	64
4.9	Uniformity factor g_1 and average horizontal illuminance E_{av} on the desk	65
4.10	Daylight glare probability (DGP) and its relative error	66
4.11	Compressed BTDF data of EVB	67
4.12	Set-up in a daylighting test module	68
4.13	Simulated work-plane illuminance at various compression ratio (CR)	69
5.1	Design of the automated 'Eye-sight' Venetian blinds	73
5.2	Daylighting test module with automated 'Eye-sight' EVB	74
5.3	Diagram of experimental set-up for shading control	75
5.4	Mapped BTDF of EVB at 72° slat tilt angle	76
5.5	Mapped BTDF of EVB at 32° slat tilt angle	76
5.6	Floor-plan showing defined work-plane position and view directions	79
5.7	Flow chart of control process on EPD	80
5.8	Cross validation set-up with a reference camera	81
5.9	Simulated HDR view images by the EPD	82
5.10	Captured HDR view images by the reference camera	82
5.11	Simulated variables by the EPD compared with reference values	83
5.12	Set-up of lux-meter sensors to monitor WPI as reference	84
5.13	WPI and DGP with/without automated EVB (summer, clear sky)	86
5.14	WPI and DGP with/without automated EVB (autumn, clear sky)	87
5.15	WPI and DGP with/without automated EVB (summer, partly cloudy sky)	89

5.16	Time fraction of WPI satisfying the constraint [500, 2000] lux achieved by automated EVB compared with no shading protection under various sky conditions	90
5.17	Reduced WPI ratio during summer time	90
5.18	Set-up of a curved mirror inserted manually as the glare source	91
5.19	Automated EVB blocking veiling glare from environment (interior view)	92
5.20	Measured WPI and simulated DGP in the module	93
5.21	Subjects evaluating performance of the automated shading system	94
5.22	Survey results on visual satisfaction	95
5.23	Simulated horizontal illuminance employing the same reflectance for each interior surface	99
5.24	Deviation of horizontal illuminance versus reflectance of scene interior	100
5.25	Simulated DGP employing the same reflectance for each interior surface	101
6.1	Design of an EC glazing integrated with an EPD (view from the outdoors towards the glass surface)	106
6.2	A daylighting testbed with three parallel offices	108
6.3	Experimental set-up	109
6.4	Tone mapped image of the BTDF matrix of EC glass at 18% transmittance	112
6.5	Flowchart of each EPD run in EC glass control	114
6.6	Parallel experiments assessing EC glazing control	115
6.7	WPI and DGP with EC glazing at 18% transmittance	116
6.8	View images with EC glazing at 1% (upper) and 6% (lower) transmittance	117
6.9	WPI with EC glazing controlled by different method (clear sky)	119
6.10	DGP with EC glazing controlled by different methods (clear sky)	120
6.11	WPI with EC glazing controlled by different methods (thin clouds)	121
6.12	DGP with EC glazing controlled by different methods (thin clouds)	122
6.13	WPI with EC glazing controlled by different methods (partly cloudy)	123
6.14	DGP with EC glazing controlled by different methods (partly cloudy)	124
6.15	Rapid motion of clouds (captured in Room A)	126
A.1	Floor plans of the daylighting test module (DEMONA)	136
B.1	WPI and DGP with/without automated EVB on Jan. 15, 2019 (winter, clear sky)	140
B.2	WPI and DGP with/without automated EVB on Jul. 12, 2018 (summer, partly cloudy/clear sky)	141
B.3	WPI and DGP with/without automated EVB on Sept. 07, 2018 (autumn, partly cloudy/clear sky)	142
B.4	WPI and DGP with/without automated EVB on Jan. 19, 2019 (winter, partly cloudy/clear sky)	143
B.5	WPI and DGP with/without automated EVB on Sept. 03, 2019 (autumn, partly cloudy/overcast sky)	144
B.6	WPI and DGP with/without automated EVB on Jan. 06, 2019 (winter, overcast sky)	145
B.7	WPI and DGP with/without automated EVB on Jan. 07, 2019 (winter, overcast sky)	146
B.8	WPI with EC glazing controlled by different method on Oct. 25, 2018 (clear sky)	147
B.9	DGP with EC glazing controlled by different methods on Oct. 25, 2018 (clear sky)	148
B.10	WPI with EC glazing controlled by different method on Oct. 26, 2018 (Partly cloudy/clear sky)	149
B.11	DGP with EC glazing controlled by different methods on Oct. 26, 2018 (Partly cloudy/clear sky)	150
B.12	WPI with EC glazing controlled by different method on Oct. 28, 2018 (Partly cloudy/overcast sky)	151
B.13	DGP with EC glazing controlled by different methods on Oct. 28, 2018 (Partly cloudy/overcast sky)	152

List of Tables

3.1	Optimized coefficients	34
4.1	Compression ratio of BTDF data and relative average error	67
5.1	Dimension of pre-computed matrices in the matrix algebraic approach	78
5.2	Reflectance and specularity of surface material in modelled scene	98
6.1	Property of the EC glass at four tint states	108
6.2	Ratio of time regarding WPI and DGP within constraints	125

1 Introduction

1.1 Daylight and buildings

As global energy consumption is rapidly growing [4, 5], environmental pollution and global warming have in many ways catalysed the campaign of energy savings all around the world [6]. Among the many energy consuming domains, the building sector is responsible for over 30% of the global energy consumption and nearly 40% of CO₂ emissions in 2017 [7, 8]. Lighting is one of the leading consumers representing 10%-35% of the energy demand in commercial buildings [9, 10, 11], despite the high electricity saving potential offered by efficient luminaires and exploitation of daylight [12, 13, 14, 15, 16]. It is also estimated that 30% of cooling energy is used to offset excessive solar heat gain (SHG) through windows in buildings in the United States [17].

The technology of solid-state lighting (SSL) has improved the energy efficiency and life span of luminaires with enhanced luminous efficacy. Code requirements on light sources have further promoted the diffusion of SSL luminaires with energy-efficient electronics [18] to gradually replace relatively inefficient incandescent and fluorescent lamps. In addition, recent progress in research and development of smart lighting systems based on a human centric approach [19] as well as the Internet of Things (IOT) have further confirmed their energy-saving potential in artificial lighting [20, 21]. Nonetheless, it has been revealed in studies that daylight, as a ubiquitous cost-economical light source, cannot be fully substituted by current technology of artificial lighting, not only due to its unique spectral power distribution [22] but also because of its non-visual effects on occupants' physiology, behaviour and circadian rhythms [23, 24, 25], which indirectly influence their health [26, 27] and performance [28]. Within developed economies, such as in Europe and North America, people spend 90% of their time on activities and in environments relying on artificial lighting [29, 30]. Therefore, increasing the daylight provision in buildings has been a growing concern for building designers and researchers.

Chapter 1. Introduction

To meet current concerns regarding energy savings, environment protection and global climate change, solar radiation, as a free and clean energy source, is exploited increasingly in residential, commercial, and industrial applications [31]. Daylight has a significant energy saving potential in the context of both building illumination, space heating and cooling load. The building envelope as a separator of indoor and outdoor environment is a key factor that determines quality and control of indoor conditions. Fenestration, primarily windows, is essentially an opening in a building envelope that connects inside and outside and allows daylight penetration into buildings. The past decades have witnessed a growing application of glazed façades in modern architecture especially in high-rise buildings, an example of which is shown in Figure 1.1 a) (downtown of a medium-sized Chinese city). Although highly glazed façades provide exterior views to occupants and simultaneously mitigate artificial lighting by admitting daylight inside buildings, daylight utilization can contradict the energy saving objective if it is not harnessed smartly. During warm seasons, large solar heat gain induced by excessive ingress of sun light can contribute to a substantial upsurge in the cooling load of buildings [32] and can also cause discomfort glare in the visual field of occupants [33]. Once visual comfort is disturbed by glare under direct sunlight, occupants tend to keep shading closed and to be reluctant in reopening it [34], even if the disturbance has passed. The example of the 860-880 Lake Shore Drive building, as presented in Figure 1.1 b), illustrates the problem that most of the white curtains are fully closed under a clear sky to prevent discomfort glare from the sun, and artificial luminaires are switched on to provide sufficient lighting in the building interior for office workers [35].



(a) Down-town of Guiyang, China

(b) 860 Lake Shore Drive, Chicago

Fig. 1.1. Highly glazed buildings

Daylight is generally regarded as an under exploited resource in commercial buildings. Studies have shown that an optimal utilization of daylight can not only save 25%-60% of lighting related energy [13, 36] but can also improve occupants' visual comfort substantially [37, 38]. The recent prolific research on visual comfort [39, 40] and non-image forming effects of light [41, 42] has gradually unveiled the mechanism of the daylight influence on human's health

and productivity [43], largely contributed by its unique spectral power distribution [44] and periodic variation between day and night. Since occupants' visual comfort has a positive impact on their productivity [43], several studies have estimated that corresponding savings through visual comfort enhancement, when projected onto staffs' salaries and benefits, can exceed energy bills in office buildings [45, 46, 47, 48].

Although comfort and satisfaction are subjective notions, norms and metrics have been developed and established to quantify and assess visual quality from daylight provision and discomfort glare perspectives. The European standard on lighting (EN 12464-1) [49] imposes minimum illuminance requirements for a given task area for different indoor activities: 500 lux for reading, typing and writing tasks, 1000 lux for quality control and inspection, 1500 lux for precise manufacturing including electronic adjustment and watch making; etc. Moreover, the recent European standard on daylighting of buildings (EN 17037) [50] has included a rating of assessing the outwards view for occupants, as another factor influencing occupants' visual satisfaction. In quantifying discomfort glare, although vertical illuminance at an eye position can be used as a basic measure, studies have shown vertical illuminance alone is insufficient for evaluating discomfort glare which is also strongly associated with luminance contrasts inside the visual field [51, 52]. Over the past decades, multiple glare metrics have been formulated for the assessment of glare risk taking luminance contrast as a major factor as a result of experimental studies and subjective evaluations, including the Daylight Glare Probability (DGP) [53] and the Daylight Glare Index (DGI) [54] for daylit space, and the Unified Glare Rating (UGR) [55] and the Visual Comfort Probability (VCP) [56] for an electric lighting environment. The DGI tends to overestimate glare under real sky conditions [57] and neglects the effect of non-uniform window luminance [58]. The DGP was proposed by Wienold et al. [53] to overcome this drawback. In spite of its limitation under overcast sky conditions and overestimation of glare when the sun is in the field of view (FOV) of occupants [59, 60], the DGP has been validated as a relatively reliable metric in a number of studies for assessing glare risk in a daylit space [61, 62, 63, 64], which is correlated with observers' extent of dissatisfaction, including imperceptible, perceptible, disturbing, and intolerable levels. These norms and metrics have paved the way for researchers and lighting designers to improve occupants' visual satisfaction.

However, regulating daylight flux to provide visual comfort for occupants remains a difficult task. The main reason lies in the fact that daylighting is dynamic and subject to the variation of sun positions, atmosphere clearness, and cloud density, distribution, and motion. Within minutes, the outdoor daylight condition can change drastically due to rapid motion of clouds, occluding the sun or moving away, which leads to substantial fluctuations of daylight availability and glare risk in a building interior.

1.2 Shading devices and switchable glazing

Window shades, including overhangs, awnings, roller blinds, and Venetian blinds [65], are commonly used in conjunction with façades to moderate excessive ingress of daylight, as shown in Figure 1.2. According to their mechanic structure, shading devices can be categorized into fixed and operable ones. Although fixed shading devices suffer relatively less from maintenance issues, operable window shades outperform them in tuning daylight transmission and in glare control in the context of hourly and even minute-by-minute variations of sky conditions [66]. Among various operable shading devices including roller blinds, shutters, etc., Venetian blinds are popular for application in buildings, since they can not only regulate daylight injection, but also preserve outwards views and privacy for users due to their two degrees of freedom (vertical position and tilt angle of slats) in adjustment.



Fig. 1.2. Various shading devices

Venetian blinds have existed for quite a long period of time. The early history of Venetian blinds is still elusive. Nonetheless, archaeology findings suggest that the curtain reeds were used in ancient Egypt and Persia, due to their merit of controlling glare from the sun without obstructing cooling air flow. Early Venetian travellers and traders possibly brought the idea of blinds from Persia back to Venice and then developed the early model of Venetian blinds. During the 19th century, Venetian blinds gained significant popularity in the western world. In recent decades, the improvement of the design and manufacturing process has triggered a renaissance of their world-wide prevalence [69]. In addition to their application in domestic

1.2. Shading devices and switchable glazing

dwellings, Venetian blinds have been commonly adopted in office buildings, factories, hospitals, hotels, restaurants, school buildings, etc., to regulate daylighting.

A Venetian blind is mainly composed of a group of parallel slats (e.g. aluminium slats) suspended by pairs of strings connected to tilting gears, making the slats adjustable in both vertical position and inclination angle. In such a way, the optical property, regarding light transmittance, of a Venetian blind is fundamentally subjected to the movement of the set of slats, with versatility of modulating sun-rays by means of directing, reflecting or diffusing, based on its retractable position and adjustable tilt angle. Depending on whether placed outside or inside a building envelope, Venetian blinds can be categorized into external and internal ones. External Venetian blinds (EVB) are more efficient and feature a higher dynamic range in tuning the SHG ($g\text{-value} \geq 0.01$) than interior ones ($g\text{-value} \geq 0.25$) [70], since interior blinds admit SHG into the work space. Despite their adjustment flexibility, the complex optical properties of Venetian blinds in daylight transmission make it difficult for occupants to manipulate them precisely. As a result, Venetian blinds are commonly kept at the same position for a long time. A study performed by Paule et al. showed that occupants' average frequency in using shading is no more than 1.7 movement per week [71] in a building at the EPFL Science Park, which contributes to the low performance of blinds in general with insufficient daylight provision in buildings. The BC building in Lausanne, as presented in Figure 1.3, also illustrates the issue. The majority of EVBs remain closed even under overcast skies when outdoor daylight availability is low, and occupants rely on artificial light to work.

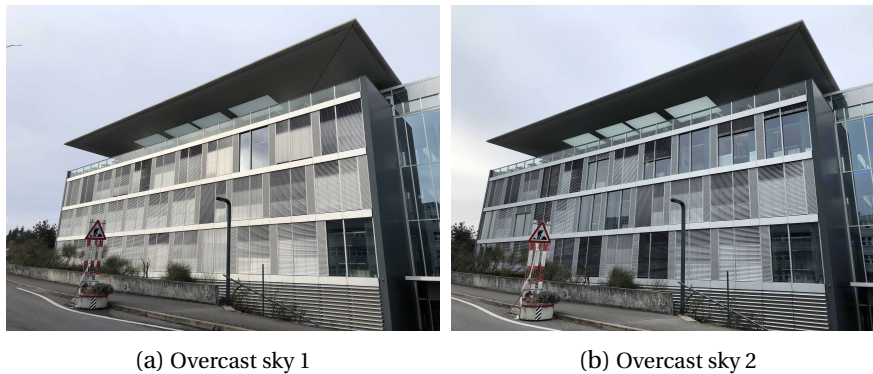


Fig. 1.3. Venetian blinds kept closed under overcast skies

While exterior shading devices have low heat gain and are relatively inexpensive to manufacture [72], switchable glazing, with a variable transmittance between clear and dark extremes, can not only control the luminous environment but also preserve exterior views for occupants, which has less installation, durability, and maintenance issues [73]. Switchable glass has been used as an alternative for regulating daylighting in highly glazed office buildings, to improve energy saving and visual comfort. According to the agents used to vary its transmittance, switchable glazing is categorized into four distinct types: electrochromic (applied voltage), gasochromic (pumped gas), photochromic (incident ultraviolet radiation), and ther-

mochromic (temperature). Both photochromic and thermochromic glazing are basically passive devices that react to ambient variation. The corollary of passive glass is the lack of control to offer an optimal luminous environment simply based on localised temperature or incident illuminance on a window surface. Electrochromic glass and gasochromic glass are active, i.e. they can be controlled according to sensors' output and can provide responsive modulation of the thermal and optical property of glazed façades to optimize lighting, visual comfort, and reduced peak cooling load. Although gasochromic glazing features a high switching speed, its installation complexity with gas inlet limits its practical application in buildings compared to electrochromic glazing with relatively straightforward installation [74]. With its technological advances, electrochromic (EC) glazing, which can modify its visual transmittance under an applied low voltage, has been a commercial product for some time and features multiple merits for building application, including a high modulation range of light transmittance, low driving voltage, and clear view in all tint states [75], as compared to crystal liquid and suspended particle devices. An electrochromic glazing, considered with user acceptance, should have a large luminous transmittance ($\geq 60\%$) in the clear state, appearing as a conventional glass for daylight harvesting and view outwards, and have a low transmittance ($\leq 2\%$) in the full tint state to temper discomfort glare especially from direct sun light [76, 77]. Research is carried out to further expand the transmittance variable range and to accelerate the switching speed of EC glass [78].



Fig. 1.4. Buildings using electrochromic window [1]

1.3 Problem statement

Although shading systems and switchable glazing have offered means to control daylight, their actual performance is largely limited by users' manual control and behaviour [79]. Survey studies have shown that users commonly hesitate to reopen shading once blinds have been pulled down [80], and their average frequency in interacting with manually controlled shading is no more than 1 time per day [81], which contributes to the low performance of manual shading in general and prevents sufficient daylight provision in buildings. Since daylight can change very rapidly in both its intensity and direction during one day, it is impractical for

occupants to constantly manipulate shading devices according to the varying sky conditions, while simultaneously performing their own tasks.

The problem that this thesis aims to address is the contradiction between variable daylighting in buildings and occupants' visual satisfaction. Therefore, the objective of this thesis is to design and demonstrate an automated daylighting control system that can secure sufficient daylight provision, mitigate excessive solar heat gain in buildings, temper occupants' discomfort glare, and maximize their outside view. A highly integrated daylighting control system is proposed based on real-time luminance monitoring of the sky and lighting computing for building interiors to offer an optimal daylit environment. In addition to the focus on systematic performance, the thesis also aims at overcoming the limitation of conventional daylighting control systems, considering factors of installation and commissioning complexity to enhance users' acceptance.

1.4 Thesis structure

The structure of the thesis is organized as follows:

Chapter 2 is comprised of five sections, each of which shows the state-of-the-art on a specific subject that the thesis is to address in the following chapters. First of all, Section 2.1 elaborates the limitation of commonly used sky luminance models in lighting simulation especially in resolving local climate and cloud distributions when the time scale is at minute level. Imaging of the sky can potentially address the limitation by directly monitoring the sky luminance distribution in real-time based on high resolution mapping. The next section reviews existing technologies on spatial luminance monitoring devices and their potential issues for sky luminance monitoring. Section 2.3 introduces the bi-directional transmittance distribution function (BTDF) that is commonly applied in lighting computation for complex fenestration systems (CFS), which has a different range of data volume according to the resolution required in different applications. It also presents the existing compression methods to reduce BTDF data volume for storage and transmission on a compact platform. Section 2.4 reviews the evolution of conventional shading automation systems and analyses their advantages and disadvantages in improving occupants' visual satisfaction. The existing control methods of EC windows are presented in Section 2.5. The research questions of the thesis are raised in Section 2.6.

Chapter 3 elaborates the design and demonstration of an embedded photometric device (EPD) that integrates sky luminance monitoring and on-board lighting computing, improving limitations of conventional devices for the luminance monitoring of the sky. A deliberate calibration procedure is presented to optically correct the spectral response and vignetting effect of its imaging system in Section 3.3. The EPD spans a wide range of luminance detection (150 dB), including the luminance of the sun, the sky background, clouds, and landscape

Chapter 1. Introduction

at daytime. Section 3.4 demonstrates its performance of lighting simulation with 'in-situ' experiments in image rendering and horizontal (work-plane) illuminance calculation based on the monitored luminance distribution of the sky (and ground), compared with a common practice employing the Perez all-weather model and weather data.

Chapter 4 investigates a scheme based on planar wavelet transform to compress BTDF data of complex fenestration systems (CFS), in order to reduce the volume of BTDF data on the EPD. The compression routine is explained in Section 4.2, with a brief introduction of wavelet transforms. The next section shows the performance in compressing a medium-resolution BTDF of five different CFS with regard to intrinsic (generic) error and the contributed error in daylighting simulation. Section 4.4 evaluates the influence of compressing a high-resolution BTDF of Venetian blinds at various compression ratios on work-plane illuminance simulation based on the monitored luminance distribution of skies by the EPD.

Chapter 5, as a key chapter, presents a highly integrated automated Venetian blind that employs the EPD as both a sensor and a controller, overcoming limitations of conventional automated shading systems. It is designed and demonstrated to regulate daylight flux in buildings as a decentralized system according to the varying sky conditions. The automated blind aims at providing sufficient daylight illumination on a work-plane, mitigating excessive solar heat gain, tempering discomfort glare, and offering maximum views of the outside to occupants, based on real-time daylighting simulation performed by the EPD integrated in the shading frame (or shell). The schematic of the automated shading system is illustrated in Section 5.2. Section 5.3 explains the methods employed in lighting computing and control algorithms to determine an optimal shading position. Section 5.4 illustrates the empirical validation of the automated EVB in tuning daylight dynamically in a daylighting test module on the EPFL campus in Lausanne, under various sky conditions during summer, autumn, and winter. A subjective study is presented in Section 5.5 to survey users' visual satisfaction with daylighting regulated by the system. Section 5.6 analyses the simulation uncertainty influenced by different reflectance values of a modelled interior, regarding applicability and commissioning complexity.

Chapter 6 illustrates the same EPD controller integrated with a split-pane EC window, as a stand-alone glazing tint control system to offer an optimal daylight environment in the building interior. Section 6.2 illustrates the design and schematic of the automated EC glazing system. The next section explains the methodology and algorithm in real-time lighting computing and the optimization process of EC tint state combinations. Section 6.4 demonstrates the performance of the automated EC window in a full-scale testbed at Lawrence Berkeley National Laboratory, CA, in securing sufficient daylight provision, mitigating excessive solar heat gain, and tempering discomfort glare for occupants, under various sky conditions. The performance is also contrasted with an existing control practice using the Perez all-weather model and

weather data. This chapter is completed with a discussion of the limitations of the EPD and EC glazing response speed under a partly cloudy sky with rapid motion of clouds, of which the potential improvement or solution is also introduced.

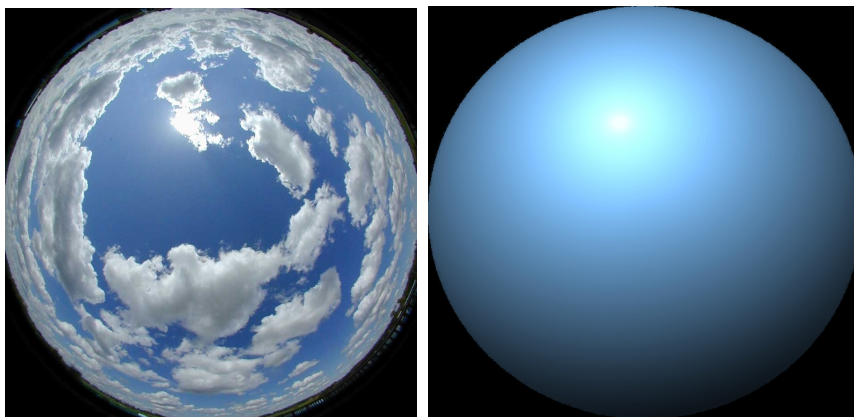
2 State-of-the-art

2.1 Limitation of sky models

Daylighting simulation is a common way to pre-design and analyse the daylight utilization in buildings, by using advanced techniques of image rendering and daylighting metrics calculation. Although annual simulation of day-lit intra-scene applications in buildings has shown convincing results [82], if the time scale shrinks to minutes or even seconds, especially when daylighting simulation is applied in real-time shading or lighting control, the discrepancy between simulation and reality is significant for transient computation [83], since the simulation is contingent upon simplified sky luminance models. Sky models were formulated for the initial purpose of comparing different sky luminance distributions, including clear, overcast and partly cloudy skies. They are commonly based on the averages of a range of sky types and cannot precisely describe a sky luminance distribution for a specific location and moment in time [84]. Moreover, the sky spans a wide range of luminance magnitude and varies dynamically. The direct sun luminance is generally in the range between 10^7 cd/m² and 1.6×10^9 cd/m². The average luminance of the sky background can vary from 2×10^3 cd/m² under a overcast sky to 8×10^3 cd/m² under a clear sky, while white clouds can achieve a luminance value upto 3×10^4 cd/m².

The International Commission on Illumination (CIE) has defined 15 different standard sky types [85] including the CIE clear and CIE overcast skies. The luminance distribution of the CIE clear and overcast skies can be regarded as two extremes of naturally occurring skies, and most real skies are intermediate ones between them. To make the modelled sky change dynamically according to the weather, Perez proposed the all-weather sky model [86] based on the solar zenith angle, sky clearness, and the sky brightness, which can be derived from the direct normal and diffuse horizontal irradiance. Despite its dynamic feature according to the sky variation, the Perez all-weather model is derived from the sky luminance monitored in Berkeley, CA, USA, which does not necessarily represent all the sky conditions for any part of the world [87]. Although the CIE General Standard sky 2003 [88] adopted sky models based on

scanned sky luminance at extended locations of Berkeley, Tokyo, and Sydney, the sky model based on empirical formulae and fitted parameters shares the same issue, which cannot resolve local micro-climate. Furthermore, reconstructing the real sky luminance distribution would require a sampling frequency at least twice as high as the maximum spatial frequency of the sky luminance distribution, according to the Shannon sampling theorem [89]. In contradiction to this, the Perez all-weather model based on merely two input variables of direct normal and diffuse horizontal irradiance and massive interpolation can hardly reconstruct the real sky luminance distribution with precision at the time scale of minutes or seconds, since cloud edges and high contrast sky patches require a much higher sampling frequency or resolution. An example of partly cloudy skies is illustrated in Figure 2.1. In addition, the common practice of modelling the ground with a constant reflectance plane contributes to noticeable disparity with reality since the material of the ground can be diverse: while the snow reflectance can reach 75%, that of the asphalt is around 7%. Moreover, the solar luminance sensed from the ground alters according to the position of the sun and weather conditions including mist, smog and haze. To address these limitations, preliminary investigations based on high dynamic range (HDR) imaging techniques for sky luminance monitoring have been conducted by Inanici [90], pointing out its improved accuracy in sky luminosity reproduction. This technique will be further investigated in Chapter 3 for real-time lighting simulation and will be used in Chapter 5 and Chapter 6 for shading and EC glazing control.



(a) HDR image of a real sky

(b) CIE intermediate sky model

Fig. 2.1. Partly cloudy skies

2.2 Image sensors used in luminance monitoring

Recent progress in microelectronics has enabled Complementary Metal Oxide Semiconductor (CMOS) image sensors gradually substitute of Charge-Coupled Device (CCD) image sensors [91], thanks to their better signal-noise ratio (SNR), dynamic range (DR) and data output speed. Among others, CMOS image sensors exhibit advantages in the compatibility with computing circuits, versatility of imaging patterns and low power consumption. Simultaneously, the

2.2. Image sensors used in luminance monitoring

development of micro-processor technology has set a trend toward smaller size, lower power consumption and higher processing speed [92]. The performance of current micro-processing unit (MPU) has made it possible to couple an MPU and high-resolution image sensors into an embedded platform for data acquisition and real-time processing.

Studies have highlighted the possibility of using image sensors as a reliable luminance monitoring apparatus. Stumpfl et al. [93] suggested an approach for photo-realistic rendering using a digital single-lens reflex (DSLR) camera by 7 consecutive frames based on HDR imaging techniques to build-up a 132 dB dynamic range picture to capture the sky luminance distribution. Wüller et al. [94] converted the RGB grey-scale values of images by a DSLR camera into the xyY color space by linear matrix transformation, for photometric purposes, to acquire a luminance value from each pixel. The limitation of the DSLR camera based approach are manifold: i) pixels monitoring the direct sun disk are commonly overexposed, its luminance being not directly measurable, ii) capture of multiple frames employs multiple lens apertures [93], which adds to difficulty to the calibration process, since each aperture requires a separate calibration process in the vignetting effect, iii) the image acquisition process is time consuming due to aperture change or extended exposure time to achieve a wide dynamic range, and consequently clouds could be blurred on the image due to their rapid motion, and last but not least, iv) the RGB channel response of an image sensor is device dependent and, without an 'ad hoc' calibration, a simple linear color space conversion for luminance monitoring is commonly associated with noticeable errors [95]. Borisuit et al. [96] used a HDR (132 dB) achromatic B&W (black and white) camera for luminance mapping of indoor spaces to investigate photometric metrics [97]. Two color filters were applied to rectify the spectral response of the camera in order to get close to the photometric sensitivity of humans. Nonetheless, the luminance detection range of this device is not large enough for monitoring the luminance distribution of the sky especially to cope with the luminosity of the sun, and the HDR image sensors commonly sacrifice the resolution for larger pixel sizes on a silicon wafer, of which the cost and availability is not a neglectable issue.

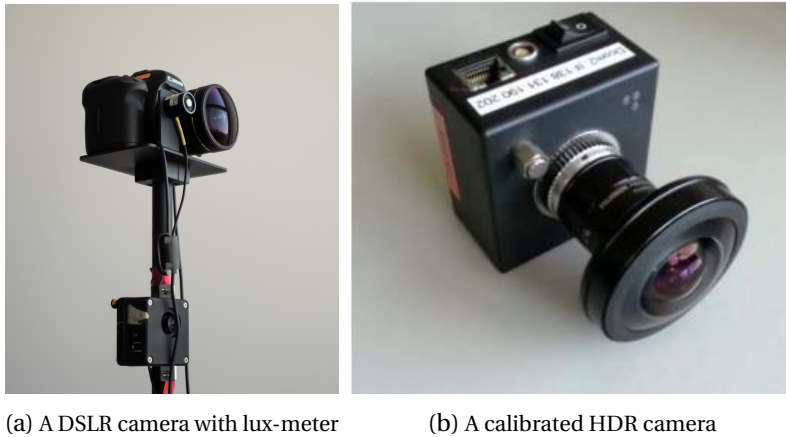


Fig. 2.2. Camera used as apparatus to monitor spatial luminance distribution

2.3 BTDF data compression

Complex fenestration systems (CFS) have gradually gained popularity as standard components in high performance buildings to efficiently control daylighting [98], including shading systems, light diffusing glass, and sun re-directing devices, which commonly exhibit merits for improving daylighting in deep regions of rooms (distant from windows) and preventing glare from direct solar rays [99]. Despite their advantages in transforming daylight, the implementation of CFS can have negative impacts on occupants' visual comfort, including reducing daylight transmission and occluding outwards view [100]. Therefore, proper pre-planning is essential before applying CFS in buildings. However, making precise prediction of the performance of CFS in daylighting is still a challenge to simulation tools in order to encourage acceptance by users and practitioners [101].

In recent decades, considerable work has been done on quantifying the optical behavior of CFS, including development of both lighting metrics and models [102]. The bi-directional transmittance distribution function (BTDF) is one such model that comprehensively describes the directional light flux transmittance property of a certain type of transparent material or complex fenestration system (CFS) [103]: it serves to characterize behaviour of photons when interacting with CFSs. The BTDF not only makes it possible for objective comparison of different CFS but also contributes to its efficient integration into daylighting simulation software, without pre-knowledge of the detailed geometry or material properties of the CFS. Goniophotometers [104] and computational tools [105] have been developed to monitor and simulate the BTDF of a CFS respectively.

BTDF is defined by the ratio of emergent radiance L ($\text{W} \cdot \text{sr}^{-1} \cdot \text{m}^{-2}$) to incident irradiance E (W/m^2) on the incident plane, as described in Equation (2.1) [106], where the subscript i denotes incident direction, t refers to transmitted direction, and θ and ϕ are the zenith

and azimuth angles in spherical coordinates, respectively. The function is generally specified with wavelength λ when a spectral dependent property is considered and is assumed to have spatial uniformity on the incident plane. In the context of photometric quantities, BTDF can be integrated with the photopic luminosity function $V(\lambda)$ [107] over wavelength λ to eliminate the dimension.

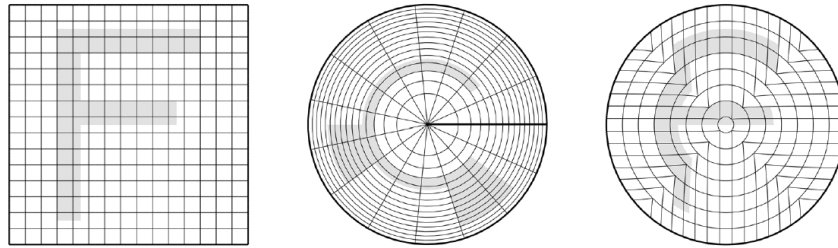
$$f_t(\theta_i, \phi_i; \theta_t, \phi_t; \lambda) = \frac{L_t(\theta_i, \phi_i; \theta_t, \phi_t; \lambda)}{E_i(\theta_i, \phi_i; \lambda)} \quad (2.1)$$

Because BTDF commonly comes in the form of a 4-dimensional tensor, the volume of an uniform or non-uniform resolution BTDF can reach megabytes, hundreds of megabytes, or even gigabytes on computational devices, depending on the number (resolution) of discretized incident and emergent directions. The resolution of BTDF must satisfy specific requirements in different applications. For daylight provision simulation, including horizontal or vertical illuminance distribution, the Klems angular basis [108] with 145 incident directions and 145 emergent directions is commonly employed, resulting in a BTDF volume at the level of megabytes. The recent development of visual comfort research has focused on the evaluation of glare risk, which is increasingly important in daylighting simulations [109, 60, 110]. Multiple indices for quantifying the glare risk of occupants have been proposed including the Daylight Glare Probability (DGP) [53], Daylight Glare Index (DGI) [54], and Unified Glare Rating (UGR) [55], the calculation of which can be essentially based on HDR view images. Simulation of HDR image rendering is sensitive to the resolution of directional transmittance property of employed CFS, where thousands of incident and emergent directions of BTDF can be involved, making the volume of BTDF reach hundreds of megabytes. Furthermore, it is challenging to assess the glare sensation that results from the exposure to the sun orb [111]. Since the sun only subtends 0.53° as its apex angle, the volume of BTDF with sufficient resolution can exceed gigabyte levels.

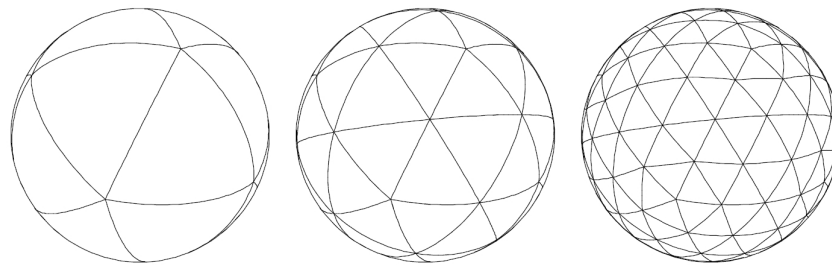
In addition, the dimension of BTDF data can be further extended when a BTDF set need to be monitored or computed to characterize the luminous transmittance property of a CFS at its various states. For example, multiple BTDFs are needed to comprehensively describe the light transmitting behavior of an operable Venetian blind with different tilt angles of the blades or for an electrochromic glazing at different tinted shades, which can increase the volume of a BTDF by an order of magnitude. Furthermore, recent studies that evaluated non-image-forming effects of light in visual comfort have attracted the attention of researchers on spectral properties of daylighting [112]. When wavelength as an extra dimension is involved in BTDF, its volume can be further multiplied by a factor of ten or even one-hundred depending on the spectral resolution. The increasingly high volume of a fine resolution BTDF for use in comprehensive studies of visual comfort would add considerable burden to storage and transmission of BTDF data base for characterizing the light transmittance properties of a

collection of CFSs.

Compression is an effective way of reducing redundancy in the BTDF data, which increases the efficiency of data storage and transmission between platforms. Ward et al. [113] employed the Shirley-Chiu disk-square mapping approach to transform spherical coordinates of incident and emergent directions into a square [114], as shown in Figure 2.3 a), thereby transforming BTDF data into a 4 dimensional tensor. Depending on the local smoothness, compression is realized by merging (averaging) neighbouring voxels into a single voxel at coarse resolution when their variance does not exceed a pre-defined threshold. Although compressed BTDF data can be used in Monte Carlo sampling, it is difficult to achieve a high compression ratio (CR) with a tolerable error, which introduces a step-pattern effect on the compressed BTDF data. This approach also limits angular basis of the original BTDF data to those with homogeneous discretization in the zenith and azimuth directions. Schröder and Sweldens [115] proposed a spherical wavelet method based on the lifting scheme [116]. This compression approach achieved a high compression ratio for data points distributed homogeneously on the surface of a sphere. Although it is applicable for compressing BTDF data, the spherical wavelet compression firstly need to map the original data onto semi-homogeneously distributed vertices on a subdivided icosahedron via interpolation, as shown in Figure 2.3 b). Reconstruction involves a secondary interpolation to convert it back to the original basis. The interpolation process contributes to pronounced errors, if the original BTDF basis is distinct from the semi-homogeneous distribution. Lalonde and Fournier [117] provided several important insights into multi-dimension wavelet decomposition of bi-directional reflection distribution function (BRDF). A compression scheme based on planar wavelet transform will be introduced and investigated in Chapter 4.



(a) Shirley-Chiu disk-square mapping [114]



(b) Subdivision on an icosahedron [115]

Fig. 2.3. Transforms involved in BTDF compression

2.4 Shading automation

Since daylight varies dynamically, according to different sun positions and varying sky conditions, inadequately harnessed daylight can not only overheat buildings via excessive solar heat gain (SHG), but also induce discomfort glare for occupants [118]. Venetian blinds are popular for application in buildings, since they can not only regulate daylight injection into buildings, but also preserve outwards view and privacy for users due to their two degrees of freedom (vertical position and tilt angle of slats) in adjustment. However, their actual performance is largely limited by users' manual control and behaviour [79], of which the low frequency of interaction with shading has been reported by survey studies [81, 71]. Since daylight can change rapidly in both its intensity and direction during one day, it is impractical for occupants to constantly manipulate shading devices according to the varying sky conditions, while simultaneously performing their own tasks.

Well-designed automated daylighting control systems have the potential to substantially reduce peak cooling requirements [119] and to improve occupants' visual comfort at the same time. Automated blinds have been designed and developed over the past decades to overcome the limitation of manual ones. Their design has been evolving along with the technological development in sensors and computational tools. Early studies on shading control before the 80s were based on the intensity of solar radiation reaching on windows to adjust shading positions according to set-points [120]. In the 90s, daylighting control strategies on the

work-plane started to draw researchers' attention. A closed-loop control system was introduced to automate Venetian blinds to stabilize the work-plane illuminance (WPI), employing a ceiling mounted photo-sensor pointing at the task area [121], as shown in Figure 2.4. Peak cooling load reduction of 28% was reported by Lee et al. [2] for the automated Venetian blinds compared with the case involving static horizontal slats during summer in Oakland, CA. However, several issues associated with the control system were revealed [122, 2], regarding calibration (correlation) between the photo-sensor signal and WPI for both day and night time, regarding noticeable variation of this correlation subject to slat angle, sun position and sky conditions, and regarding complication of furniture rearrangement. These issues add to the complexity of the commissioning phase, and the commissioning quality has a noticeable impact on the actual shading control performance. Later, sophisticated control algorithms including fuzzy-logic rules [123], artificial neural networks [124] and multi-zone control [125] were investigated taking multi-variables as control input variables, including weather data, room temperature, solar radiation, and user presence. Above all, the preliminary automated blinds based on photo-sensors only managed to evaluate WPI, without preventing discomfort glare for occupants, since directional information of incident daylight is lost on a photo-diode.

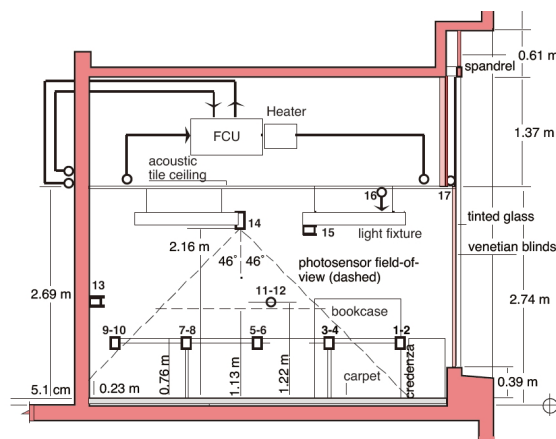
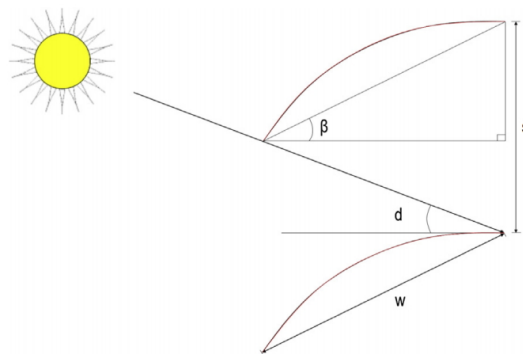


Fig. 2.4. A ceiling mounted photo-sensor for shading control [2]

With advances in image-sensor technology, calibrated DSLR cameras have been gradually applied as apparatuses to monitor the directional luminance distribution in interior space based on HDR imaging techniques [94], as a relatively economic solution. Newsham et al. [126] successfully applied a camera to control roller blinds in an office room compared with photo-sensors. The study showed performance improvement in WPI control accuracy and the possibility of assessing discomfort glare using a camera. Motamed et al. [127] implemented a second camera with a HDR image sensor at an occupant's sitting position, assessing glare risk, to control the position of roller blinds by using fuzzy logics. Although the 'cut-off' angle strategy is a common way to determine the slat angle of Venetian blinds required to exclude direct sun rays based on the sun profile angle [128] for occupants, Karlsen et al. [129] pointed out that it was insufficient to avoid discomfort glare from specular inter-reflection between

slats, as illustrated in Figure 2.5 a). Goovaerts et al. [130] further investigated the application of a DSLR camera in controlling Venetian blinds in different scenarios, as shown in Figure 2.5 b). With captured HDR images, the DGP was calculated to assess glare risk for occupants: a closed-loop control configuration was employed to iteratively adjust the blind position until DGP was below the discomfort threshold, in order to moderate the inter-reflection glare between slats. Since frequent movement of shading can contribute to users' dissatisfaction, a suppression algorithm was applied to maintain shading position for 10 min after each movement, which inevitably reduced response speed and accuracy of daylight control.



(a) Cut-off strategy to block the sun [129]



(b) A DSLR camera in shading control [130]

Fig. 2.5. Two approaches in control of tilt angles of Venetian blinds

Although cameras have been extensively used for shading control in a laboratory environment, privacy issues induced by positioning cameras indoors remain an impeding factor for their practical application [126]. From a performance perspective, the existing interior camera based shading control systems also share the following limitations:

- A closed-loop control system is commonly applied to stabilize WPI and glare risk, which induces shading oscillation or frequent movements that cause disturbance for occupants [2].
- Although a suppression algorithm can be applied to reduce the closed-loop oscillating motion of shading, it inevitably sacrifices daylight control accuracy by reducing iterative movements, since the oscillation of a closed-loop system actually promotes the convergence of controlled WPI or glare metrics to a set point.
- The 'cut-off' angle strategy, used to exclude direct sun light, cannot prevent discomfort glare from the inter-reflection between slats of Venetian blinds [129].

- Prevention of veiling glare due to the secondary reflection on specular surfaces from the exterior environment, including glazing walls of neighbouring buildings and wind screens of static vehicles, remains a challenge.
- When a glare source disappears outside, the controller commonly fails to reopen shading timely.
- The field of view (FOV) of indoor cameras can be occluded by occupants' random movements.
- The availability of weather data, including direct normal and global horizontal irradiance, limits the application in decentralized building units [131], since office owners commonly have limited access to a roof or a weather station nearby.
- Last but not least, the pre-knowledge of geographical location, window orientation, sensor position, and possible furniture rearrangement adds cost and difficulty in the commissioning phase, as impeding factors of their wide application [132].

A novel self-sufficient shading system will be introduced in Chapter 5 aiming at improving or addressing the above issues of conventional automated shading systems.

2.5 Electrochromic glazing control

EC windows have been alternative products for highly glazed offices and high-rise buildings to regulate daylight, in order to achieve energy saving and visual comfort improvement. The integration of EC glass with a control system is a major challenge for the broad application of EC glass. Since the sky is dynamic, daylight conditions can change drastically during daytime according to variations in the sun position, atmosphere turbidity, and patterns and motion of clouds. If not harnessed properly, excessive daylight ingress can overheat building interior and simultaneously induces discomfort glare for occupants [118]. Tint states of EC glazing therefore must vary in real-time according to the changing sky conditions to provide an optimal daylighting environment in building interior, which is impractical to be realized by manual manipulation [80, 81]. Well-designed daylight control systems can substantially reduce peak cooling loads, provide sufficient daylight, and improve occupants' visual comfort [133]. Early studies of EC glazing control systems focused on maintaining the daylight provision with a single tint state of the whole window. Sullivan et al. [134] simulated three strategies of EC glazing control to compare their energy performance, including maintaining work-plane illuminance (WPI) based on a closed-loop control, linear tuning based on incident solar radiation and set-points, and control according to cooling load. From energy saving perspective, Karlsson et al. [135] studied control of EC transmittance according to solar radiation impinging on the window surface in three different locations. Lee et al. [136] employed a ceiling-mounted photo-sensor to monitor WPI, based on which a closed-loop control system was set-up to maintain WPI between 540 and 700 lux. Daily lighting electricity demand was reduced by

8-23% as compared to a reference tinted glazing showing a luminous transmittance of 0.5.

Recent studies of EC glazing control have started taking discomfort glare into consideration as a human centric control in order to improve visual comfort for occupants. Jonsson et al. [137] constrained the transmitted direct solar vertical irradiance below 200 W/m^2 to moderate discomfort glare in a simulation study. Gugliermetti et al. [138] used DGI to determine a solar irradiance set-point to mitigate discomfort glare. Piccolo et al. [139] employed two metrics, DGI_N [140] and Glare Subjective Rating (SR) [141], to assess glare achieved by an EC glazing controlled by a closed-loop system to maintain WPI at approximately 300 lux. Although these approaches can improve visual comfort in given situations, they are not designed to precisely handle discomfort glare for users at a specific location (user-centric control); imprecise daylight control can either turn the environment dark [76], increasing usage of artificial lighting [142], or moderate glare insufficiently. Preventing discomfort glare remains a difficult task when the sun is in the field of view (FOV) of occupants. Fernandes et al. [143] introduced split-pane EC glazing control in which transmittance of two window panes was managed independently. In order to moderate discomfort glare, two metrics (vertical illuminance at eye level of occupants and luminance ratio between a visual task area and surround environment) were controlled using a lighting calculation based on weather data and sky luminance models. In another study, Fernandes et al. [144] performed EC glazing control with different modes according to the set points of outdoor vertical illuminance and sun position that is calculated based on astronomical formulas. When the sun is within a pre-set position range (can be seen through window by occupants at a defined position), one or more subpanes would be tinted to the darkest state to temper discomfort glare, despite the resulting dark daylit environment as reported by occupants. The setpoints were changed seasonally to achieve better performance of glare mitigation in contrast to the adoption of constant setpoints. Although discomfort glare from direct sun exposure can be improved by the adjustment of set-points based on practitioners' experience, the issue of veiling glare remains a challenge due to secondary reflections on specular surfaces from surroundings, including glazed façades of opposite buildings and wind screens of parked vehicles. With technological advances, calibrated cameras have been used indoors to monitor discomfort glare of occupants and control shading accordingly [130]. However, privacy issues introduced by placing cameras within buildings to monitor building interior remains an impeding factor for a real application in EC window control [126]. Furthermore, since tinted EC glass renders a bluish environment and it is believed that users have a preference on the neutral spectrum of daylighting, Mardaljevic et al. [74] studied an approach for maintaining the neutral spectrum of illumination with an EC window by combining tinted glass panels with a small fraction of clear glass panels. A stand-alone EC window control system will be introduced in Chapter 6 to provide sufficient daylight provision, mitigate excessive SHG in buildings, and moderate discomfort glare for occupants.

2.6 Research questions

Based on the above summarized limitations of conventional daylighting control systems, the research questions that this thesis addresses are as follows:

- How can the visual satisfaction of occupants be efficiently achieved by a daylighting control system according to dynamic sky conditions with minimal disturbance?
- Is it possible to effectively assess discomfort glare both from the sun and from secondary reflections in surroundings for users without inducing privacy issues in buildings?
- Can a daylighting control system have the minimal installation and commissioning difficulty with enhanced user acceptance?
- Is it possible for a daylighting controller to be compatible for shading devices and switchable glazing?

3 Embedded photometric device

3.1 Introduction

Studies have shown that the exposure to daylight can have substantial visual/non-visual benefits for building occupants. To optimise daylighting provision while maintaining a comfortable visual environment, daylighting control systems have been investigated by architectural engineering and academic research for a number of years. However, real-time handling of daylight flux in buildings requires transient daylighting simulation with high accuracy and, daylighting simulation, as performed to date, is significantly impacted by the employed sky luminance distribution models which only crudely reproduce the real sky characteristics due to oversimplification and limited luminance sampling inputs.

To provide a sky luminance distribution with high accuracy for daylighting simulation, an embedded photometric device (EPD) is proposed in this chapter to combine high dynamic range (HDR) imaging based high-resolution sky luminance monitoring with quasi real-time on-board daylighting computing. The EPD is composed of a low-cost image sensor and a field programmable gate array (FPGA) micro-processor. A calibration procedure of the whole imaging system, regarding its spectral response (spectral correction error $f'1 = 8.89\%$), vignetting effect and signal response, was formulated and validated experimentally. The device was made to measure a wide luminance range (150 dB) including that of the direct sun disk, sky vault, and landscape simultaneously. Finally, experiments during predominant clear and overcast sky conditions were conducted respectively to assess its performance in daylighting simulation, both qualitatively and quantitatively. The experimental results demonstrated its quality in solar tracking as well as its capability to reduce daylighting simulation error to $\frac{1}{7} \sim \frac{1}{3}$ of that of a common practice using the conventional Perez all-weather sky model for workplane illuminance calculation in office buildings. The chapter is based on the article published in the "Building and Environment" journal by Wu et al. [145].

3.2 Device Architecture

A highly self-sufficient system is normally comprised of microprocessor units (MPUs), memory, sensors and actuators. In the case of lighting simulation, the computation load for an MPU is formidably heavy in the massive calculation of ray-tracing algorithms [146]. A field programmable gate array (FPGA) processor with system on-chip (SoC) architecture was selected as the major MPU of the platform, due to its high-speed performance in both calculation and input/output (IO) and to its flexibility in communication with sensors or actuators. In the context of sky luminance monitoring under an extreme solar radiation, a low-cost image sensor with high-speed shutter was selected for sensing the whole sky, including the direct sun disk, the sky vault, and clouds. The specification and detailed architecture of the components constituting this device are given here after.

3.2.1 Image sensor

The image sensor is fundamentally an accurate device for the measurement of light intensity as an array of photo-diodes. An 1/2.5 inch low-cost CMOS image sensor was employed as the main sensing unit. The sensor features 5 million pixels (frame size: 2593×1944), a 12-bits ADC (analog to digital converter) resolution and 38.1 dB SNR (signal to noise ratio). Its short integration period enables it to detect extreme luminance values without any saturation for outdoor applications. In addition, the maximum data transmission rate of the sensor reached 9.6×10^7 pixels/second to output a full frame in 70 ms. Its 381 mW peak power at maximum resolution satisfies the constrain of low-power consumption applying to the component of an embedded device. Furthermore, the wide range of operation temperature (-30°C to $+70^{\circ}\text{C}$) allows its application in most geographical locations on the planet. Regarding the shutter mode, the electronic rolling shutter (ERS) was chosen, ensuring an identical exposure time for each pixel at various positions on the image plane [147]. The pixel array was arranged in the RGB Bayer pattern, as illustrated in Figure 3.1, which is a common way of arranging RGB pixels. The ratio of the RGB pixel number was 1:2:1 respectively. For the measurement of photometric variables, since the color information was disregarded, 4 pixels were grouped as a sensing unit to detect and synthesize the luminance by each unit. The sensor was also equipped with multiple registers for the configuration of its functionalities, including operation mode, driving frequency, readout pattern, etc..

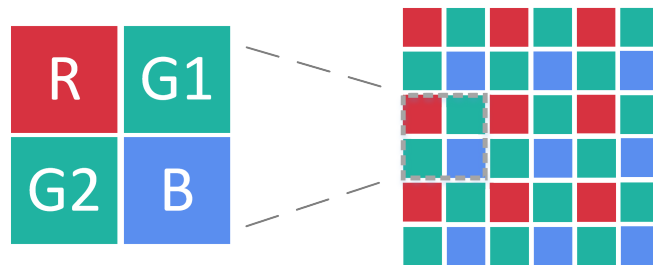


Fig. 3.1. RGB Bayer pattern of the pixel arrangement of the image sensor

3.2.2 FPGA processor

FPGA chips have been widely applied by the telecommunication industry, which imposes strict requirements on the data processing and transmission speed [148]. In the context of this study, its high speed performance matches the demand of bulky data transfer from the image sensor, particularly in case of high dynamic range imaging (HDR), leading to a massive data volume. The recent development of FPGA-SoC architecture, embedding a hard-core-processor (HPS) with FPGA on a single silicon die, has provided further versatility to such processors in operation with high-level algorithms [149]. To balance both performance and compactness, a commercial FGPA chip (Altera Cyclone V) was employed as the main MPU to import bulky pixel data, to control sensor-actuators, and to operate on-board lighting simulation algorithms. This single processor is composed of two major parts: FPGA fabric and HPS. The FPGA fabric part is essentially a massive field of logic blocks (85K logic cells) and a hierarchy of reconfigurable interconnects; each of them can be configured to realize complex logic functions via place-and-route by a hardware description language (HDL). On the field of logic elements, a number of hardware units, including sensor interfaces, memory managing units and calculation accelerators, can be implemented as long as the communication protocol and timing rules are strictly complied with. As shown in Figure 3.2, a sensor interface was established together with a direct memory access (DMA) unit in the FPGA fabric. The interface was designed with two sub-functionalities: i) control of image sensor, and ii) transfer and pre-processing of pixel data. The image sensor, connected with the processor through bidirectional pins, can be configured by parameters written into an array of registers to set up the frame size, operating mode and shutter type. In addition, the interface also triggers the shutter of the image sensor and regulates the exposure sequences used by the HDR imaging technique during the sky luminance monitoring stage. Then after a frame has been collected on the image sensor, the interface is prepared to read in the pixel data sequentially, to pre-process the data and to arrange it in the external memory through the internal FPGA2SDRAM bridge for further calculation. The HPS part of the processor is an ARM Cortex-A9 (925 MHz) unit with peripherals including SDRAM controllers to access external double data rate three (DDR3) memory and communication bridges with the FPGA fabric part (e.g. HPS2FPGA bridge) to access interfaces and general purpose input/output (GPIO), as shown in Figure 3.2. A simplified version of Linux has been installed on the ARM unit as operation system configured for embedded devices, where executive programs (including C and C++) can run with relatively high-level algorithms, including luminance mapping and ray-tracing. In this way, the two parts cooperate seamlessly in executing both the low-level algorithms, including data collection, preprocessing and parallel acceleration, and the high-level algorithms, including ray-tracing and Monte-Carlo integration.

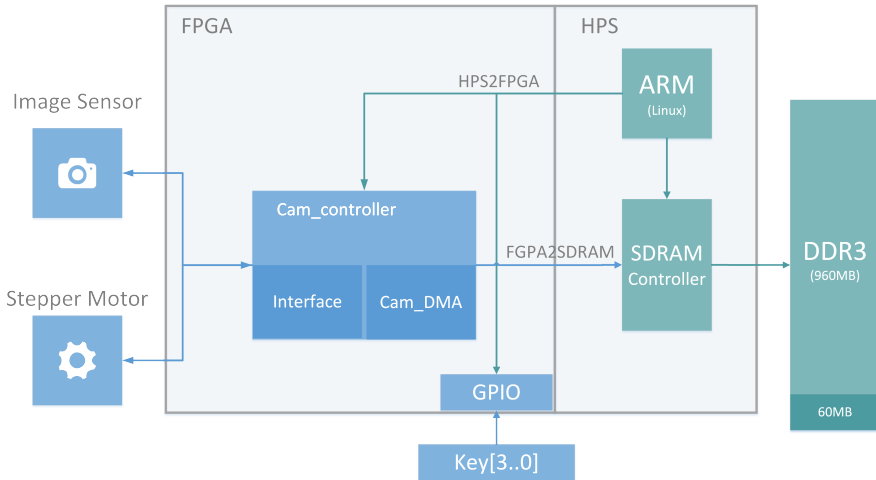


Fig. 3.2. Modules configured in the FPGA chip and connections with external elements

3.2.3 Lens and actuator

To cover both the sky vault and the ground, a wide angle lens with 2.5 mm focal length was coupled with the image sensor as the imaging part of the device. As a super-wide angle lens contributes to noticeable optical distortions in imaging and sacrifices a portion of unused pixels, the field of view (FOV) of the lens was limited to an opening angle of 160° ($129.8^\circ \times 96.7^\circ$ in the horizontal and vertical directions respectively), maintaining the distortion at a tolerable level: an image illustrating its FOV is shown in Figure 3.3 with the sun disk in FOV. The maximum angular resolution of a pixel is 0.041° (equivalently 5.24×10^{-7} sr in solid angle), which is one magnitude finer than that of a class B luminance meter (0.33°). The high resolution feature of each pixel makes it possible for the device to detect or even indirectly (due to specular reflection) identify glare sources with particularly minuscule size in lighting simulation.



Fig. 3.3. Field of view (FOV) of the imaging system

Furthermore, since the device has to be exposed under the sky vault for monitoring, the influence of the direct sun light issued from the solar disk was taken into consideration in the design phase. To mitigate the risk of irreversible physical damage, an opaque shield mask was installed at the front end of the lens to protect the image sensor from overheating under intense solar radiation when the imaging system is idle, as illustrated in Figure 3.4. A closed-loop stepper motor was also coupled with the shield mask to open and close it when the imaging system performed measurement, keeping the maximum opening time below 0.55 s before the sensor gets overheated.

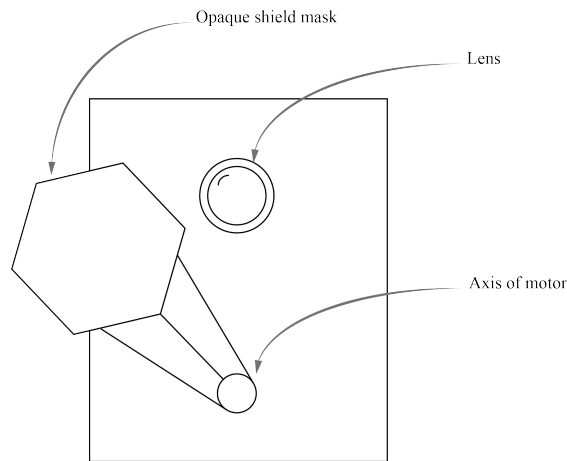


Fig. 3.4. Protection mask for the imaging system

3.3 Calibration procedure

As the accuracy of lighting computing is contingent on the quality of measurement (sky luminance monitoring), a high quality calibration procedure of the imaging system was formulated, implemented and validated with experiments, including correction of the spectral response, vignetting effect, spatial mapping and response functions.

3.3.1 Spectral response

The spectral response of the RGB channels of an image sensor can have pronounced disparity with the color matching function of RGB primaries defined by the standard CIE-1931 triplet stimuli [150]. Its spectral response is commonly device dependent and biased, depending on the manufactures who cater in varying ways to consumers' preference in compelling color. Linear transformation of the response of RGB channels (color space conversion) into the photometric quantity can contribute to substantial errors without optical correction, ignoring the spectral discrepancy, since the photopic luminosity function $V(\lambda)$ normally does not lie in the vector space spanned by $R(\lambda)$, $G(\lambda)$ and $B(\lambda)$, λ being the wavelength of incident radiation. The error tends to be unacceptable particularly when relatively narrow bandwidth light sources are involved [151] in illumination, including light-emitting diode (LED). To

Chapter 3. Embedded photometric device

address this limitation, the spectral response of the image sensor was rectified by optical filters. Before selecting the filters, the spectral response of the image sensor with the coupled lens was measured using a spectroradiometer (left, Figure 3.5) and monochromatic light beams with the experimental set-up shown in Figure 3.5, of which the diagram is shown in Figure 3.6. A monochromator (OMNI- λ 300, Zolix), shown on the right side of the figure, was employed to bandpass a narrow bandwidth (20 nm) of light spectrum by the way of a diffraction grating from a high intensity discharge lamp (HID, Xenon arc) used as light source. Since the photometric device is dealing with the visual range of the spectrum, the monochromator swept wavelengths of the passing band at 10 nm intervals from 380 nm to 780 nm to cover the entire visual range of the spectrum. An internal near infra-red (NIR) cut-off filter eliminated unnecessary NIR range of the spectrum. In addition, an integration sphere was used to homogeneously diffuse the beam coming from the exit port of the monochromator over the internal surface of the integration sphere. Although the two devices targeted at the same area, the critical role of the integration sphere was to reduce the effect of inevitable misalignment of the FOV of a central pixel on the image plane and that of the spectroradiometer, which showed a different resolution.

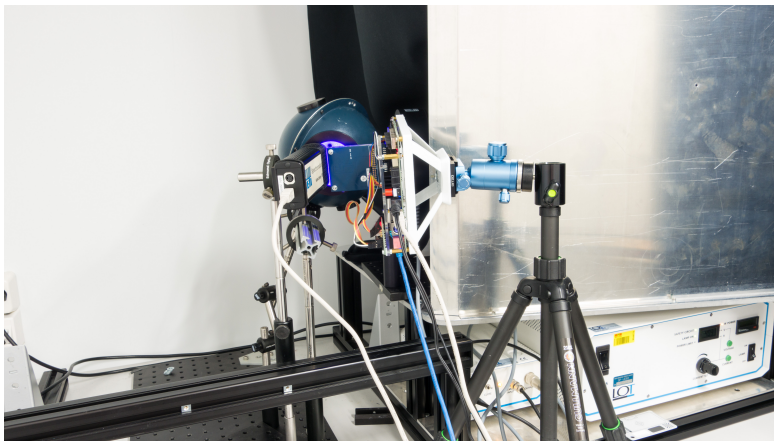


Fig. 3.5. Experimental calibration set-up

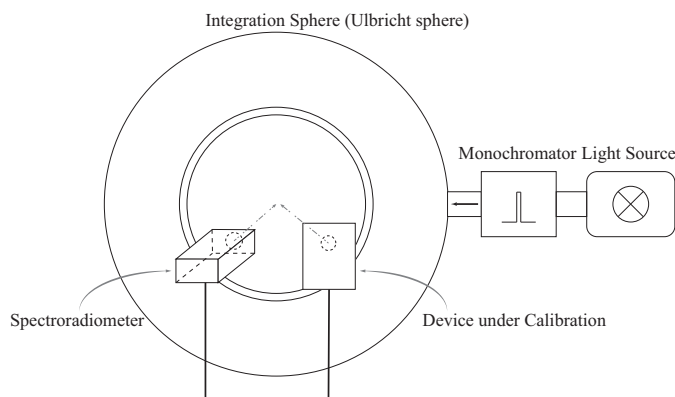


Fig. 3.6. Diagram of experimental set-up

The experiment was conducted in a darkroom in order to isolate it from parasitic light. Figure 3.5 and Figure 3.6 show the photometric device and the spectroradiometer during the calibration; both were fixed at the exit port of an Ulbricht sphere, the input port being aligned with the light beam issued from the monochromator and a light source. After scanning the entire visible spectrum, the pixel response of the image sensor was normalized by the spectral power of the monochromatic light measured by the spectroradiometer (1 nm resolution), leading to the spectral response of each channel illustrated in Figure 3.7. For each data point, 9 neighbouring pixels at the center of the image plane were averaged for each channel to reduce the spatial noise; the measurement was repeated 5 times to mitigate the temporal noise ($\pm 1.13\%$ for 95% confidence interval). Furthermore, the reset noise of pixels was measured and corrected in its response.

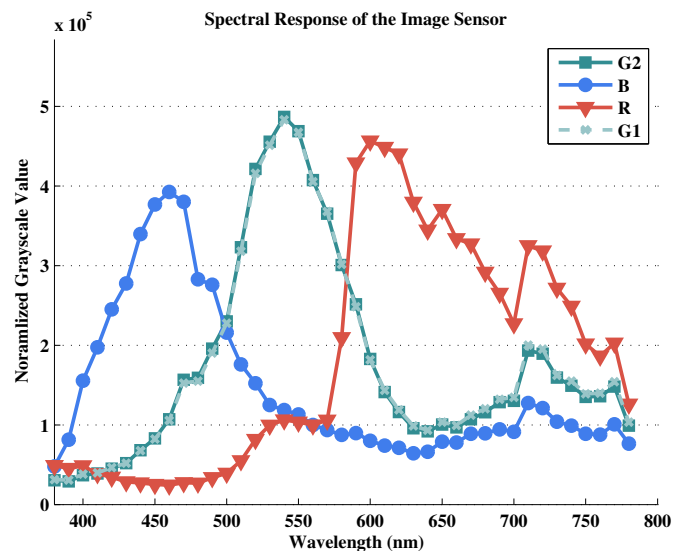


Fig. 3.7. Spectral response of the RGB channels of the image sensor

As mentioned, to improve accuracy of measuring luminance, the sensor had to be corrected by optical glass filters. The optimization was performed on a pool of bandpass filters (256 models) with neutral-density (ND) filters over 2.8 million combinations to fit the luminosity function $V(\lambda)$, through the least error in the ℓ_2 norm space. With consideration of the limited space available for filters in imaging system, the optimal set of filters was finally determined using only three filters, a cyan filter, a yellow filter and an ND filter (1% transmittance). The spectral transmittance distribution of the two color filters is presented in Figure 3.8.

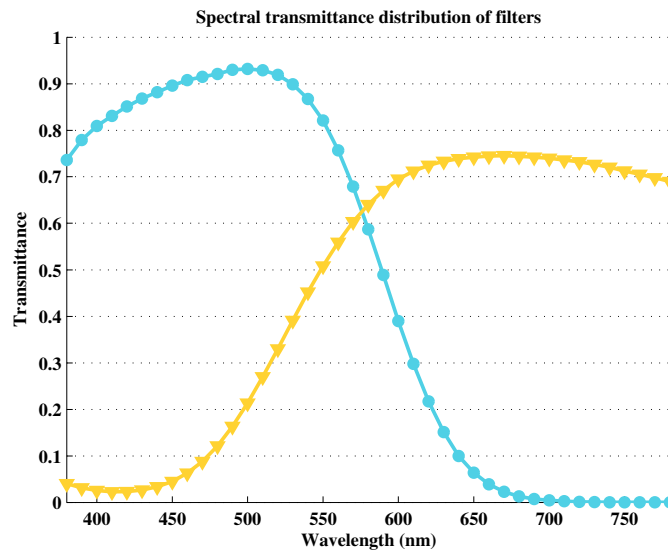


Fig. 3.8. Spectral transmittance distribution of the color filters

The filters were installed in the imaging system, between the rear side of the lens and the image sensor, instead of in front of the lens, to lessen the mechanical vignetting of the optics. Then the spectral response of the imaging system with embedded filters was measured again with the identical set-up as Figure 3.6. To assess the spectral response with high resolution, the center wavelength of the beam was swept at a finer wavelength interval by the monochromator, e.g. every 5 nm from 380 nm to 780 nm. The spatial and temporal noise were again mitigated by averaging 9 center pixels and by repetition of 5 frames per wavelength interval. Figure 3.9 illustrates the spectral response of the RGB channels of image sensor equipped with the embedded two color filters and a single ND filter for spectral rectification, which shifted the peaks of each channel close to the 550 nm wavelength as the peak location of the luminosity function $V(\lambda)$ compared with Figure 3.7.

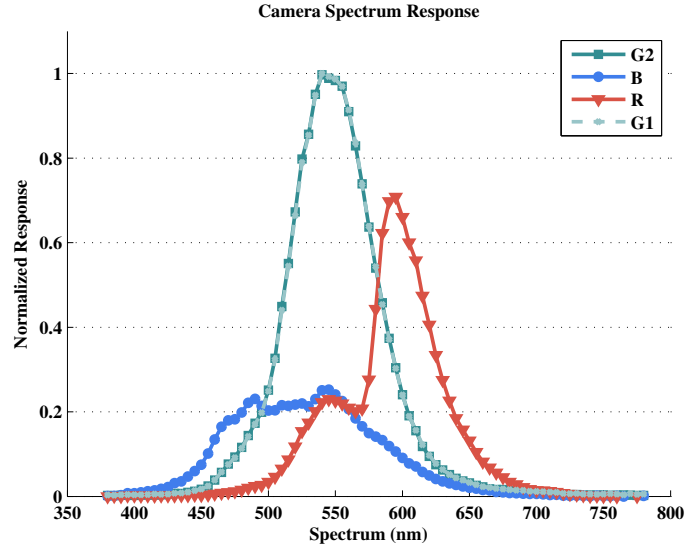


Fig. 3.9. Spectral response of the RGB channels after optical corrections

The luminosity function $V(\lambda)$ can be fitted through a linear transformation of the corrected spectral response of the imaging system equipped with filters. The coefficients of the RGB channels were determined by calculating the least-error in the ℓ_2 norm space. With optimized coefficient of RGB channels, the spectral response of the imaging system is illustrated in Figure 3.10 and is close to the $V(\lambda)$ curve. According to the CIE publication No. 69 [152], the relative spectral correction error f'_1 was determined using Equations (3.1) and (3.2), where $S_1(\lambda)$ is the spectral distribution of illuminant which is assumed to be a CIE illuminant D65, $S(\lambda)$ is the relative spectral response of the detector, and $S_n(\lambda)$ is the normalized spectral response of the detector. The f'_1 error of the calibrated imaging system equipped with optical filters is equal to 8.89%, compared to 52.9% with linear color space conversion without optical corrections. According to the DIN 5032 standard [153], the maximum f'_1 error of a commercial luminance measurement device should be 9%, which achieved in this case.

$$f'_1 = \frac{\int_{380}^{780} |S_n(\lambda) - V(\lambda)| d\lambda}{\int_{380}^{780} |V(\lambda)| d\lambda} \quad (3.1)$$

$$S_n(\lambda) = \frac{\int_{380}^{780} S_1(\lambda)V(\lambda) d\lambda}{\int_{380}^{780} S_1(\lambda)S(\lambda) d\lambda} S(\lambda) \quad (3.2)$$

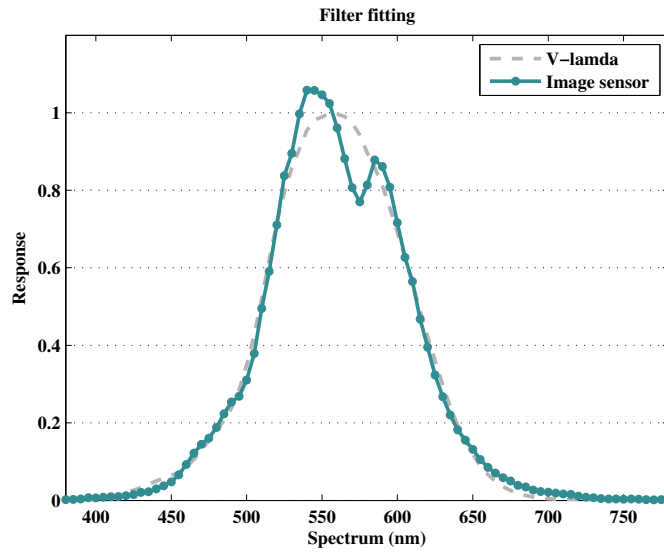


Fig. 3.10. Synthesised spectral response of the imaging system

3.3.2 Vignetting

Vignetting effect is essentially a phenomenon of imaging systems where the intensity of light is attenuated towards off-axis zones; this is particularly noticeable at the edges of a frame with wide-angle lens. Multiple impact factors involved can be categorized into natural vignetting, optical vignetting, pixel vignetting and mechanical vignetting [154]. Natural vignetting is an intrinsic property of the lens that attenuates incident rays at off-axis parts, which obeys the \cos^4 law of the off-axis angle α [154], as in Equation (3.3), where E is the illuminance at center and $E(\alpha)$ is that at off-axis pixels on the image plane. Optical vignetting is caused by the limited size of a lens and thus the clipping of light by the body of the lens, which can be potentially alleviated by introducing an aperture. Digital image sensors can also have pixel vignetting due to the occlusion by the walls of each photo-diode. In addition, the filters or the hood of a lens can contribute to mechanical vignetting.

$$E(\alpha) = E \cdot \cos^4(\alpha) \tag{3.3}$$

For a fish-eye lens, the vignetting is inevitably a pronounced problem, which need to be corrected and compensated. The glass filters, as shown in Section 3.3.1, were placed behind the lens to reduce its mechanical vignetting. The existing vignetting was then measured and corrected using the experimental set-up illustrated in Figure 3.11. The integration sphere was employed to diffuse the light beam homogeneously in all directions at its exit port, which was used as the reference target to quantify the fall-off of intensity.

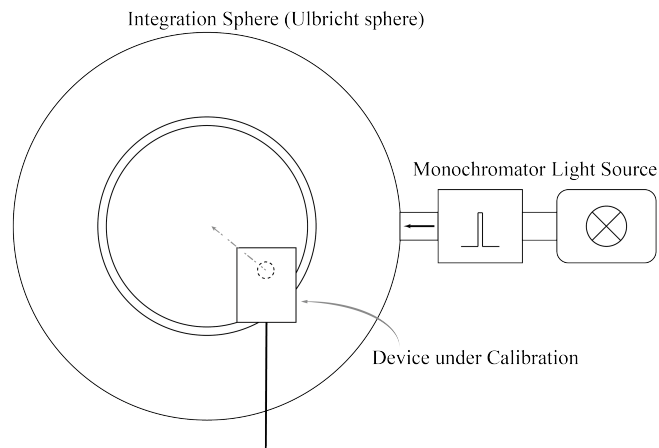


Fig. 3.11. Diagram of experimental set-up

To mitigate the temporal noise, 5 images were taken and averaged together. The lens was assumed to be axial symmetric and thus only a quarter of the image plane needed to be analysed, the remaining three quarters being deduced. The original signal turned out to be noisy with high density of spikes. In order to eliminate such noise, a 2-D Gaussian filter was applied through a convolution of the signal, as shown in Figure 3.12, where the signal surface was smoothed. Its normalized isoheight plane was illustrated by the color gradient, in which light intensity can be noticed being impaired from the origin (the center of image plane) to the boundary.

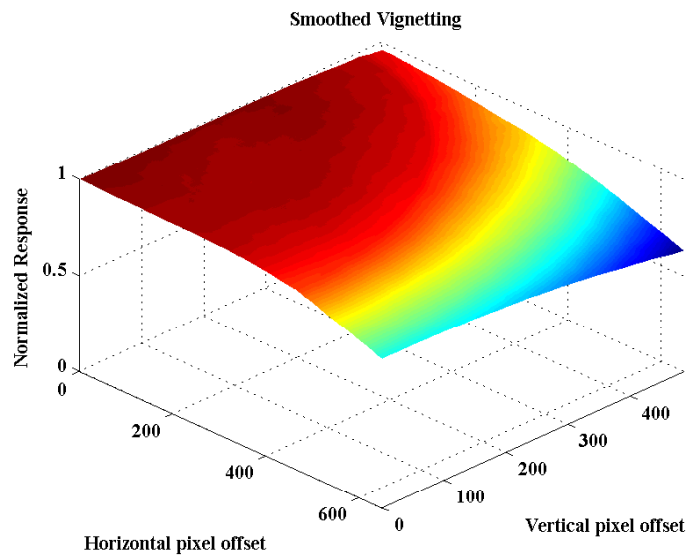


Fig. 3.12. Surface of response attenuation due to vignetting

Using the normalized surface of attenuation, the vignetting was approximated by a 4th-

order polynomials of $\cos(\alpha)$ to describe the combined effect of multiple factors, where α represents the off-axis angle, as given in Equation (3.4). The RGB channels were merged using the coefficients in Section 3.3.1 for calculating the value of normalized luminance V in Equation (3.4). Optimized with the least-error in the ℓ_2 norm space, the function was fitted over the 2-D surface. The fitting results are partially illustrated in Figure 3.13 with deviation from the center in 1-D along the cross section of the horizontal axis on the image plane. The coefficients are listed in Table 3.1. The relative RMSE is equal to 2.2%, and the R^2 coefficient of determination is equal to 0.961.

$$\sum_{i=0}^4 a_i \cdot \cos^i(\alpha) = V \tag{3.4}$$

Table 3.1 – Optimized coefficients

a_0	a_1	a_2	a_3	a_4
1.42	-12.1	33.4	-32.0	10.3

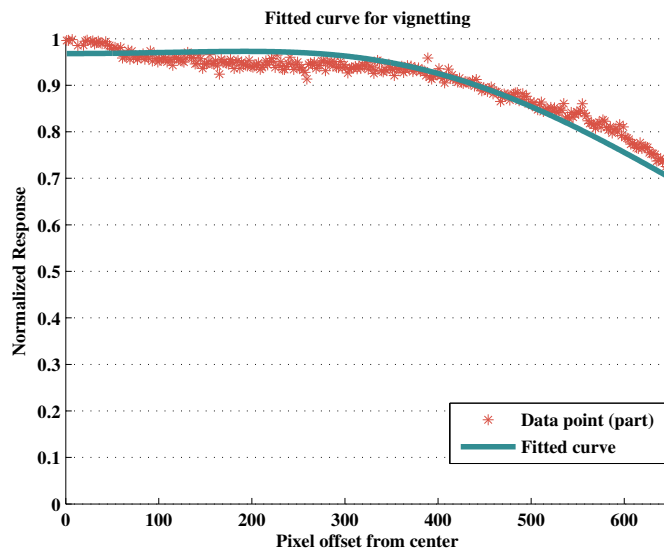


Fig. 3.13. Fitted curve for vignetting effect

3.3.3 Response curve

Linear response, in many ways, is a compelling system property, since it offers simplicity in both modelling and computing. Although the linear region of a photo-diode is commonly used to measure the number of captured photons, gamma correction is usually employed by camera manufacturers to compress the response of pixels in order to match the non-linear nature of the sensation of human eyes. An experiment was performed to evaluate the response

curve and the linear region of the image sensor. The experimental set-up is illustrated in Figure 3.14 where a class-B luminance meter (Minolta LS-110, with $\pm 2\%$ accuracy) substitutes the spectroradiometer to quantify the luminance of exiting light flux from the integration sphere as a reference. The shutter of the image sensor was set at 6 different speeds from 125 ms to 4 s so that both the saturated region and non-responsive region were covered respectively. The luminance at the exit port of the integration sphere was adjusted to range from 150 to 3900 cd/m^2 .

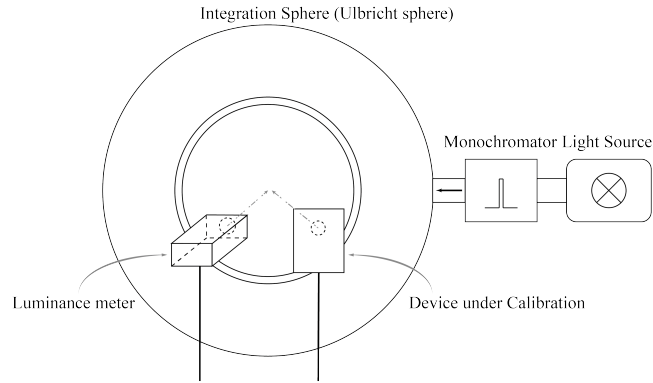
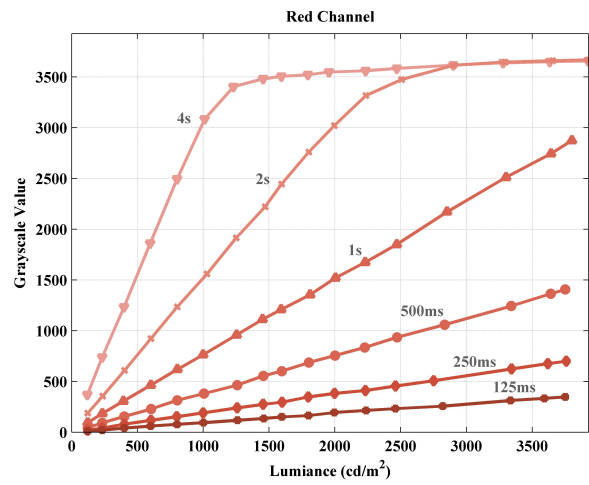


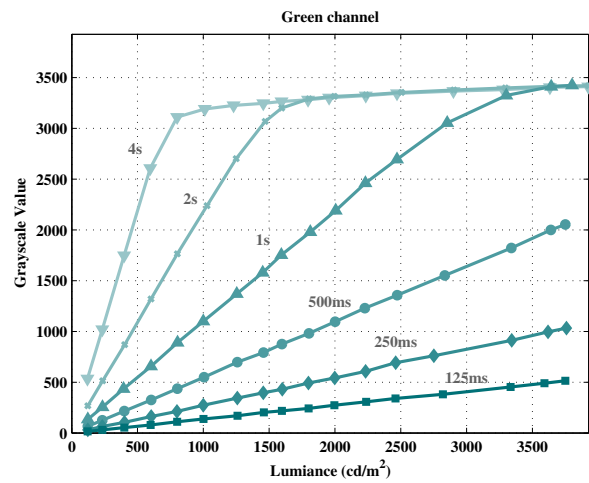
Fig. 3.14. Diagram of experimental set-up

The response curve of the RGB channels is illustrated in Figure 3.15. The response of each channel shows conspicuous linearity from above the noise floor upto a 3300 gray-scale value. Only the linear region of the response curve was used as a valid sensing range for luminance detection. Together with the weightings of RGB channels obtained in Section 3.3.1, the luminance L measured by a group of 4 neighbouring pixels (R, G_1, G_2, B) can be fitted by Equation (3.5) according to the integration time Δt , where C_g is the coefficient to be determined and R, G, B are the gray-scale values of corresponding pixels and G is the mean of G_1 and G_2 . Using the least-square norm as the objective function, the optimized coefficient C_g was computed with data points pertaining only to the linear response region. The corresponding fitted response curve with data points is presented in Figure 3.16 a). The relative error compared to the reference luminance given by the luminance meter is illustrated in Figure 3.16 b); it is bounded by 2% and shows a mean relative error of 0.81%.

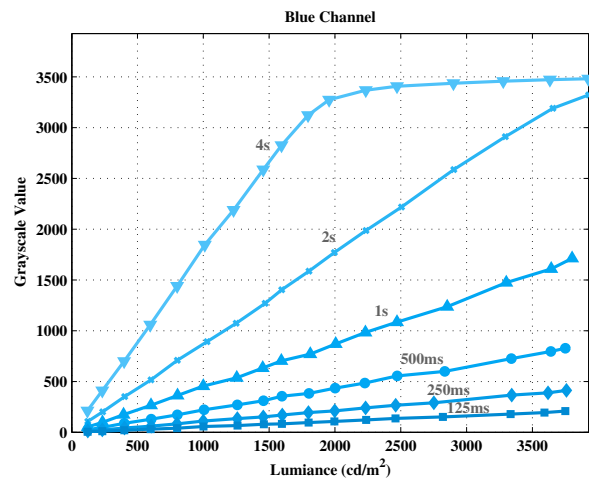
$$L = C_g \cdot \frac{w_1 R + w_2 G + w_3 B}{\Delta t} \quad (3.5)$$



(a) Red channel



(b) Green channel



(c) Blue channel

Fig. 3.15. Response of RGB channel versus luminance at 6 shutter speed

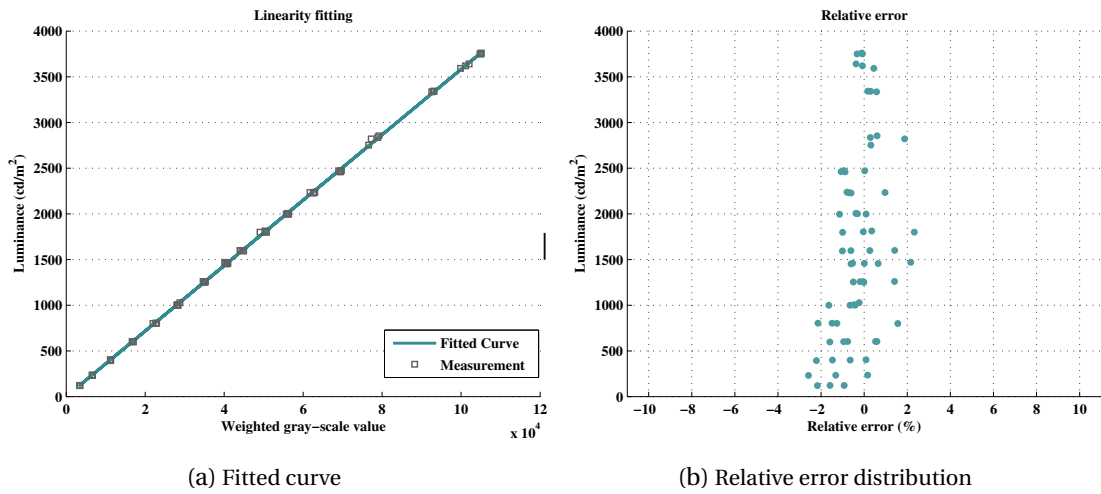


Fig. 3.16. Luminance monitoring by the calibrated imaging system and its error distribution

Owing to the imperfection of the lens, an imaging system with a wide-angle lens also suffers from linear and non-linear distortions. A field-test experiment with a standard chessboard was conducted first to determine the distortion coefficient and correct it during computation. Above all, the imaging system was corrected with optical glass filters for its spectral response and rectified digitally for its vignetting, response curve and geometric distortion. The device is able to cover a luminance detection range of $3.78 \times 10^9 \sim 1.2 \times 10^2 \text{ cd/m}^2$ (150 dB), the maximal mapping resolution reaching 1.2 million pixel groups, each pixel group being able to sense one single subdivided sky patch.

3.4 Empirical validation

The common daylight simulation approach is based on standard sky luminance models, their oversimplification contributing to a noticeable mismatch compared to a real sky and therefore to pronounced simulation errors [82], when the time scale is at the level of minutes or even seconds. By substantially expanding the volume of input data and thus increasing the resolution of the sky luminance mapping, the HDR imaging based sky luminance monitoring technique can reduce the discrepancy with real skies, which features complex patterns of clouds, high contrast sky regions as well as the direct sun orb. The ground is another factor contributing to simulation errors. A common practice is to model it as a lower hemisphere fraction with a 20% typical constant reflectance. In fact, the ground is complex in reality. Its reflectance is manifold and variable; it can reach as low as 7-9% for clean asphalt or slate and as high as 60-80% for snow. In addition, it is problematic to model the surrounding buildings or vegetation as a flat surface or a homogeneous hemisphere. The HDR luminance monitoring method can potentially reduce this discrepancy by real-field measurement in high resolution, which at the same time saves the efforts in modelling the landscape. After deliberate calibrations and parameter optimization, the embedded photometric device is able to map both the sky vault and ground in a subdivision with 1.2 million luminance patches: its

wide luminance detection range is able to cover the luminance at two extremes of both the direct solar orb and surrounding shadowing objects. This section evaluates its performance regarding the accuracy in physically based rendering, horizontal illuminance computing, and solar position tracking and intensity monitoring.

3.4.1 Image rendering

Merging every 4 neighbouring pixels into a group, the image sensor with 5 million pixels was divided into 1.23 million groups, each detecting the luminance of a patch of the sky vault or the ground in an unique direction from the lens. Multiple exposures (0.5 s in total) of the image sensor were controlled and image acquisition was pre-processed by the FPGA fabric part of the processor. Then the HPS part of the processor synthesised multiple frames into luminance values and mapped each pixel onto a single sky or ground patch, based on the parameters acquired in Section 3.3. The resolution of luminance mapping is variable and can be downgraded by sub-sampling with the application of low-pass digital filters for anti-aliasing effects. In the context of this chapter, the maximal resolution was retained for the evaluation of accuracy performance. Since the focal length (2.5 mm) of the lens is infinitesimal compared to the object distance (to the principal plane) in the camera coordinates, including the sky, the sun disk, clouds, and landscape on the ground, objects can approximately be regarded as a single entity and the lens can focus on the infinity. It takes the processor 1.3 seconds to accomplish the whole course of HDR imaging acquisition, data processing, and luminance mapping.

For image rendering of a scene, the RADIANCE software, a physically-based lighting simulation program package largely developed by Greg Ward [155], was employed with the backward ray-tracing algorithms computing the daylighting in buildings. The two sub-programs, `rtrace` and `rpict` [155], were employed and run on the HPS part of the processor to render the scene.

A typical office with an unilateral façade was selected as the study target. The calibrated embedded device was positioned in front of the façades with its lens axis in the orthogonal plane of the façades. The FOV of the lens was aimed at the sky vault facing the façade. The absolute geographical coordinates of the test room are not necessary for the lighting computing, since the daylighting in the space was exclusively contributed by the daylight flux through the unilateral façades: a relative coordinate was established by the imaging system for the sky vault and ground.

A 3-D model of the considered office space was created for the device. After the luminance map of the hemisphere seen by the camera, comprising half of the sky vault and half of the ground, was monitored, it was compiled with the scene model into an octree file for the RADIANCE program in the device. The embedded device was able to perform the rendering of

the scene in 79.2 seconds with 1.41×10^6 tracing rays for a coarse image, with splotchy patterns in the shadowed zones. In fact, the computing time is largely contingent on the resolution of the luminance map. If the sky patches are sub-sampled into 145 patches according to the Tregenza or Klems subdivision [156], the time in rendering the same scene can be reduced to 1/3 of that in full resolution (20-30 s). With high quality parameters, maximal luminance map resolution, and long time rendering, the scene of the office was rendered with a smooth shadow on the wall as illustrated in Figure 3.17 b) for a partly cloudy sky. For comparison, the direct normal and diffuse horizontal irradiance was simultaneously measured on the rooftop of the office building; a common practice employing the Perez all-weather sky model [86] using the monitored irradiance as inputs is illustrated in Figure 3.17 a) rendering the scene of the same office room. The merits of the HDR imaging based sky monitoring approach can be illustrated by the neat contour of the sky patterns and landscape from a viewing perspective towards the façades, including the surrounding buildings and vegetation which is extremely difficult to model correctly. In addition, the HDR imaging approach is closer to the reality than that employing the Perez sky model as in common practice according to the mismatch in the shadows on the desks and floor in Figure 3.17.

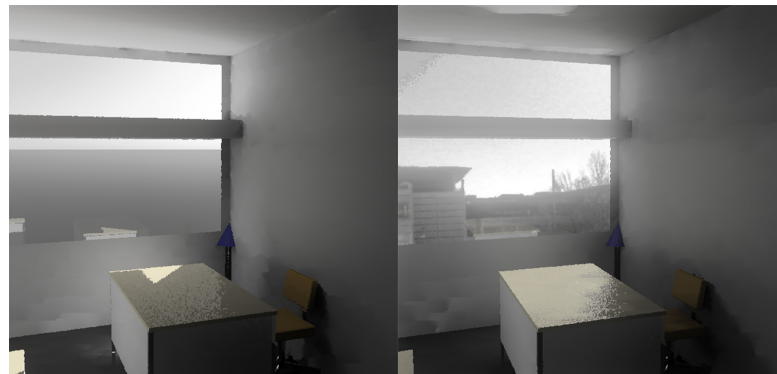


Fig. 3.17. Rendering of a office room by a) Perez model b) HDR imaging based sky luminance map

3.4.2 Work-plane illuminance

While Section 3.4.1 qualitatively assesses the accuracy of the embedded device in image rendering of daylit environment, this section investigates the computation of intra-scene horizontal work-plane illuminance distribution, cross validated with the monitored value issued from an array of real lux-meters as a reference. In this section, the on-board RADIANCE program was used again for computing the illuminance distribution based on ray-tracing and Monte-Carlo integration techniques. In order to outline its performance, the embedded photometric device based on the HDR sky monitoring approach was compared with a common practice employing the Perez all-weather sky model based on weather data.

Experimental set-up

A lighting test module (DEMONA, interior size: $6.4 \times 2.9 \times 2.6 \text{ m}^3$) was selected as the experiment site, mimicking a typical office room with 3 pairs of desk and chair. The module was equipped with an unilateral double-glazed façade (6 elements) facing towards south, showing a 0.62 window to wall ratio in total, as presented in Figure 3.18 a). To improve simulation accuracy, both the dimensions and the reflectance of each surface composing the module were modelled in accordance to reality. In this experimental set-up, the geometric dimensions and relative position of each furniture in the module were measured by a range finder (Leica DISTO), establishing relative coordinates of all the objects. The chromatic coordinates and reflectance values of each surface material were measured by a chromameter (MINOLTA CR-220) in the xyY color space with a CIE D65 light source, including the ceiling, the wall, the floor, the window frame, and each furniture surface. As RADIANCE adopted the RGB color space, the measured xyY chromatic coordinates were converted into the RGB color space based on pre-defined primaries in RADIANCE by matrix multiplication. The specularity, characterizing the ratio of the direct component in reflection, was measured by using a gloss meter (MINOLTA GM-060). It characterized the proportion of specular component at the incident angle of 60° and was supposed to approximate the specularity, despite its minor dependence on the incident angle. Furthermore, the roughness of each material was assigned a value between 0 and 0.2 according to the particle size of the surface. The virtual model of test module is illustrated in Figure 3.18 b).

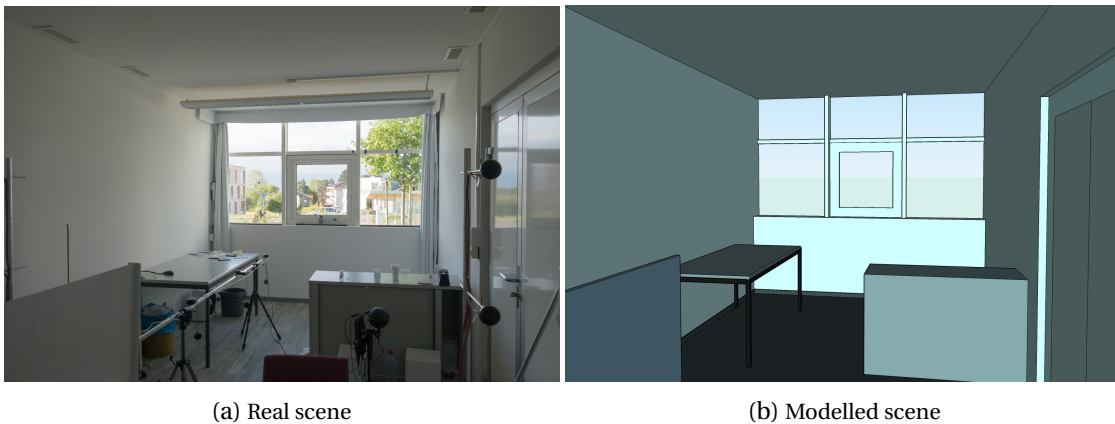


Fig. 3.18. The daylighting test module with unilateral façades (DEMONA)

For the monitoring of work-plane illuminance (WPI), five lux-meter sensors (MINOLTA T-10A, with $\pm 2\%$ accuracy) were placed in the test module at the workplane height of 0.8 m, with their sensible surface aligned upward in the horizontal plane. The sensors were arranged in a line and fixed at the distance of 1 m, 2 m, 3 m, 3.9 m and 4.7 m from the façade, as shown in Figure 3.19. Each lux-meter was connected in parallel to a data logger ensuring that the measurement from each sensor can be acquired simultaneously. Accordingly, for the daylighting simulation, 5 virtual sensors were placed at identical positions in the modelled scene as in the real module. Since the virtual sensors were commonly point receptors in

RADIANCE, 9 sampling points covering a $2 \times 2 \text{ m}^2$ square were defined and averaged to reproduce the sensing area of each lux-meter and to reduce the spatial noise for simulated horizontal illuminance.

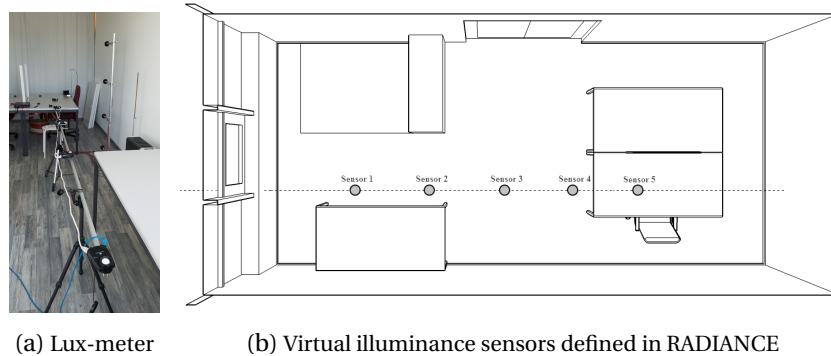


Fig. 3.19. Sensor position for monitoring horizontal illuminance

During the experiments, three major equipments were installed close to the daylighting test module: i) the HDR embedded photometric device (under test), ii) a pyranometer (Delta-T BF3, accuracy $\pm 12\%$) monitoring the direct normal and diffuse horizontal irradiance (for comparison with the Perez sky model), and iii) a lux-meter array (acquisition of reference illuminance values for cross validation), as illustrated in Figure 3.20.

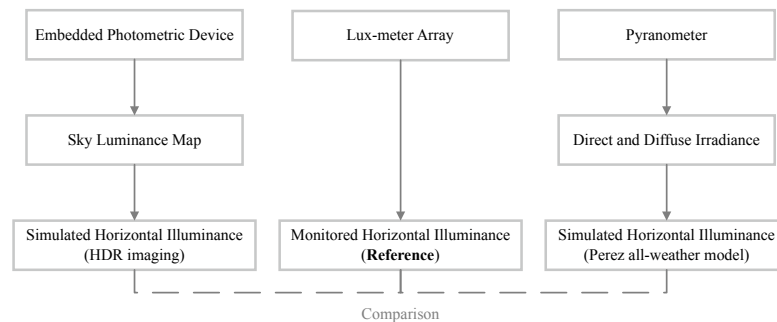


Fig. 3.20. Employed equipments and their feature in experiments

The embedded photometric device (EPD) was anchored in front of the test module with its lens axis aligned in the plane orthogonal to the façade, as illustrated in Figure 3.21. The device was adjusted with 2/3 of its FOV covering the sky vault and 1/3 of that covering the ground fraction, as the sky is responsible for the main daylight contribution through the façade. The process of the luminance monitoring of the sky and landscape, luminance mapping, and computation of horizontal illuminance distribution were executed on-board independently. The pyranometer was positioned on the rooftop without shadowing. Its monitoring of the direct normal and diffuse horizontal irradiance was used as input for the Perez all-weather sky model during the simulation of the WPI distribution. The three apparatus were synchronized during the data monitoring, in order to achieve simultaneous illuminance simulations and measurements. To reach a high accuracy, identical sets of simulation parameters in RADIANCE

Chapter 3. Embedded photometric device

were employed based on the backward ray-tracing and Monte-Carlo integration techniques for both approaches based on monitored luminance distribution of the sky and based on weather data and a sky model respectively, with parameter set '-ab 5 -ad 1024' [155] for ambient calculation in RADIANCE. As a trade-off between computation accuracy and time consumption, the synchronization was made using 15 min sampling time intervals for the three apparatus.



Fig. 3.21. The embedded photometric device positioned in front of the unilateral façade

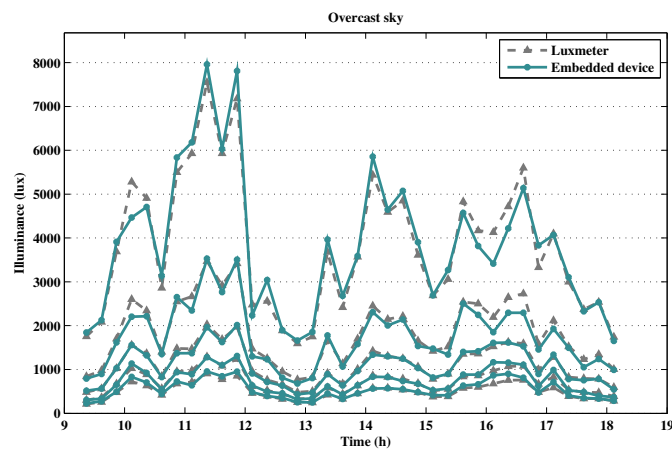
To study the accuracy of the simulated WPI distribution using the EPD, partly cloudy days with predominant overcast and clear sky, when most of the daytime was dominated by overcast or clear skies, and the rest of time was partly cloudy, were considered as the two critical conditions to investigate daylighting without indoor artificial lighting. The experiments were conducted from 9 a.m. to 6 p.m. in the test module from May 08th to 09th, 2017 on the EPFL campus in Lausanne, Switzerland; the workplane horizontal illuminance was simulated by the EPD, cross validated by measured values of the lux-meter array.

Predominant overcast sky

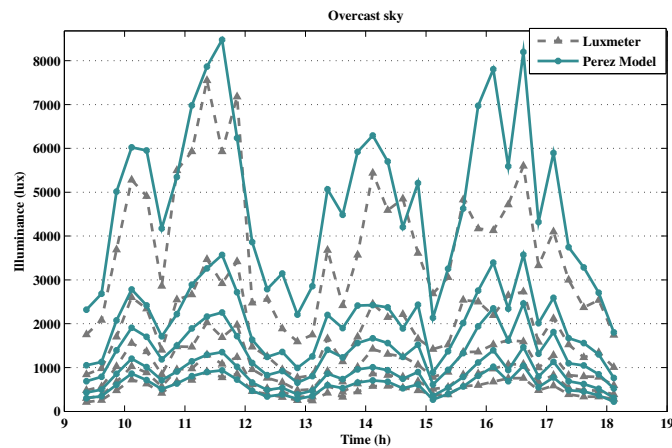
The workplane horizontal illuminance computed by the EPD based on the monitored luminance distribution of the sky (and ground) is illustrated in Figure 3.22 a) by the green solid lines for a predominant overcast sky. The five curves stacked sequentially from top to bottom respectively for the illuminance values simulated for points at a 1 m distance to a 4.7 m distance from the façade. The monitored horizontal illuminance values by the lux-meter array are denoted by the grey dotted lines and used as a reference to assess the simulation error. Analogously, the workplane horizontal illuminance simulated based on the Perez all-weather model is represented by green lines in Figure 3.22 b). Although the monitored illuminance of each lux-meter fluctuated throughout the day, the HDR sky monitoring approach outperformed the Perez sky model in the simulation of WPI distribution, the result of which was closer to the monitored value (grey dotted line) as shown in Figure 3.22 a) and b). Using monitored

3.4. Empirical validation

reference value by the lux-meters, the relative error of the two methods was determined; Figure 3.23 illustrates the results for the 5 sensors denoted by gradient shaded bars and grouped along the time line (e.g. for Sensor 1 at distance of 1 m and Sensor 5 at distance of 4.7 m from the façade). The relative error bars are showing the advantage of employing the HDR sky monitoring approach compared to the standard sky model. The average error of the five WPI values computed using the EPD in case of a predominant overcast sky are equal to 6.4%, 7.5%, 4.1%, 5.0%, and 7.0% respectively; those obtained by the simulation based on the Perez sky model reach respectively 32%, 22%, 29%, 23% and 23%. The overall 3-4 times higher error rate of the Perez sky model can be explained by the fact that it neglects high contrast patches of the sky vault and the ground fraction, where the complex cloud patterns and inhomogeneous nature of the landscape can be major factors for errors.



(a) HDR imaging approach



(b) Perez all-weather sky model

Fig. 3.22. Workplane horizontal illuminance assessed by two daylighting simulation methods compared with lux-meter values for a pre-dominant overcast sky [3]

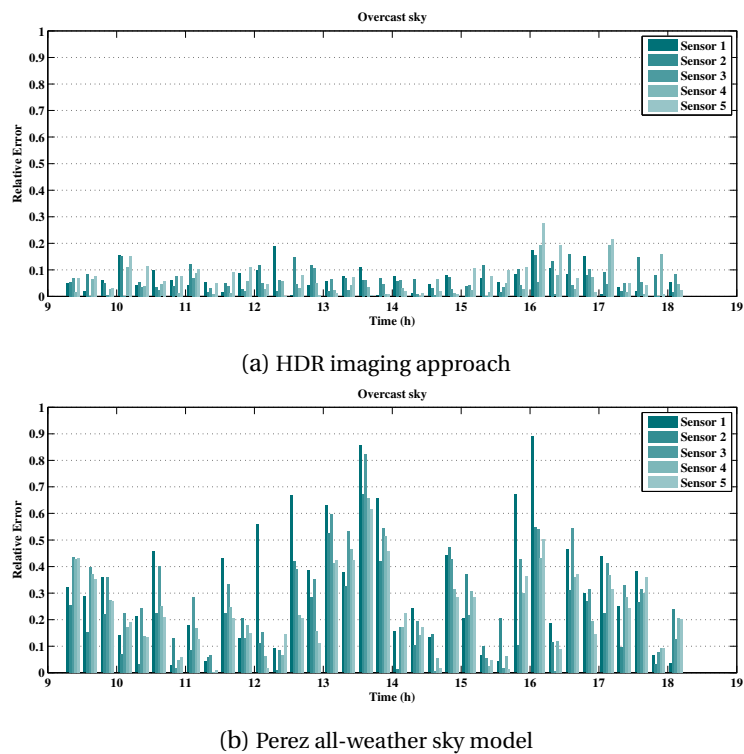
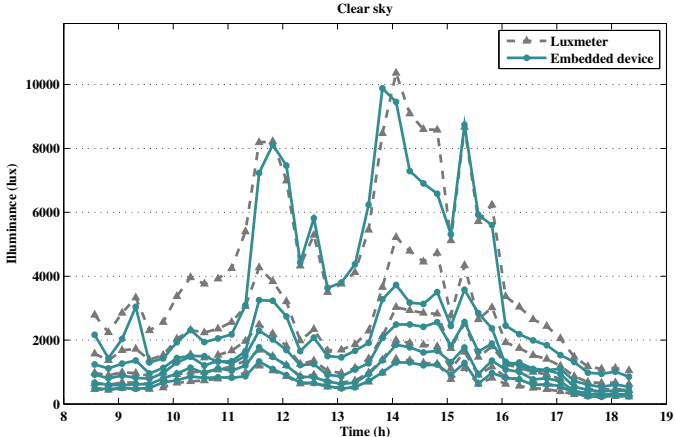


Fig. 3.23. Relative error of the 5 computed workplane illuminances compared with lux-meter values for a pre-dominant overcast sky [3]

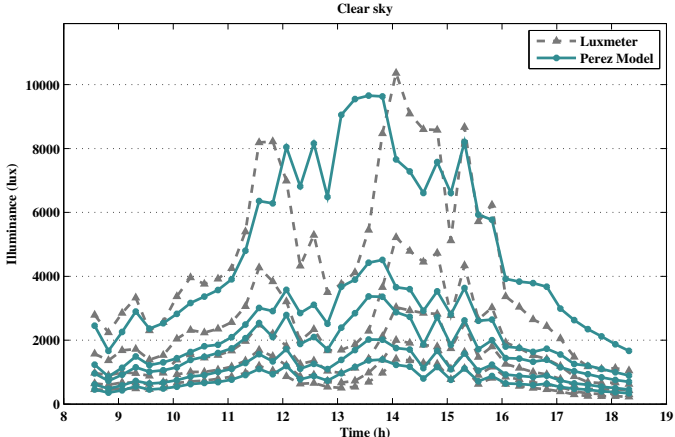
Predominant clear sky

For a predominant clear sky, the WPI distribution simulated by the EPD based on monitored luminance distribution of the sky is illustrated in Figure 3.24 a), where the stacked lines represent the 5 computed values (green) as well as reference values monitored by lux-meters (grey) at identical positions respectively. Similar to Section 3.4.2, the simulated WPI values based on the Perez sky model are shown in Figure 3.24 b) together with the monitored illuminance values (grey). According to their mismatch with the reference values, the HDR imaging based sky luminance monitoring approach shows higher concordance with the monitored illuminance values than the common practice employing the Perez sky model, thanks to the high-resolution sampling inputs. The relative error of simulation compared to the reference was also calculated and is illustrated in Figure 3.25 a) and b) for the two approaches respectively. The Perez all-weather sky model approach shows overall a larger error rate than the HDR sky luminance monitoring approach in the transient daylighting simulation, which is likely due to the oversimplification of sky models which are levelling the high contrast patches of the sky vault and the ground fractions. It can also be noted from the figure, on the time line 13:00 - 14:00, when the sun was occluded by thin clouds, that the relative error of the Perez model exceeded 100%, i.e. the sky model shows a pronounced discrepancy in regards to the real sky. On the opposite, the HDR sky monitoring approach must be given merits for its accuracy; however, for the sake of clarity and comparison of the error bars, Figure 3.25 was not

scaled down to include the highest peaks. The average over-all relative error of the 5 computed illuminances throughout a day with a pre-dominant clear sky is respectively equal to 25%, 22%, 9.7%, 8.9%, and 11% for the HDR imaging based sky monitoring approach and 37%, 32%, 36%, 31%, and 28% for using the Perez all-weather sky model. Although the former approach shows lower relative errors than the latter, the first two simulated illuminances, at 1 m and 2 m distance from the façade, for the HDR imaging based approach, were prone to noticeable errors compared with the other three locations deep into the test module; this can also be noted from the time line 9:00-11:00 in Figure 3.25 a), when the sky was entirely clear without any thin clouds occluding the sun. This can possibly be attributed to the insufficient sampling of the sun disk, since for a clear sky, the solar disk is one of the major sources of daylight. The sky background together with the sun was defined as the 'glow' material in RADIANCE program, which sampled randomly the sky vault. With a low probability for sampling rays to reach the solar disk due to its relatively small dimension, there is a high probability of underestimating the overall sky luminance as well as the corresponding daylighting contribution in the test module.

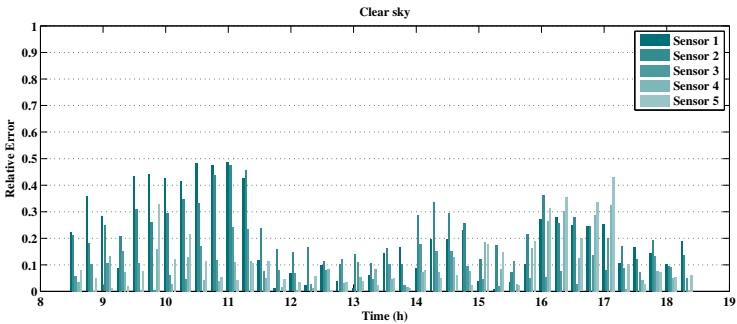


(a) HDR imaging approach

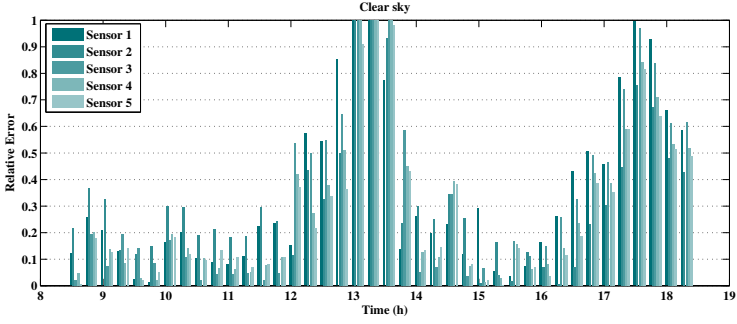


(b) Perez all-weather sky model

Fig. 3.24. Workplane horizontal illuminance assessed by two daylighting simulation methods compared with lux-meter values for a predominant clear sky [3]



(a) HDR imaging approach

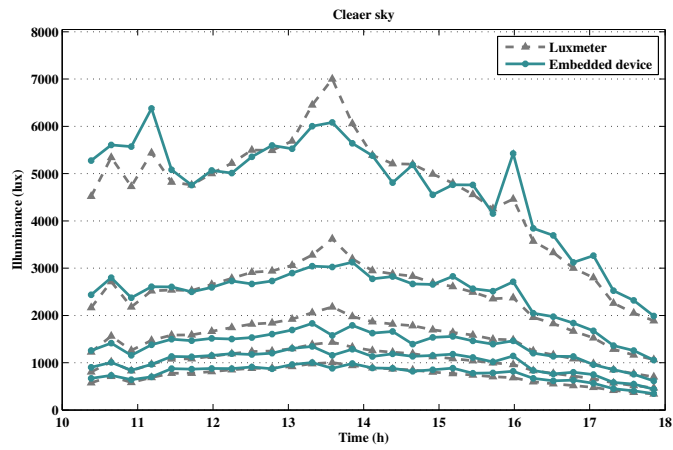


(b) Perez all-weather sky model

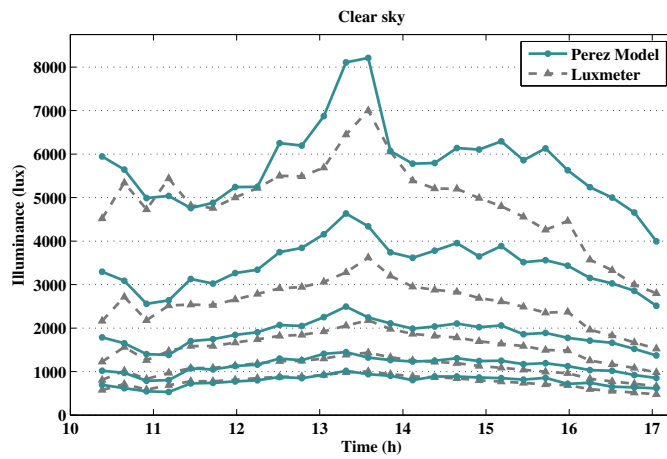
Fig. 3.25. Relative error of the 5 computed workplane illuminances compared with lux-meter values for a predominant clear sky [3]

Improvement of sampling

The issue of insufficient sampling of the high contrast sun disk for a clear sky can be addressed by the extraction of the solar patch and by using concentrated sampling. As the maximal luminance of the sun orb observed at sea-level in a clean atmosphere is approximately $1.6 \times 10^9 \text{ cd/m}^2$ [157], the extraction of the solar disk was based on a threshold of solar luminance of $5 \times 10^8 \text{ cd/m}^2$, as well as a subtending angle on the monitored luminance map from the embedded device equal to 0.53° in the FOV. The extracted sun disk is defined as a separated component in RADIANCE as a 'light' instead of a 'glow' material [155] for the concentrated sampling on the sun. With this improvement, the experiment with the EPD was repeated on another day with a predominant clear sky from 10:00 - 18:00, the sky condition being clearer (less thin cloud presence) than that in Section 3.4.2. The workplane horizontal illuminance of the 5 virtual sensors are illustrated in Figure 3.26 and compared to the monitored values monitored by lux-meters. The two front locations, at 1 m and 2 m distance from the façade, show better concordance and a lower discrepancy with the reference illuminance values than those shown in Figure 3.24 a). The relative error for the two virtual sensors, as presented Figure 3.27, are significantly reduced, compared to Figure 3.25 a). The average error throughout a day with a clear sky is improved respectively to 7.5%, 6.1%, 8.7%, 5.3%, and 8.2% for the HDR imaging based sky monitoring approach in comparison to the results presented in Section 3.4.2.

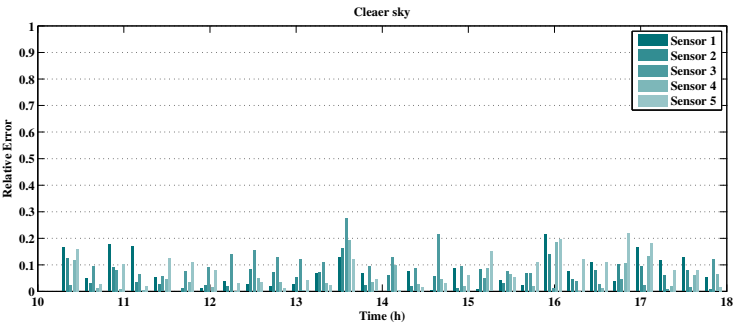


(a) HDR imaging approach with improved sampling

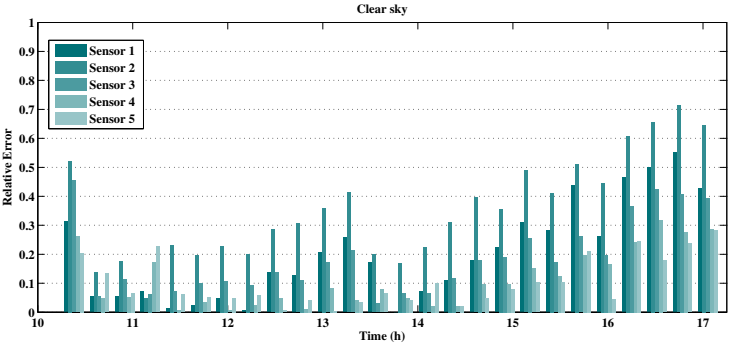


(b) Perez all-weather model

Fig. 3.26. Workplane horizontal illuminance assessed by two daylighting simulation methods with lux-meters values for a clear sky



(a) HDR imaging approach with improved sampling



(b) Perez all-weather sky model

Fig. 3.27. Relative error of the 5 computed workplane illuminances compared with lux-meter values for a clear sky

3.4.3 Solar tracking

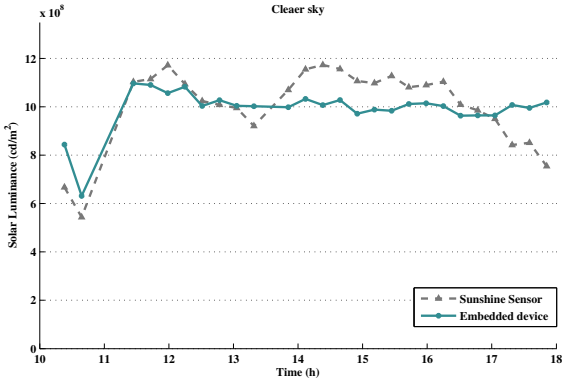
The solar orb providing a substantial contribution to daylighting in buildings during clear sky conditions, an accurate mapping of the solar disk from the image plane to the world coordinates would have a noticeable influence on the overall accuracy of daylight simulation based on the EPD. This section presents the evaluation of the monitoring accuracy of the sun orb by the EPD, with regard to solar luminance and sun position.

The device was positioned with the lens axis aligned towards the south, as shown in Figure 3.21. The solar position was determined according to centroid of a group of pixels on the luminance map with values larger than the threshold defined in Section 3.4.2; their size corresponded to 0.53° angle FOV. The luminance of the solar patch was assessed by averaging 35 pixel groups identified above the threshold, which subtends 0.53°. According to its position on the image plane, the sun location was determined by applying the intrinsic and extrinsic matrix of the imaging system [158]. As reference, the solar luminance was also measured indirectly by using a pyranometer (Delta-T BF3, ±12% accuracy) that recorded the global and diffuse horizontal illuminance, and it was converted to solar luminance according to the solar position. The zenith angle (solar altitude) a_t and azimuth angle a_s of the sun can be calculated by Equation (3.6).

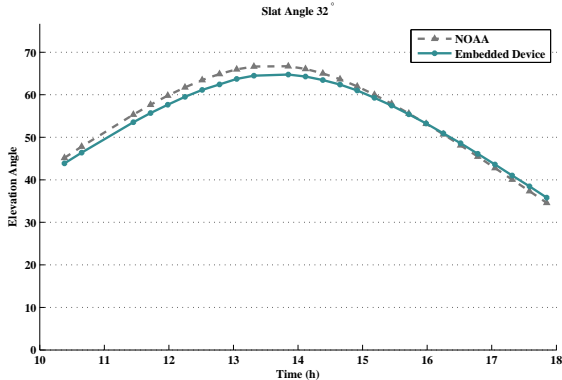
$$\begin{aligned}
 a_t &= \arcsin(\sin(l)\sin(\delta) - \cos(l)\cos(\delta)\cos(\pi t/12)) \\
 a_s &= \arctan\left[\frac{-\cos(\delta)\sin(\pi t/12)}{-(\cos(l)\sin(\delta) + \sin(l)\cos(\delta)\cos(\pi t/12))}\right]
 \end{aligned}
 \tag{3.6}$$

where t is the solar time in decimal hours, l is the site latitude in radians and δ is the solar declination in radians, defined by $\delta = 0.4093\sin(2\pi(J - 81)/368)$, where J is the Julian date [159]. The calculation of the sun position is based on the results obtained by National Oceanic and Atmosphere Administration (NOAA).

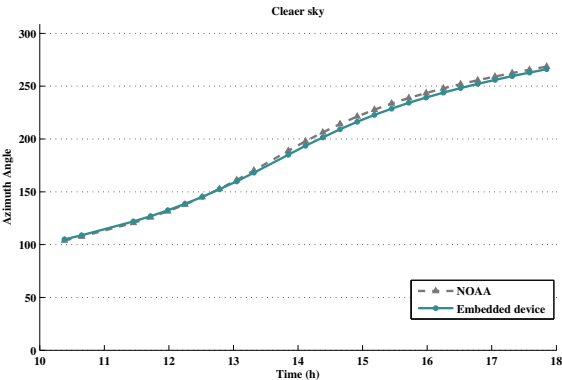
During one day with predominant clear sky conditions on Jun. 23th, 2017, the embedded photometric device tracked the sun luminance and position every 15 min from 10:00 to 18:00. The monitored solar luminance is illustrated in Figure 3.28 a) by a green solid line, and compared to the reference measurement obtained by a pyranometer (grey dotted line). Accordingly, the sun zenith and azimuth angle monitored by the EPD are illustrated in Figure 3.28 b) and c) respectively (green solid lines), together with the reference data (e.g. NOAA and pyranometer, in grey dotted lines). The average relative error (RMSE) throughout a day for the luminance of the solar disk monitored by the EPD is equal to 9.6%; those of the elevation angle and azimuth angle are equal to 2.4% and 1.3% respectively, demonstrating its reliability and accuracy in solar tracking.



(a) Solar Luminance



(b) Elevation angle of the sun



(c) Azimuth angle of the sun

Fig. 3.28. Solar luminance and position monitored by embedded photometric device

3.5 Conclusion

The accuracy of daylighting simulation can be strongly deteriorated by the mismatch between the luminance distribution of standard sky models used in simulation and that of real skies. By monitoring the luminance of the sky vault and the ground fraction with a high resolution

mapping, this mismatch can be substantially reduced especially when the time scale for simulation reaches minutes or even seconds. In this way, monitored luminance distribution of the sky overcomes the limitation of standard sky luminance models, most of which are based on weather data and average conditions obtained over multi-annual periods among various geographical locations. This chapter presents a compact embedded photometric device (EPD) comprising a FPGA processor and an image sensor used for real-time on-board daylighting simulations following an HDR sky luminance monitoring process.

A calibration procedure of the imaging system was set-up and validated with experimental data issued from the monitored luminance distribution of the sky vault. The calibration procedure includes the spectral response, vignetting effect, response and geometric distortion of the imaging system. Its spectral response was rectified by a short-pass and a long-pass filter, improving the relative spectral correction error f'_1 to 8.89%. The vignetting effect and geometric distortions were corrected and compensated by the processor. The dynamic range of the imaging system reaches 150 dB, covering a luminance monitoring range between $3.78 \times 10^9 \sim 1.2 \times 10^2$ cd/m²: the upper bound is high enough to monitor the extreme luminance of the sun orb and the lower bound is low enough to perceive a relatively dim landscape during daytime. This high resolution imaging system is able to map the sky vault and the ground fraction in 1.2×10^6 patches, which potentially alleviates the difficulty in modelling landscape, including buildings and vegetation.

The performance of the device was demonstrated using 'in situ' experiments in daylighting test modules for image rendering, horizontal illuminance simulation and solar tracking. Firstly, the device was able to accomplish a HDR sky luminance monitoring, luminance mapping and on-board image rendering (one image) in approximately 79 s tracing 1.41×10^6 rays, using on-board RADIANCE programs. The rendering of façades with outdoor views of the landscape showed a better concordance with reality compared to a common practice simulation employing the Perez all-weather model. Secondly, the accuracy achieved with the EPD in daylighting simulation of the horizontal illuminance was assessed comparing to a common practice employing the Perez all-weather model, using measurements by a lux-meter array as reference. For both predominant overcast and clear sky conditions, the embedded photometric device based on HDR sky monitoring was able to reduce the error of transient WPI calculation to $\frac{1}{7} \sim \frac{1}{3}$ of that of the common practice using standard sky models. The simulation accuracy was demonstrated experimentally to be improved thanks to the extraction of the solar direct component and application of concentrated sampling method for clear sky conditions. Finally, the device showed a quality in solar tracking, with relative average error 9.6% for solar luminance monitoring and below 3% in the sun position tracking.

Above all, the embedded photometric device demonstrated its merits in real-time daylighting simulations, in the response time, simulation quality, and adaptability. In the context of

building automation, the device can potentially be used for the control of shading, lighting or electro-chromic glazing to regulate daylight ingress and passive solar heat gain both for centralized and decentralized systems. Moreover, its capability in solar luminance monitoring and position tracking make it suitable for the solar photovoltaic (PV) power generation or control of the profile angle of the modules. In addition, the device accuracy in daylighting simulation can also be used for the analysis of lighting solutions in retrofitting process. If the resolution of the luminance map is downgraded to 145 Tregenza or Klems patches, the 5-phase matrix algebraic approach [160] can be employed to save computational loads, using pre-computed view matrix and inter-reflection matrices. The FPGA fabrics can be exploited to parallelize the computation massively. Investigation on its reliability and on its ability to accelerate the computing by employing the FPGA fabric part will be the subject of future work.

4 Wavelet compression on BTDF data

4.1 Introduction

The bidirectional transmittance distribution function (BTDF), which is used to characterize the light transmission of a complex fenestration system (CFS), commonly involves bulky volume of data that can be a challenge to data storage and transmission in lighting simulation tools and on compact platforms. This chapter introduces a compression scheme that is based on planar wavelet transform with three levels of decomposition to efficiently compress the BTDF of CFS and maintain fidelity in daylighting simulation. The root-mean-square error (RMSE) and transmittance error (TE) of compressed medium-resolution BTDF using three different wavelet bases are evaluated for five paradigmatic CFS samples at various compression ratio. Based on the results, the generic error due to compression did not exceed 20% with CDF9.7 basis for compression ratio up to 200. In the case of rendering an image of a scene in which a CFS was installed at the upper daylighting section of an unilateral façade, error began to be noticeable at a compression ratio above 70. The uniformity factor g_1 was discovered to be relatively sensitive to compression (below 15% error), while the average horizontal illuminance and DGP (below 10% error) were immune to compression ratio below 100. Compression was also investigated on a high-resolution BTDF of external Venetian blinds in the work-plane illuminance (WPI) simulation. With a HDR imaging technique based sky luminance map, the WPI simulation had unnoticeable error using compressed BTDF within a compression ratio of 100. The chapter is based on the article "Performance assessment of BTDF compression based on wavelet transforms in daylighting simulation" submitted to the "Solar Energy" journal by Wu et al.

4.2 Methodology

Wavelet transform is able to concentrate information from massive data sets onto a limited number of coefficients [161], with multi-resolution decomposition as a merit. Wavelet transform has been widely used to compress statistical and computer graphic data [162]. For a

continuous signal denoted by function $x(t)$ and defined in L_2 Hilbert space with finite energy, the signal can be mapped into ℓ_2 space by wavelet transform and can be denoted by the linear combination of basis function as shown in Equation (4.1), where $\phi_k(t)$ and $\psi_m(t)$ are the scaling and wavelet basis functions respectively, $\hat{\phi}_k(\mu)$ and $\hat{\psi}_m(\mu)$ are their dual basis, and k and m are integer indices of the basis functions [163]. In the special case where basis functions are orthogonal and normal (i.e., orthonormal), dual bases are equal to the scaling and wavelet basis functions. In this way, the signal can be expanded in a series of basis functions, in which the coefficients are merely inner products with duals, as shown in Equation (4.1).

$$x(t) = \sum_{k \in \mathbb{Z}} \langle \hat{\phi}_k(\mu), x(\mu) \rangle \cdot \phi_k(t) + \sum_{m \in \mathbb{Z}} \langle \hat{\psi}_m(\mu), x(\mu) \rangle \cdot \psi_m(t) \quad (4.1)$$

If $x(t)$ is compactly supported, then a finite number of coefficients can represent the signal with scaling and wavelet basis functions, of which the information is concentrated on the coefficients of scaling basis functions. Additionally the basis functions need to satisfy the conditions of wavelets, including refinement basis, nested space, and space orthogonality. For more detailed theory on wavelets, readers can refer to [164, 165]

The routine used to compress the BTDF data (in tabulated format) is illustrated as a flow chart in Figure 4.1. First, the wavelet transform was performed on the BTDF data over the two emergent hemisphere dimensions (θ_t and ϕ_t) with three levels of decomposition (depth). The coefficients were computed at the coarsest level for one scaling basis function group that represented the approximation, and were computed at finer levels for nine wavelet basis function groups that stored the BTDF details. In this chapter, the wavelet transform was applied only on the emergent hemisphere of the BTDF, of which the data were mapped onto a 2-D matrix. To avoid the effects of implicit discontinuity at the edges of matrices, the defects were addressed with circular and mirror padding along the azimuth and in the zenith angle direction, respectively, since the BTDF connected end-to-end on the exit unit hemisphere. Second, as the information of BTDF was concentrated on the coefficients of scaling basis functions, the compression was realized using Equation (4.2) to quantize the coefficients. In Equation (4.2), \mathbf{w} is an array of coefficients, and u and v are scalar parameters adjusting the quantizing step width. The u and v parameters tune the sparsity of quantized coefficients, determine the compression ratio, and regulate the compression error.

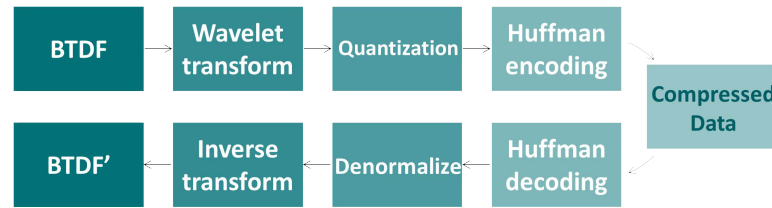


Fig. 4.1. BTDF data compression routine based on wavelet transform

$$\lfloor \frac{\mathbf{w}}{\max(\mathbf{w})} \cdot 2^v \cdot (1 + u \cdot 2^{-11})^{-1} \rfloor \quad (4.2)$$

After quantization, coefficients of negligible magnitude (below a pre-defined threshold based on compression ratio) were approximated to nil. Commonly, a substantial portion of the coefficients, particularly those of the wavelet basis functions, are equal to zero (high sparsity). To increase the efficiency of compression, the consecutive zeros were symbolized in a compact form. Next, non-trivial coefficients, together with the symbols representing consecutive zeros, were Huffman encoded, which generated a variable-length code based on the frequency of occurrence, with shorter bits representing more frequent symbols [166]. After encoding, the BTDF data were compressed and the size of compressed data were compared with that of the original BTDF to calculate the compression ratio.

Inversely, the new BTDF data were synthesised by Huffman decoding, followed by de-normalization that rescaled the coefficients back to the original range before quantization. Following the inverse wavelet transform, the BTDF data were reconstructed. Its RMSE (root mean square error) of the restored BTDF was computed, comparing to the original BTDF data. Since the routine was essentially a lossy compression due to quantization, there was a trade-off between the error (quality) and compression ratio. In this chapter, since the mapped BTDF is fundamentally similar to an image, three wavelet bases commonly used in image compression were investigated to assess the performance of compressing the BTDF data of a group of CFS. The employed wavelet bases included an orthogonal basis Daubechies 10 (DB10) [167], a bi-orthogonal basis 6.8 (Bior6.8), the Cohen-Daubechies-Feauveau basis 9.7 (CDF9.7) [168], in which the tailing numbers denoted the number of vanishing moments [169] of the wavelet basis for decomposition and reconstruction, if separated by a period. Only 6-10 vanishing moments were allowed in this chapter for compressing BTDF because of the compression efficiency. Large vanishing moments corresponds to lengthy support of basis, which involves further expansion of matrices to eliminate boundary defects, which can affect the compression ratio negatively.

4.3 Compression on medium-resolution BTDF data

4.3.1 BTDF generation

To assess compression performance, five paradigmatic CFS panels with distinct light transmission characteristics were selected, including a) a white opalescent plexiglass, b) CFS3 (a prismatic panel), c) Lumitop (a sunlight re-directing glass), d) Venetian blinds, and e) Fabric blinds, as shown in Figure 4.2. These CFS panels were selected because of their distinct material properties or internal substructures that redirect light in different ways. For instance, the opalescent plexiglass is ultra-diffuse, which smooths transmitted light rays, while the prismatic panels maintain the sharpness of light and redirect light in a different direction.

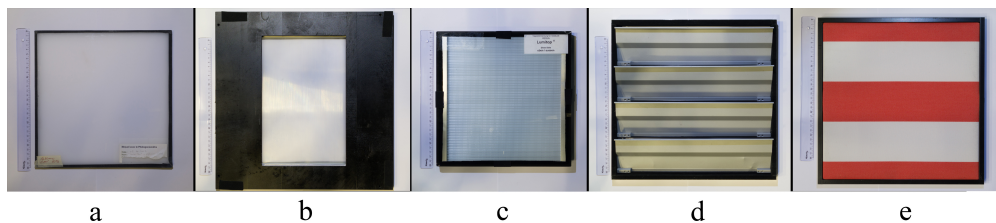


Fig. 4.2. CFS panels with different light transmitting behaviour

The BTDF of the five CFS panels were monitored with a CCD (charge-coupled device) imaging based bidirectional goni photometer [170, 104], as shown in Figure 4.3. A collimated light beam from an intense source was shined on the center of the disk plane where each CFS sample was positioned and anchored. Inside the cone below the disk, a calibrated imaging system detected the luminance of the light flux that was transmitted or redirected by the sample being measured. The detected luminance was divided by the incident illuminance on sample plane to compute the BTDF according to Equation (2.1). The rotation of the cone and the sample holder adjusted the relative incident direction of the source beam onto each sample being measured. The goniophotometer was capable of monitoring BTDF with a maximum of 145 incident directions of Tregenza zones and 1297 emergent directions with homogeneous intervals of azimuth angle and zenith angle (step size 5°).

4.3. Compression on medium-resolution BTDF data



Fig. 4.3. CCD imaging based Gonio-photometer

As a performance assessment, the BTDF of each sample was monitored at the maximum resolution of the goniophotometer and their photometric solids, showing the BTDF magnitude and direction, for one incident direction (zenith angle 36° , azimuth angle 0°) were presented in Figure 4.4. The pattern above the circular disk of coordinates illustrates the magnitude and direction of the emergent hemisphere of BTDF, while the arrow below the disk shows the direction of the incident ray. From the photometric solids, the diverse light transmitting behaviour of the five samples is illustrated in Figure 4.4, where panel a) and e) diffuse the incident light, while panel b) and d) maintain the sharpness and redirect the incident ray.

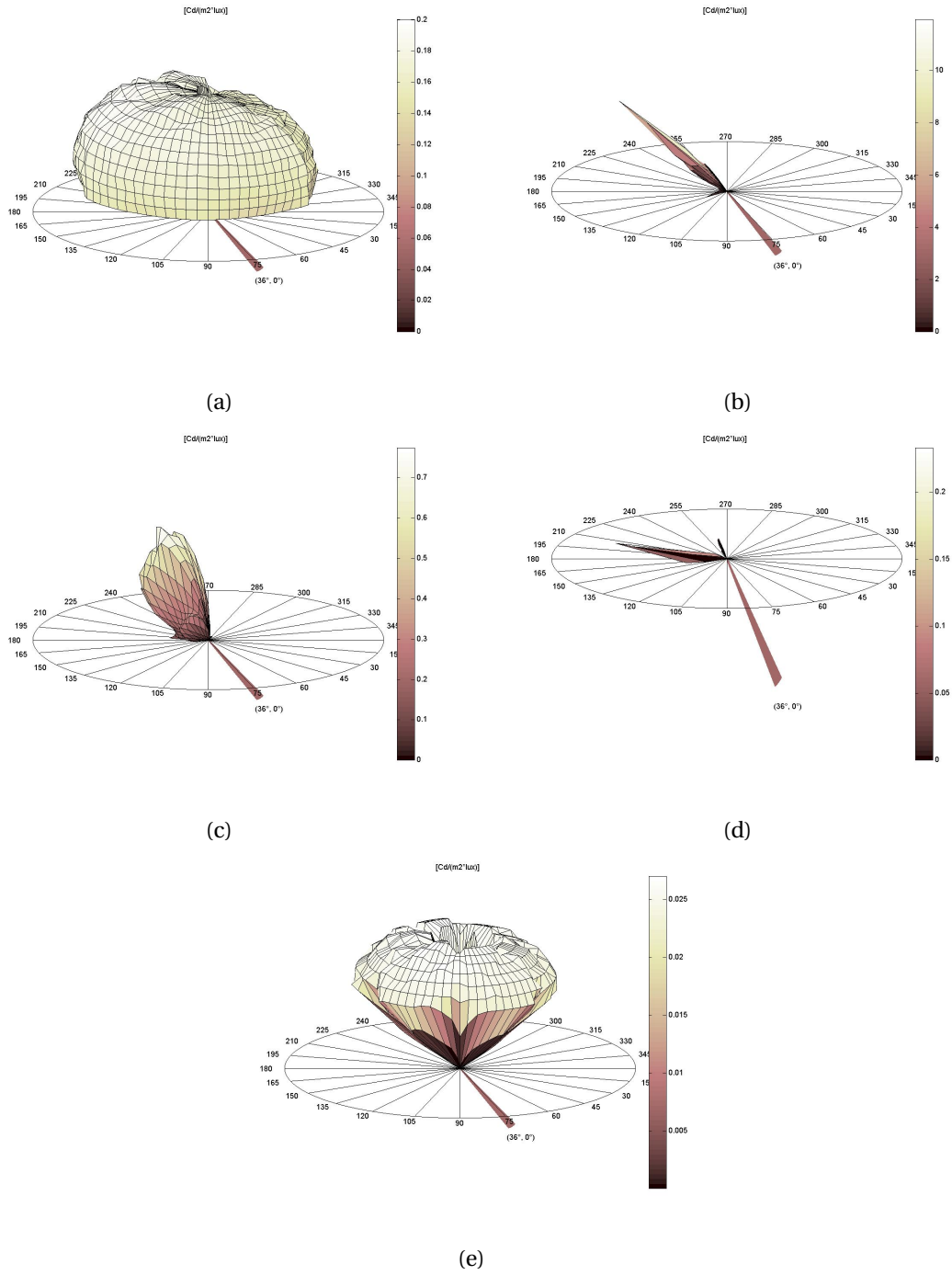


Fig. 4.4. Photometric solids of BTDF data of the five samples

4.3.2 Performance assessment

Since the BTDF resolution in the emergent hemisphere is uniform in its zenith and azimuth angle direction, the data in the two dimensions of the emergent hemisphere, as shown in

4.3. Compression on medium-resolution BTDF data

Equation (2.1), can be mapped to a 2-D matrix. Each group of BTDF matrix of samples went through the compression routine illustrated in Figure 4.1. Three commonly used wavelet bases in image compression were investigated and compared for their relative error, including DB10, Bior6.8, and CDF9.7. For the performance assessment, both the relative RMSE and transmittance error (TE) of the BTDF reconstructed from compression were calculated relative to the original data as reference. The intrinsic relative error of reconstructed BTDF illustrates the general quality (i.e., level of distortion) of compression; however, unnoticeable intrinsic error does not ensure superb performance in lighting applications. For instance, pronounced mismatch in certain critical emergent directions (e.g. direction of a sharp peak of BTDF, which occupies only a trivial portion of data), can contribute to substantial relative error in lighting simulation even if the overall RMSE of BTDF is negligible. Therefore, in this section, the simulation error in image rendering and daylighting metrics was additionally investigated for intra-scene lighting computations.

Generic error assessment

The dependence of different CFS types on the three wavelet bases was studied at an identical compression ratio. The quantization of BTDF data for each CFS sample and each wavelet basis was tuned to fix the compression ratio at 20 (i.e. compressed BTDF data occupies 1/20 the size of the original data). Then, the relative RMSE was computed for each CFS sample and the reconstructed BTDF and original BTDF over 145 incident directions and 1297 emergent directions were compared. Similarly, the relative TE was calculated by integrating the cosine weighted BTDF on the emergent hemisphere to compute the transmittance from each incident direction of the reconstructed and original BTDF, which was then used to compare the RMSE of sets of transmittance. The results of the RMSE of BTDF compression employing the three bases are shown in Figure 4.5, in which different bases are grouped for each CFS sample and denoted by shaded green error bars for each basis. According to the results, the DB10 basis exhibits the highest error of all the CFS samples, whereas the CDF9.7 shows the lowest error. Although the DB10 basis was inferior in terms of generic error, this orthonormal basis would be advantageous for the multi-resolution representation, of which the coefficients of the scaling functions are the best approximation (in ℓ_2) of BTDF at a reduced resolution. The overall pronounced error rate of the CFS3 (a prismatic panel) can be attributed to the sharpness of its BTDF, since the quantization of coefficients of wavelet basis commonly results in the loss of the high frequency part of the data, which smooths its peaks.

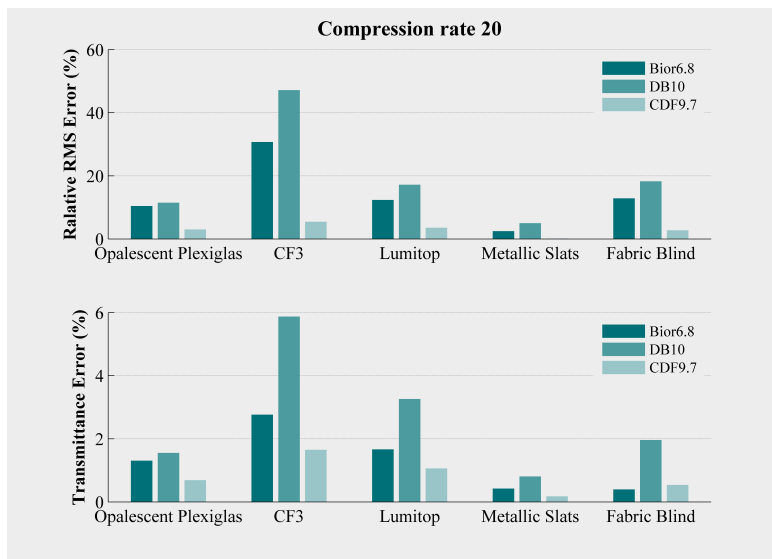


Fig. 4.5. RMSE and TE at compression ratio 20

Next, the performance of the two basis (Bior6.8 and CDF9.7) at various compression ratio was compared for one of the CFS samples (panel c). As shown in Figure 4.6, the quantization was tuned so that the two bases performed at identical compression ratios ranging from 20 to 220. Their RMSE and TE are compared in Figure 4.6, indicated by shaded lines with different marks. Based on the results, the CDF9.7 basis has a lower RMSE and TE over the full range of compression ratios, upto 220. According to the slopes of the lines, the gradient of error is depressed at higher compression rate, which can be explained by the significance of the coefficients of the scaling function. Since the coefficients of the scaling function are dense while those of the wavelet basis function are sparse, and the number of wavelet coefficients is 60 times more than the number of scaling coefficients, quantization increases the sparsity of wavelet coefficients at high compression ratio, while those of the scaling coefficients remain dense. Overall, the concentration of information on the scaling function coefficients makes the wavelet transform efficient at compressing BTDF at high compression ratio.

4.3. Compression on medium-resolution BTDF data

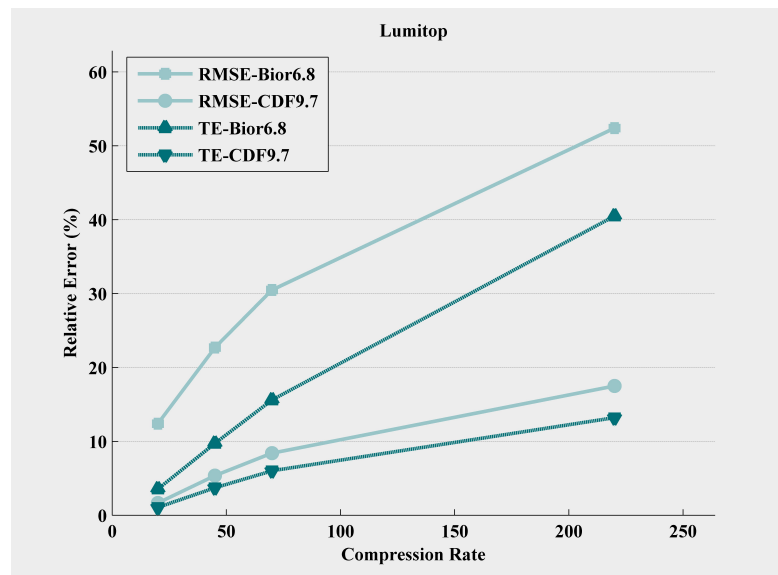


Fig. 4.6. RMSE and TE at various compression ratios of Lumitop

Daylighting simulation

A typical office with unilateral façades facing toward the south was modelled to evaluate the influence of BTDF compression on daylighting simulation. The modelled office was equipped with two pairs of desks and chairs, as illustrated in Figure 4.7. The unilateral window had two sections: a lower section for the outwards view of occupants, which contained a single layer of glazing, and an upper section for daylighting, where a sunlight re-directing glazing (panel c) was installed.

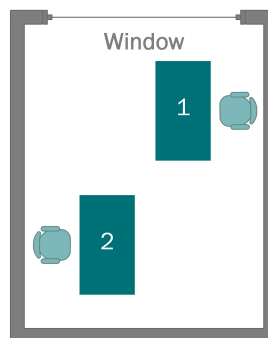


Fig. 4.7. Floor plan of an office room

The Radiance software [155] was used for the lighting simulation in the scene, which employed backward ray-tracing algorithms. The upper daylighting window section with installed CFS used the BTDF that was reconstructed from various compression ratio (up to 220) in the lighting simulation. The rendering of the office is shown in Figure 4.8, where the numbers at the bottom line denotes the corresponding compression ratio (CR) of BTDF. The rendering

of the scene was generated in the identical view direction and was compared to the one with original BTDF (uncompressed) in order to study the disparity. For the visualization, the rendered images were monochromatized and were subtracted from the one with the original BTDF (the left sub-figure of Figure 4.8). In Figure 4.8, the grey region signifies zero disparity while the magenta and green regions are associated with positive and negative error, respectively, of which the concentration of color is proportional to the magnitude of error. According to the figure array, the color region (error) starts to be pronounced on the shadow of the wall starting at compression ratio 70; at compression ratio 220, the color region even spreads onto the ceiling (noticeable error).

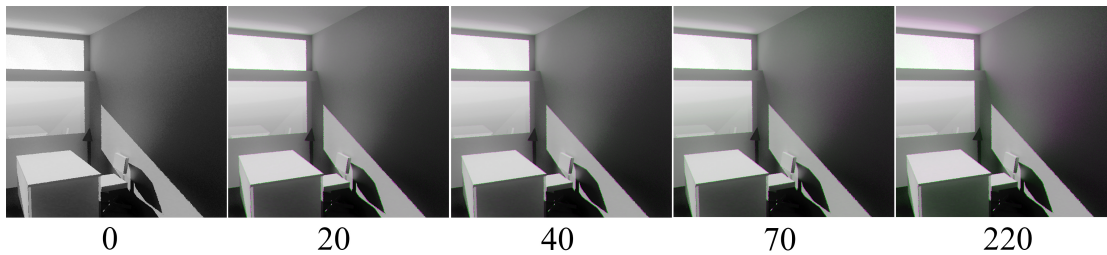


Fig. 4.8. Image rendering of daylighting in an office at various compression ratios

In addition to qualitative assessment, multiple daylighting metrics were computed to quantitatively evaluate the influence of BTDF compression on lighting simulation. In the field of user centric studies, the illuminance uniformity on the work-plane and glare risks are critical metrics for assessing the visual comfort of occupants. To evaluate daylighting simulation that is influenced by BTDF compression, the uniformity factor $g1$ [171], defined as the ratio of minimum illuminance over average illuminance, and the average horizontal illuminance E_{av} on the inner desk (desk 2 in Figure 4.7) were computed for the BTDF of a CFS (Lumitop, panel c in Figure 4.2) installed at the upper window for daylighting. The reason for investigating the inner desk (desk 2) instead of the desk close to the window (desk 1 in Figure 4.7) was due to the fact that the influence of CFS (from the upper window section) on the inner desk would be stronger than that on the one close to the window where the influence of the lower window section (with clear glazing) dominated. The uniformity factor $g1$ and average horizontal illuminance E_{av} were compared for the BTDF that was reconstructed from various compression ratio together with those of the original BTDF denoted as compression rate 0. Three critical days, including spring equinox, summer solstice and winter solstice (based on the Perez all-weather model [86] describing the sky luminance distribution), with clear skies were considered at mid-day time (12:00) to assess the two metrics $g1$ and E_{av} ; the results are illustrated in Figure 4.9. The uniformity factor $g1$ is relatively sensitive (fluctuation) to the compression despite a relative error maintains lower than 15%. This can be explained by the nature of wavelet transform based compression that smooths the BTDF and contributes to the alternation of peak magnitude of illuminance on the work-plane. In contrast, the average horizontal illuminance E_{av} on the desk is relatively immune to the compression.

4.3. Compression on medium-resolution BTDF data

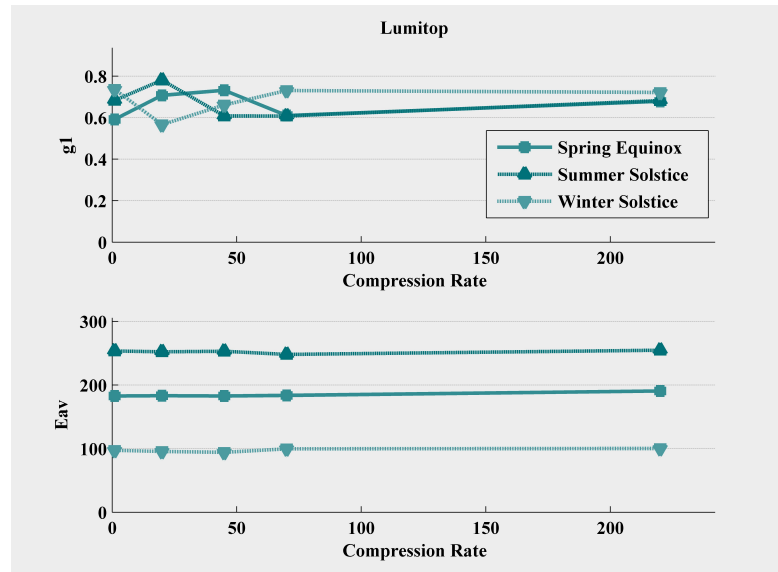


Fig. 4.9. Uniformity factor g_1 and average horizontal illuminance E_{av} on the desk

To assess the glare risk, a view point was defined at the position of the inner chair at a height of 1.2 m above the floor, oriented 45° to the façade. It emulates an occupant sitting on the chair with both the façade and shadow on the wall (the right-side wall in Figure 4.7) in field of view (FOV), as a worst case study on discomfort glare. The daylight glare probability (DGP) [172] was computed for the BTDF of the installed CFS (panel c in Figure 4.2) that compressed at various ratios, for a clear sky when the sun would be in FOV of the defined view direction through the upper daylighting window section if a clear glass were installed; the results were presented in Figure 4.10. According to the relative error, the compression of BTDF has negligible influence on the DGP for CR below 220.

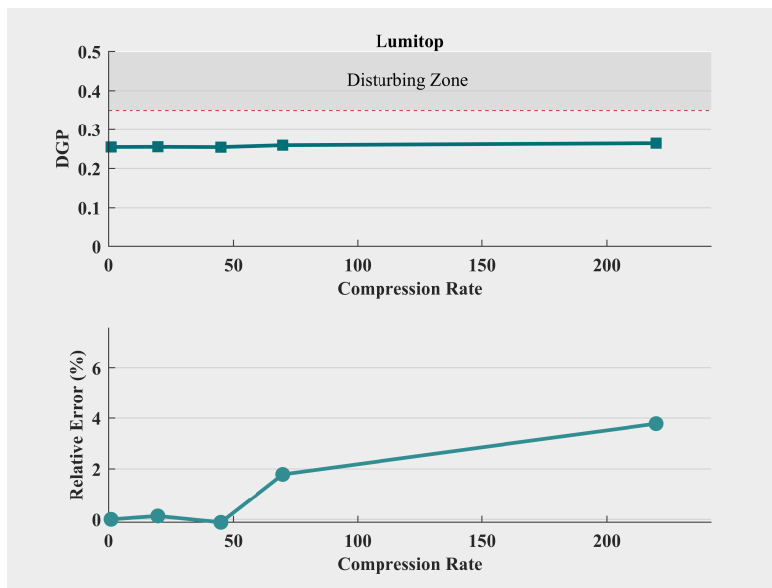


Fig. 4.10. Daylight glare probability (DGP) and its relative error

4.4 Compression on high-resolution BTDF data

High resolution BTDF data have an increasing significance in visual comfort study to achieve satisfying accuracy of daylighting simulation. Especially when the HDR imaging technique based sky luminance map is involved, pronounced lighting simulation error for a CFS can be due to the resolution mismatch between a low-resolution BTDF in discretized incident directions and a fine-resolution sky patch, with high contrast luminance of the clouds or the sun. In this section, the wavelet compression scheme is investigated for compressing a high resolution BTDF data of external Venetian blinds and evaluated on its performance in work-illuminance simulation with a monitored luminance distribution of the sky by the EPD [90].

The BTDF of an external Venetian blind (EVB), made of an 8 cm wide aluminium plate with a sinusoidal profile, was generated using the genBSDF program based on ray-tracing algorithms in RADIANCE. Although the tilt angle of the EVB slats is adjustable, this study investigated one of its tilt angles. The slats was fixed at 32° to the vertical plane. The BTDF was generated with 2305 incident and 2305 emergent directions, employing the subdivided Tregenza angular basis (Reihart MF:4). Figure 4.11 a) shows its BTDF matrix mapped onto an image with tone-mapping [173], where each row represents BTDF data of various incident directions and each column represents various emergent directions. With the black region denoting zero value, BTDF's non-trivial value is distributed along the diagonal and horizontal and vertical ripples. The compression scheme based on planar wavelet transform was applied on the BTDF of EVB with various quantization steps. The reconstructed BTDF matrix of compression ratio (CR) from 50 to 1000, after being tone-mapped into images, is illustrated in Figure 4.11 b) - f). The

4.4. Compression on high-resolution BTDF data

mismatch between the compressed and original BTDF is unnoticeable when CR is below 200. Above a CR of 200, the compressed BTDF exhibits a pronounced discrepancy, especially in the pattern of ripples. Its diagonal is blurred and part of the ripples disappear when CR reaches 1000. The generic relative RMSE of BTDF associated with various CR is listed in Table 4.1, which also corresponds to the discrepancy in Figure 4.11. Although its overall generic error is not substantial even at CR of 1000, lighting simulation can be influenced by the discrepancy of BTDF data in a limited number of directions.

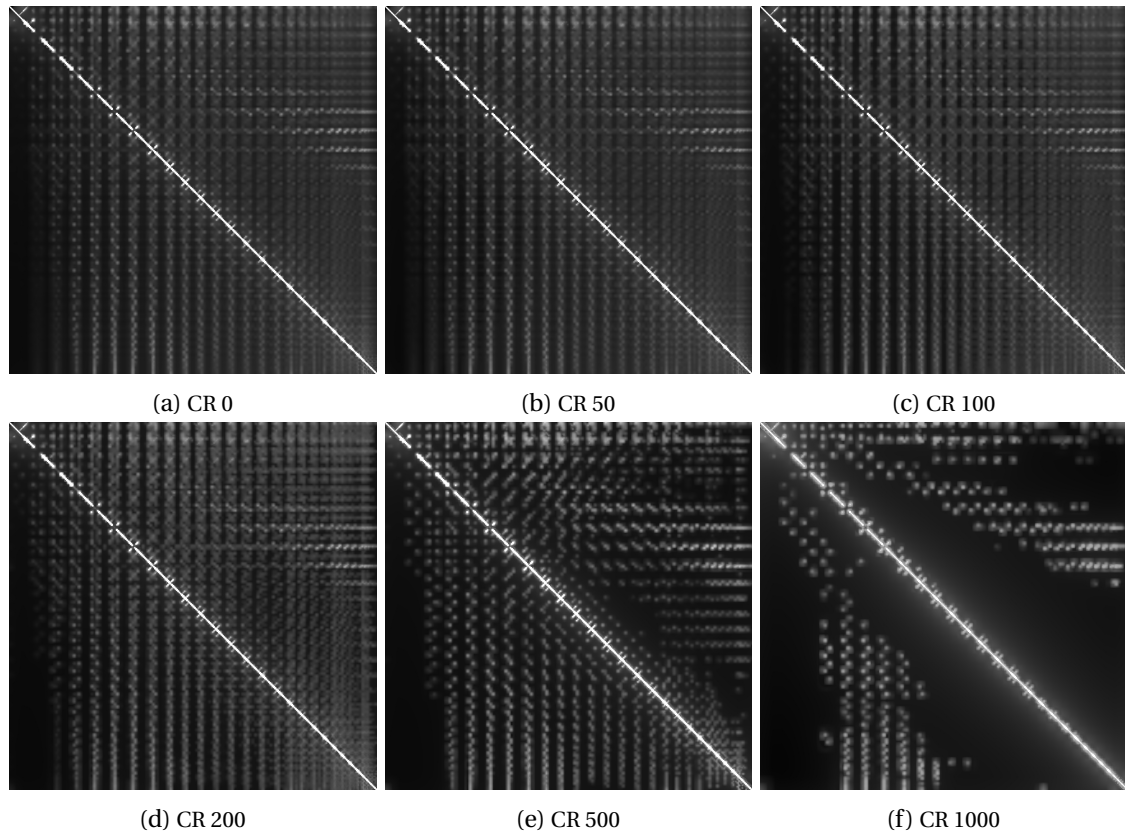


Fig. 4.11. Compressed BTDF data of EVB

Table 4.1 – Compression ratio of BTDF data and relative average error

CR	Generic RMSE of BTDF	Simulated WPI RMSE
50	0.3%	2.9%
100	0.9%	2.7%
200	1.7%	15.3%
500	3.3%	32.1%
1000	6.4%	36.9%

In order to evaluate the effect on lighting simulation, a daylighting test module, with interior dimension $6.4 \times 2.9 \times 2.6 \text{ m}^3$, was modelled to investigate the influence of employing compressed BTDF data in the simulation of work-plane illuminance (WPI) in Lausanne, Switzerland. The

module, as shown in Figure 4.12, was equipped with a south-facing unilateral façade that had a window-to-wall ratio of 62%. The EVB was installed, fully extended to cover the façade, and fixed at 32° tilt angle. An embedded photometric device [145, 3], based on HDR imaging technique, was positioned in front of the façade, which monitored the luminance distribution of the sky vault and landscape in front of the façade, including the sky background, clouds, the sun, and surrounding landscape objects; it mapped the luminance distribution into 3605 sky subdivisions as the daylighting source. Multiple virtual sensors at a height of 0.8 m in the module were defined to calculate the work-plane illuminance (WPI), employing the RADIANCE ray-tracer. In the WPI simulation, instead of defining the geometry of EVB, its corresponding BTDF data was employed to characterize the light transmittance properties of EVB.

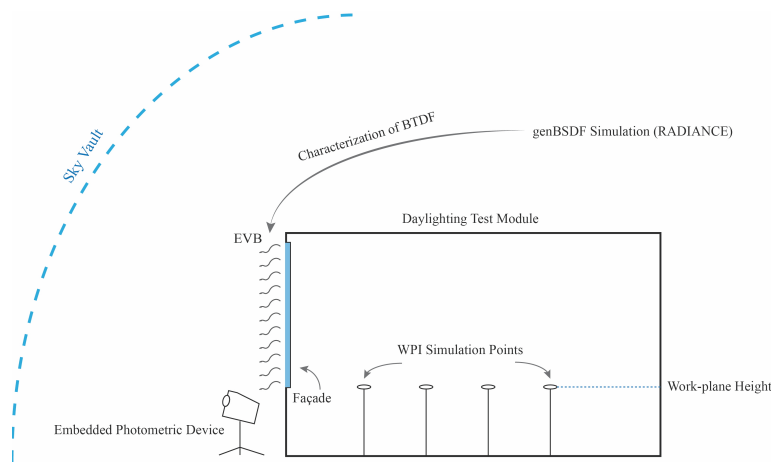


Fig. 4.12. Set-up in a daylighting test module

A day with a partly cloudy sky was selected for testing the performance of using high-resolution compressed BTDF data when the luminance distribution of the sky was peaky. The EPD monitored the luminance distribution of the sky every 15 min from morning to evening. The original BTDF of EVB was employed for the WPI calculation as reference; the compressed BTDF at various CRs was then used to calculate the WPI with an identical daylighting source (monitored sky luminance map), excluding artificial lighting. Since the lighting calculation method was identical, and only different BTDFs of the EVB were compared, alternation of WPI was the result from the discrepancy of compressed BTDF data. Figure 4.13 shows the results of simulated WPI from 9:00 to 17:00 employing BTDF data of the EVB with slats maintained at 32° tilt angle. The grey line denotes the WPI using the original BTDF as reference, while WPI simulated by employing compressed BTDF from CR 50 up to CR 1000 is marked by color lines respectively. Although the reference WPI fluctuates throughout the day due to the variable luminance distribution of the sky, the WPI influenced by using the compressed BTDF with CR 50 and 100 is marginal, the cyan and green lines of the figure almost overlapping with the reference grey line. For CR above 200, the mismatch starts to be noticeable, especially between 10:00 and 15:00, when the sky luminance distribution was peaky. The associated RMSE of WPI is calculated and presented in the third column of Table 4.1 accordingly.

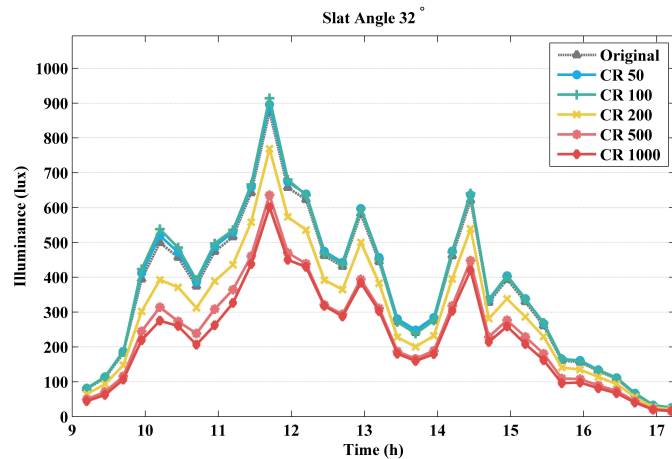


Fig. 4.13. Simulated work-plane illuminance at various compression ratio (CR)

4.5 Conclusion

Optimal integration of advanced daylighting technologies, including complex fenestration systems (CFSs), can contribute to reduce energy consumption for artificial lighting, cooling, and heating, and can improve the visual comfort of occupants in existing buildings. The BTDF that is used to characterize the light transmittance feature of a CFS is critical for generating high-quality daylighting simulations for building interior; however, establishing BTDFs for a CFS commonly involves generating bulky volumes of data, which is challenging both data storage and transmission, especially for compact platforms.

A compression scheme using 2-D wavelet transforms was presented in this chapter that considered image compression and was adapted to the condition of BTDF. In this scheme, quantization and Huffman coding were used to efficiently compress the data set to reduce its redundancy. The ability of this compression scheme was evaluated by applying it to compress medium-resolution BTDF data of five paradigmatic CFS samples; the original BTDF data was monitored by a gonio-photometer, and to compress a high-resolution BTDF of an EVB, simulated by genBSDF program in RADIANCE. Three wavelet bases were investigated for a quantitative evaluation of intrinsic error. Based on the results, the CDF9.7 basis performed with superb compression ratio and tolerable error rate both in RMSE and TE for CFS sets: at compression ratio 200, the RMSE was maintain below 20%. Although the orthonormal basis DB10 was inferior in compressing BTDF from the perspective of introduced generic error, it can be suited for the multi-resolution representation.

Compression of medium-resolution BTDF (145×1297) was evaluated in daylighting simulation of an office. Using the compressed BTDF as a representation of the CFS installed in the upper daylighting window section, both the scene rendering and multiple daylighting metrics

regarding visual comfort of occupants were investigated at various compression ratio of BTDF with the Perez all-weather model describing the sky luminance distribution. The error of rendering started to be noticeable from a compression ratio 70. For the daylighting metrics, it was found the uniformity factor g_1 was relatively sensitive to the compression, while, for WPI and DGP, the compression of BTDF based on wavelet transform maintained error below 5% for compression ratio up to 70. Furthermore, compression on a high-resolution BTDF (2305×2305) of an EVB fully extended and kept at 32° tilt angle was assessed in WPI simulation in a daylighting test module, with monitored sky luminance distribution of a partly cloudy sky using an EPD based on HDR imaging technique. Although generic (intrinsic) average RMSE of BTDF did not exceed 10% even at compression ratio 1000, the discrepancy in simulating WPI started to be noticeable when CR exceeded 200. According to the simulated WPI, compression ratio below 100 for BTDF maintained the fidelity of daylighting simulation.

In conclusion, the compression of BTDF data based on planar wavelet transform is able to achieve compression ratio of 100 with fidelity for the selected CFS with either medium-resolution or high resolution BTDF in visual comfort studies. The trade-off between compression ratio and error tolerance should be considered in specific applications. Although this chapter only investigates compressed BTDF data, the compression scheme is also potentially applicable on daylighting matrices of the 5-phase matrix algebraic approach [160] in lighting simulation, which can further reduce data storage load on compact computing platforms.

5 Automated Venetian blinds

5.1 Introduction

Optimal shading control can improve the visual comfort of occupants and energy savings on artificial lighting and on cooling loads. A highly integrated automated shading system is presented in this chapter with an improved actuator. Designed to regulate daylight ingress according to the varying sky conditions in decentralized applications, it optimizes visual comfort for occupants and maximizes their view outwards.

The shading control is based on real-time lighting simulation for a building interior based on monitored luminance distribution of the sky (and landscape), which employs an EPD. Its lighting simulation quality was cross validated in a daylighting test module, showing a 10% root-mean-square error (RMSE) in both work-plane illuminance (WPI) and daylight glare probability (DGP) calculation. Conducted under various sky conditions, the shading control demonstrated its capability in regulating daylight provision, mitigating excessive solar heat gain, tempering discomfort glare, and maximizing outside view for occupants with minimal delay during summer, autumn, and winter. The results showed that the WPI was maintained within the range of [500, 2000] lux during 96% of working time under clear skies and in between 79% and 88% of working time under partly cloudy skies. The expected associated mitigation of solar heat gain (SHG) was estimated to reach 47% during warm seasons. It was also demonstrated to successfully occlude veiling glare due to secondary reflection on specular surfaces from the surroundings. A survey study conducted with 34 subjects experiencing the shading system showed occupants' satisfaction on daylight provision, glare prevention, and quiet motion of adjustment. The chapter is based on the article "Automated 'eye-sight' Venetian blinds based on an embedded photometric device with real-time daylighting computing" submitted to the "Applied Energy" journal by Wu et al.

5.2 Design of automated EVB

The proposed design, named automated 'eye-sight' Venetian blinds, integrates an embedded photometric device (EPD) into the shading frame (or shell), with its imaging lens pointing outdoors, as illustrated in Figure 5.1 a). With the vision of exterior space, the EPD, comprising a microprocessor and an imaging system as illustrated in Section 3.2, is able to monitor the luminance distribution of the sky, including the sun, clouds, sky background, and landscape, and perform quasi real-time lighting simulation for building interior space. According to the dynamic sky conditions, the EPD calculates interior daylight provision and assesses glare risks based on a geometric model of building interior, to find a global optimal shading position. In fact, the EPD is not limited to be positioned in the shading frame (or shell) according to the figure but can also be fixed at other locations in the shading, including the bottom slat, as long as the imaging system of EPD points at the exterior space. When the optimal shading position is determined, a signal is sent to an actuator to adjust the shading position smoothly, as shown in Figure 5.1 b). Since the imaging system points outdoors rather than indoors, privacy issues can be avoided and the FOV of the sensor will not be obstructed by occupants' movements. The integrated set-up also alleviates installation complication and costs and maintains interior aesthetics, since no additional sensors or connection cable is necessary to be installed in a building interior. (Figure 5.1 excludes several detailed peripheral components, circuitry, and wiring connections in the shading device.)

5.2.1 Embedded photometric device (EPD)

Wu et al. [145] designed an embedded photometric device (EPD), mainly composed of a low-cost image sensor and a field programmable gate array (FPGA) processor. A comprehensive calibration was performed on its imaging system with regard to its spectral response, vignetting effect, signal response, and geometric transformation. After correction by optical filters, its spectral response is close to the CIE photopic luminosity function $V(\lambda)$ [174] (spectral correction error $f_1' = 8.89\%$), which can measure photopic quantities including luminance. Owing to its high-speed hardware and employed HDR imaging techniques, the EPD features a wide luminance detection range from 120 cd/m^2 to $3.78 \times 10^9 \text{ cd/m}^2$ (150 dB) within 1.3 seconds image acquisition time: the upper bound is above twice the maximum of the solar luminance $1.6 \times 10^9 \text{ cd/m}^2$ and the lower bound is low enough for the luminance of shadowing landscape during daytime. The EPD monitors luminance distribution of the exterior space, including that of the sun, clouds, sky background, and landscape, and map it into 1.2 million pixel groups. Together with the modelled scene and optical property of shading (described by BTDF data), the EPD is able to perform quasi real-time on-board lighting computing of building interior, which has been demonstrated with improved accuracy compared with using sky models [145, 3], saving efforts in landscape modelling. Details of the EPD has been illustrated in Chapter 3.

5.2.2 Shading actuator

Acoustic disturbance and rapid movement of shading can cause occupants' distraction and reduce their comfort. Therefore, a stepper motor coupled with a reduction gearbox, as shown in Figure 5.1 b), is introduced to mitigate noise level and to smooth motion of the shading. The stepper motor, driven by impulsed signal from the controller, can be configured to move as slowly as desired. The actuator is configured with two modes of speed: i) fast motion for vertical motion (1.7 cm/s, as fast as using a conventional shading actuator), or ii) slow motion for tilt angle adjustment ($0.8^\circ/\text{s}$, substantially slower than a conventional shading actuator). The noise levels for the two modes were measured to be approximately 10 dB and 20 dB lower respectively at 0.5 m distance than employing a conventional actuator with AC (alternating current) motor. The driving circuit of a stepper motor is also compatible with the EPD, since both are based on low voltage DC (direct current) power supply and digital signal communication, without introducing an additional ADC (analog-to-digital converter).

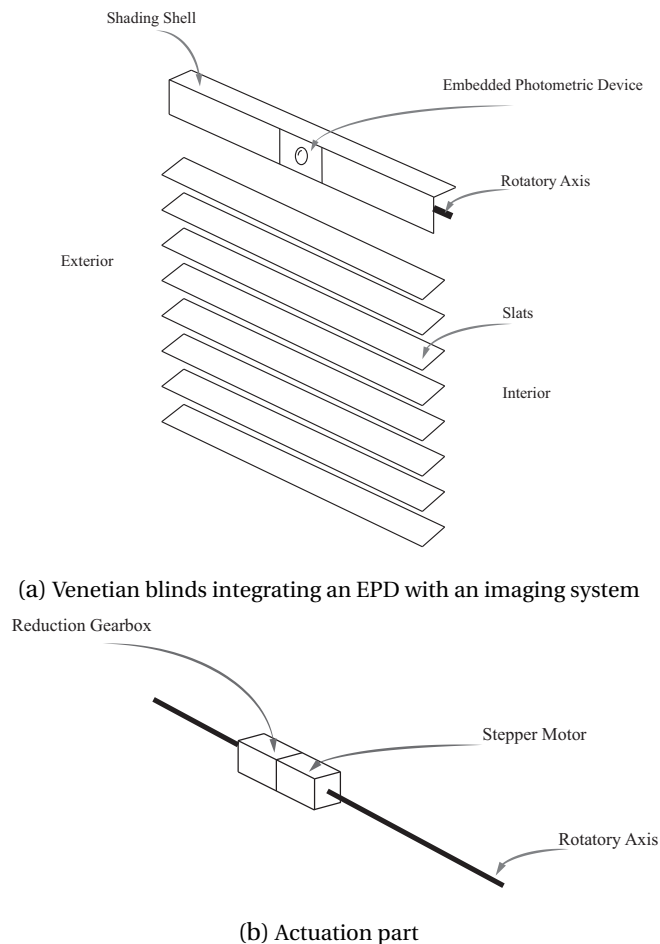


Fig. 5.1. Design of the automated 'Eye-sight' Venetian blinds

5.3 Methodology and control algorithms

5.3.1 Modelling and experimental set-up

A daylighting test module, with interior dimension $6.4 \times 2.9 \times 2.6 \text{ m}^3$ (located on the EPFL campus in Lausanne, Switzerland), was selected for testing and validation purpose. An external Venetian blind (EVB), each slat of which was a 8 cm wide aluminium plate with a sinusoid profile (52.4% and 81.5% reflectance on upper and lower side respectively, specularity 44%), was installed on its south facing double-glazed façade, showing a 0.62 window-to-wall ratio. In the prototyping phase, the EPD was positioned in front of the shading instead of in the frame (or shell) as designed for the sake of convenience for testing and re-configuration. This position shift is assumed to have unnoticeable influence on its control performance, as shown in Figure 5.2. Model of the test module was created in the EPD platform according to the physical features, for real-time lighting simulation in the interior space. To secure simulation accuracy, the dimension and position of each piece of furniture were measured by a laser range finder (Leica DISTO). Reflectance and specularity of each interior surface material were characterized by a chromameter (MINOLTA CR-220) and a gloss meter (MINOLTA GM-060) respectively.



Fig. 5.2. Daylighting test module with automated 'Eye-sight' EVB

As illustrated in Figure 5.3, the EPD was positioned with its lens axis in the orthogonal plane to the façade, pointing toward the sky vault and landscape. The bi-directional transmittance distribution function (BTDF) [106] of EVB was characterized (as explained in Section 5.3.2), describing its directional light transmission properties. Together with the modelled scene, the EPD calculated the work-plane illuminance (WPI) and daylight glare probability (DGP) in the module interior, at defined positions. In this chapter, the DGP is employed as a metric to evaluate glare risk for occupants. For cross validation purposes, lux-meter sensors (MINOLTA T10A, with $\pm 2\%$ accuracy) array was placed at 0.8 m height to measure horizontal illuminance in the module to compare with simulated values by the EPD and to assess shading performance.

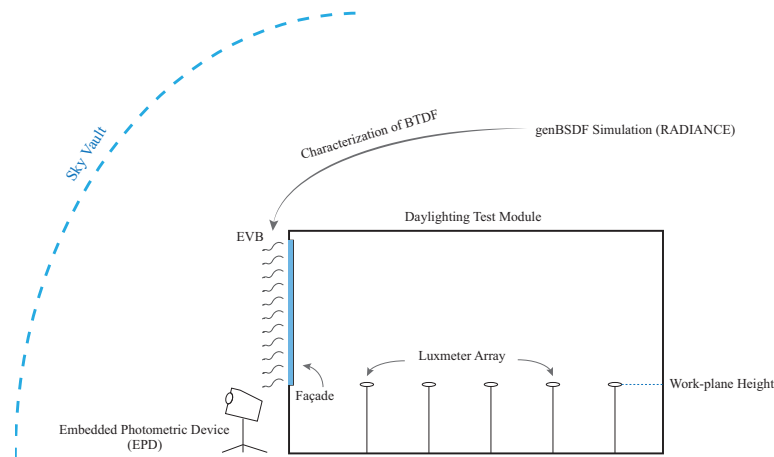


Fig. 5.3. Diagram of experimental set-up for shading control

5.3.2 BTDF data generation

BTDF is defined as the ratio of emergent radiance over incident irradiance on the incident plane [106], characterizing the directional light transmission properties of a complex fenestration system (CFS). It can be used to represent a CFS in daylighting simulation without knowing the geometry or material property of a CFS. In this chapter, BTDF is employed to represent the EVB in the lighting simulation algorithms (instead of using geometry of blinds) in order to speed-up the computation on the compact embedded platform for shading control. A group of BTDF was characterized for the EVB with its slats tuned at 15 different tilt angles with 5° interval increments from 0° (closed) to 72° (horizontal) inclined to the vertical plane, to be used in daylighting calculation. Each BTDF was generated using the genBSDF program, integrated in the RADIANCE software [155], based on ray-tracing algorithms. To account for veiling glare due to secondary reflection on specular surfaces from the outdoor surroundings and to improve lighting simulation accuracy, the genBSDF program was modified to deliver a high resolution BTDF data set: the Tregenza angular basis [156] subdivided by a factor of 16 (Reinhart MF:4 [175]), with 2305 incident and emergent directions, subtending an apex angle of 3° was used for that purpose. The HDR images of the generated BTDF matrix, after tone-mapping [173], are shown in Figure 5.4 and Figure 5.5 for a slat tilt angle of EVB at 72° and 32° respectively, compared with that of a low resolution BTDF based on the Klems angular basis [176] with 145 incident and emergent directions generated by using the original genBSDF program.

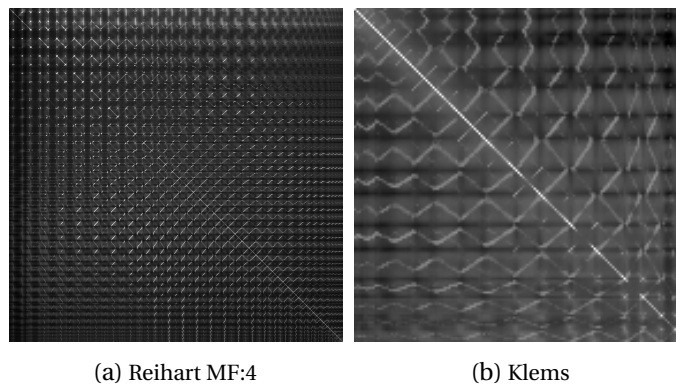


Fig. 5.4. Mapped BTDF of EVB at 72° slat tilt angle

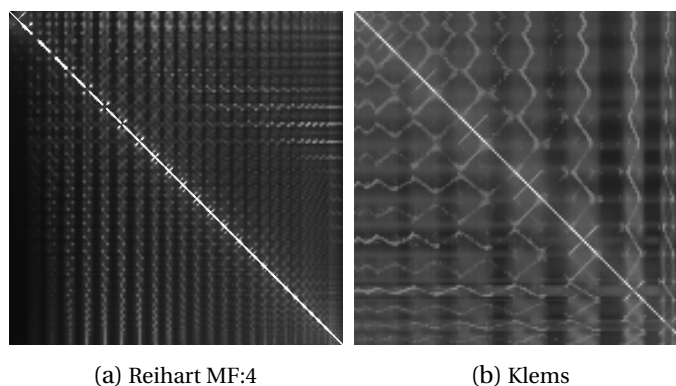


Fig. 5.5. Mapped BTDF of EVB at 32° slat tilt angle

5.3.3 Simulation method

Although the EPD is able to perform a quasi real-time daylighting simulation based on backward ray-tracing algorithms using on-board RADIANCE software, the time consumption of computing WPI and DGP is considerable for evaluating 15 different EVB tilt angles on a compact platform. Therefore, the five-phase matrix algebraic approach [177, 160] is employed for the EPD to evaluate daylight provision and glare risk in the building, making iterative computation time-efficient. The idea is to pre-compute matrices based on ray-tracing algorithms relating the monitored sky luminance distribution to the target WPI and HDR view image, as explained by Equation (5.1). In spite of the time consumption required to prepare these matrices, the iterative computation phase only involves matrix multiplication on the compact platform (EPD), which is substantially more time efficient compared with ray-tracing algorithms to achieve a comparable simulation quality. The EPD monitors the sky and landscape luminance distribution that the façade is facing and generates a luminance map with 1.2×10^6 units. Instead of using the original high resolution luminance map, it was pre-filtered and sub-sampled into 3602 sky patches for vector \mathbf{s} , each subtending a 2.4° apex angle. The multiplication of matrices \mathbf{VTDs} in Equation (5.1) is to compute the WPI according to the luminance map (\mathbf{s}). By changing the corresponding transmission matrix T (BTDF), WPI can be

calculated for the EVB with slats at various tilt angles. Since the sun orb only subtends 0.53° , a noticeable error of WPI simulation has been reported by Lee et al. [111] due to the mismatch between BTDF resolution using the Klems angular basis ($10 - 15^\circ$ apex angle) and the sun apex angle. Instead of directly raising the dimension of each matrix to address this issue, which potentially adds a considerable computation load, the direct sun component is extracted and its contribution to indoor daylighting is calculated independently by introducing the solar coefficient matrix (\mathbf{C}_{ds}) and direct solar vector (\mathbf{s}_{sun}), the product of which is the daylight contribution from the sun. The sun position is discretized into 5176 locations, each subtending 0.53° , and is approximated to the closest point with a maximal bias 1.5° . Since \mathbf{s}_{sun} is a sparse vector, the product of $\mathbf{C}_{ds}\mathbf{s}_{sun}$ involves trivial additional time consumption for the solar component calculation. The $\mathbf{V}_d\mathbf{T}\mathbf{D}_d\mathbf{s}_{ds}$ is used to exclude the redundant computation of solar contribution in daylighting from a diluted solar luminance element in \mathbf{s} and \mathbf{s}_{ds} . The same equation is employed to generate HDR view images to analyse glare risk; the only difference is that \mathbf{i}_{5ph} is a view image synthesized by arrays of sub-images \mathbf{V} and \mathbf{C}_{ds} . The dimension of each matrix is presented in Table 5.1.

$$\mathbf{i}_{5ph} = \mathbf{V}\mathbf{T}\mathbf{D}\mathbf{s} - \mathbf{V}_d\mathbf{T}\mathbf{D}_d\mathbf{s}_{ds} + \mathbf{C}_{ds}\mathbf{s}_{sun} \quad (5.1)$$

where:

- \mathbf{C}_{ds} is the solar coefficient matrix, relating the light contribution from the solar component at discretized locations to the WPI at corresponding positions.
- \mathbf{D} is the daylight matrix, relating sky luminance distribution to each incident direction on the front EVB plane.
- \mathbf{D}_d is the direct daylight matrix, similar to \mathbf{D} but excluding inter-reflections from the ground or surrounding objects.
- \mathbf{i}_{5ph} is the illuminance vector containing the WPI values at defined positions in the daylighting test module.
- \mathbf{s} is the sky vector, containing the luminance distribution of the subdivided sky monitored by EPD as input for lighting simulation.
- \mathbf{s}_{ds} is the direct sky vector, a sparse vector containing only the luminance of the diluted solar patch.
- \mathbf{s}_{sun} is the direct sun vector, a sparse vector containing only the luminance of the 0.53° solar patch with discretized locations.
- \mathbf{T} is the transmission matrix (BTDF), relating light flux transfer from incident directions on the EVB exterior plane to emergent directions on the interior side of the window façade.

- \mathbf{V} is the view matrix, relating the light contribution of each emergent direction from the window (interior) to the WPI at corresponding positions.
- \mathbf{V}_d is the direct view matrix, similar to \mathbf{V} but only relating the solar component (coarse resolution) excluding interreflection in the module.

Table 5.1 – Dimension of pre-computed matrices in the matrix algebraic approach

Matrix	Dimension (WPI)	Dimension (view image)
\mathbf{i}_{5ph}	238×1	500×500
\mathbf{V} (or \mathbf{V}_d)	238×2305	$500 \times 500 \times 2305$
\mathbf{T}	2305×2305	2305×2305
\mathbf{D} (or \mathbf{D}_d)	2305×3602	2305×3602
\mathbf{s} (or \mathbf{s}_{ds})	3602×1	3602×1
\mathbf{C}_{ds}	238×5176	$500 \times 500 \times 5176$
\mathbf{s}_{sun}	5176×1	5176×1

5.3.4 Control algorithm

The EVB control employs an optimization process based on an objective function to maximize the EVB opening (α) for occupants' view outwards, with constraints on WPI and DGP satisfying visual comfort, as explained in Equation (5.2). The work-plane is defined as a $1.6 \times 1.3 \text{ m}^2$ horizontal rectangle area at 0.8 m height representing a virtual desk in the module, with its center at 1.5 m distance to the façade. The WPI calculation involves averaging illuminance values of 238 points distributed evenly with 10 cm spacing on the work-plane, as highlighted in Figure 5.6. The WPI is constrained to be larger than 500 lux, satisfying minimum daylight provision (EN 12464-1 [49]), but to be lower than 2000 lux, preventing excessive solar heat gain. Two view positions are investigated at both sides of the work-plane at 1.2 m height, representing two seated occupants. Their views are oriented at 45° and 135° to the façade respectively, with 10° elevation upward: this can be considered as one of the worst cases regarding discomfort glare, since both the façade, as a major glare source, and sunlit area on the wall are within occupants' FOV. The DGP, employed as the glare risk metric for daylit space, can be computed by the EPD using the 'evalglare' program in the RADIANCE software, once view images are generated. In Equation (5.2), the larger DGP value of the left (DGP_l) and right (DGP_r) view perspectives are constrained to be below 0.35, within the imperceptible glare range [53] for visual comfort from both view directions.

Maximize:

$$\alpha \tag{5.2a}$$

Subject to:

$$500 \text{ lux} < \text{WPI} < 2000 \text{ lux} \quad (5.2b)$$

$$\sup\{\text{DGP}_l, \text{DGP}_r\} < 0.35 \quad (5.2c)$$

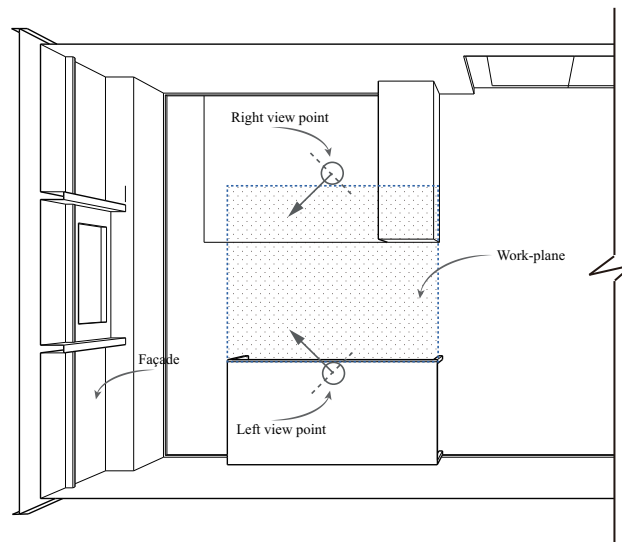


Fig. 5.6. Floor-plan showing defined work-plane position and view directions

The EPD work flow is illustrated in Figure 5.7 with the time consumption of the corresponding process annotated next to each block, as performed by the EPD. The EPD firstly monitors the luminance distribution of the sky vault and ground, including the sun orb, clouds, sky background, and landscape, based on HDR imaging techniques. Then the generated luminance map is sub-sampled into the sky vector \mathbf{s} in Equation (5.1) with 3602 luminance patches. With the sky vector \mathbf{s} as input, the WPI is calculated on board for 15 EVB positions, including the EVB fully retracted position, fully extended with horizontal slats (tilt angle 72°), slats inclined at 67° , 62° , ... 12° , and EVB fully closed (tilt angle 0°), ordered in descending openings. In this chapter, the intermediate position between fully retracted and extended positions is not considered, since frequent vertical motion of EVB is distracting for occupants and tilt angle adjustment is more efficient in tuning daylight injection and preventing glare than vertical position adjustment [2]. Moreover, a low priority is attributed to the vertical movement of slats from extended position to fully retracted position to reduce disturbance. Priority is given to tilt angle adjustments, except the case that the retracted position is the only solution satisfying Equation (5.2). According to the simulated WPI results, the EPD selects the corresponding shading positions satisfying the constraint of [500, 2000] lux for further evaluation. If no position satisfies, the daylight provision is too low in this case and full retraction of EVB is the optimal position, since it is impossible for the WPI to exceed 2000 lux at EVB's fully closed position in this module with an unilateral façade. The set of EVB positions satisfying the WPI constraint is further assessed with HDR view images generated from the left and right view

Chapter 5. Automated Venetian blinds

perspectives. Based on the view images, the DGP is calculated by the EPD, and the shading is optimized for the largest opening with corresponding DGP below the 0.35 limit, for occupants' maximal possible view outwards. Finally, the EPD as a controller sends a signal to the actuator to adjust shading to the optimized position. The whole process of each evaluation takes 6-10 min depending on the number of assessed shading positions within the daylighting constraint, subject to sky conditions. The interval of each iterative evaluation is set to be 15 min, leaving an over 50% time margin.

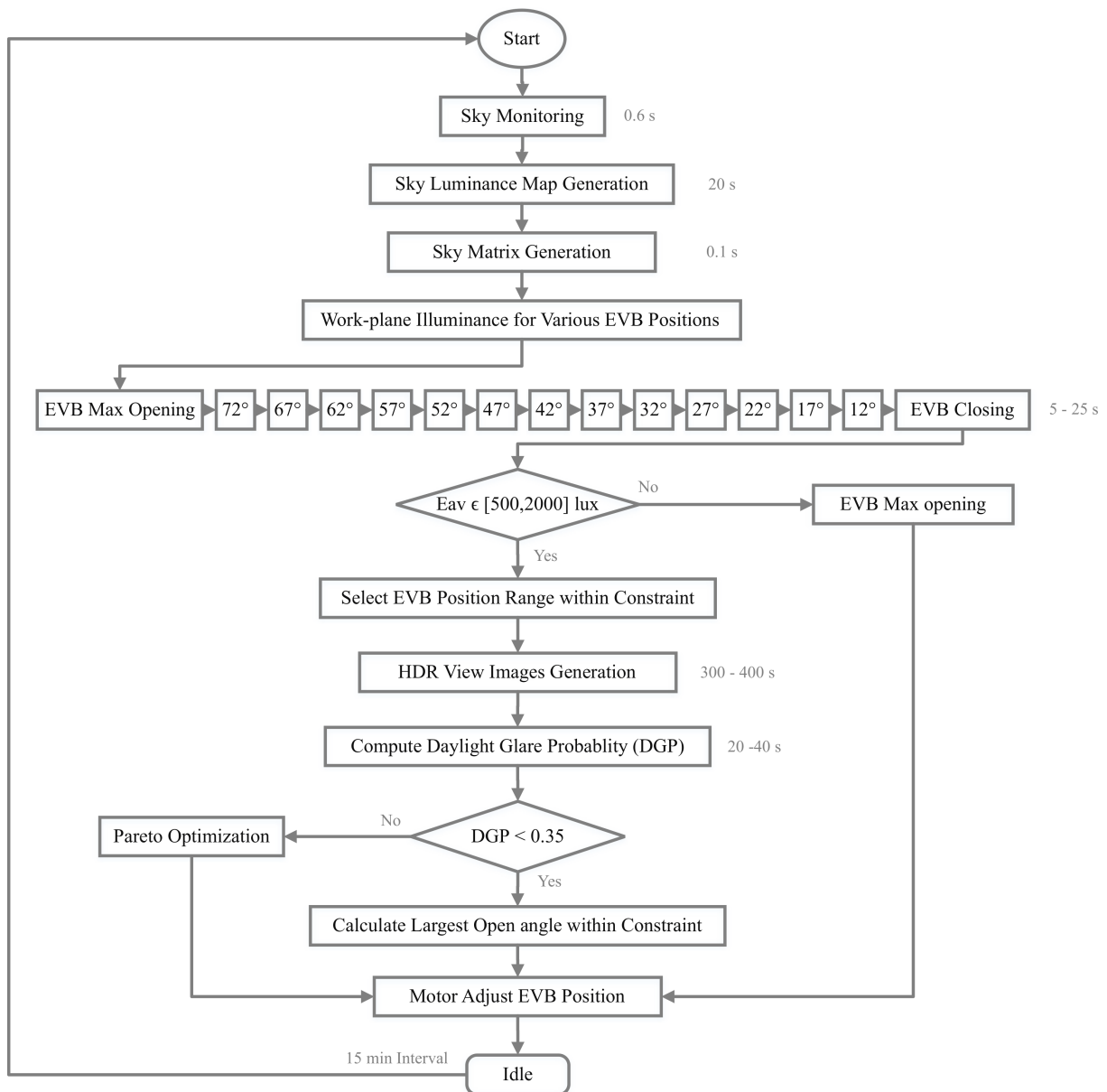


Fig. 5.7. Flow chart of control process on EPD

5.4 Empirical validation

The accuracy of daylighting simulation influences the performance of shading control, since optimization of the shading position depends on the simulated WPI and DGP results. Although Wu et al. have demonstrated the real-time lighting simulation capability of the EPD in several studies [145, 178, 3, 179, 180], additional experiments were conducted in the daylighting test module to validate the simulation accuracy for work-plane illuminance and DGP, employing the method introduced in Section 5.3.3. The 'in-situ' EVB control experiments were performed over multiple weeks under various sky conditions covering three seasons: summer, autumn and winter. Furthermore, the automated 'Eye-sight' Venetian blind was demonstrated to succeed in preventing veiling glare from outdoor surroundings.

5.4.1 Cross validation

In order to evaluate the simulation capability performed by EPD, the real-time simulation of horizontal illuminance, view image rendering, and glare risk were cross validated by means of reference apparatuses. The slats of the shading were fully extended and were fixed at 72° tilt angle (horizontal slats). Inside the module, 5 lux-meter sensors were positioned at 1 m, 2 m, 3 m, 4 m, and 5 m distance to the façade at 0.8 m height. The horizontal illuminance values were compared with the simulated ones at identical positions in the modelled scene, as illustrated in Figure 5.3. A calibrated HDR camera (Icycam, $\pm 13\%$ accuracy in luminance detection, compared to the luminance meter Minolta LS-110) [96], connected to a computer, was placed at 1.5 m distance to the façade at 1.2 m height, facing the window at 45°, as the left view point defined in Figure 5.6, to capture view images and then generate reference DGP values. The camera with its 180° fish-eye lens is able to monitor luminance distribution inside the module with a 130 dB dynamic range in detection. The set-up for cross validation is shown in Figure 5.8.



Fig. 5.8. Cross validation set-up with a reference camera

Chapter 5. Automated Venetian blinds

The experiment was conducted from morning to evening on June 23rd, 2018 on the EPFL campus in Lausanne, Switzerland, a day with clear sky conditions (occasionally with thin clouds). The EPD, placed outside the module, performed lighting calculations every 15 min for horizontal illuminance and DGP based on simulated view images. Both the lux-meter sensors and the reference camera inside the module were synchronized with the EPD, to record reference illuminance values and capture view luminance images simultaneously. Figure 5.9 shows one of the simulated view images performed by the EPD from the left perspective based on monitored sky luminance map, with the glare source labelled in Figure 5.9 b) (different color represents different group of glare source). Figure 5.10 presents the HDR image captured at the same time by using the reference camera. A sound correspondence is achieved and illustrated comparing the two sets of images with regard to light and shadow. Although the view image simulated by the EPD shows a mosaic pattern on its landscape through the window and details including the texture of shading slats are lost due to the discretization of the sky vector, the tree's profile (in front of the module) is still discernible from both images.

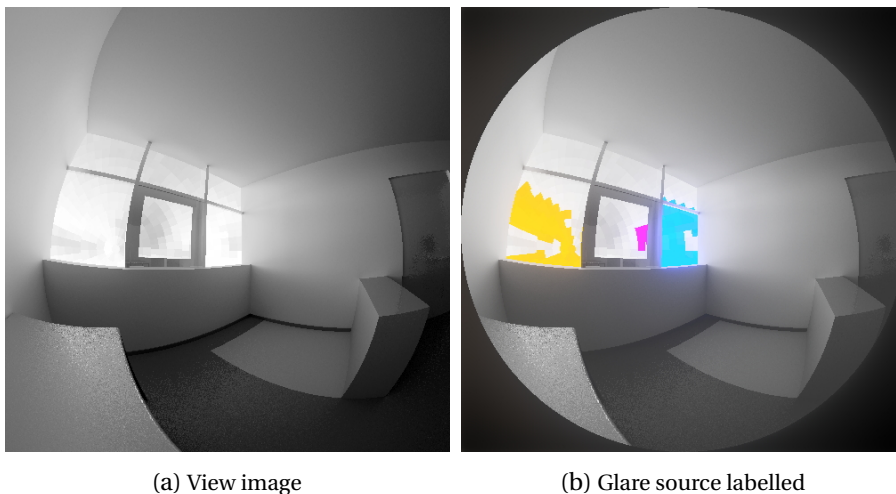


Fig. 5.9. Simulated HDR view images by the EPD

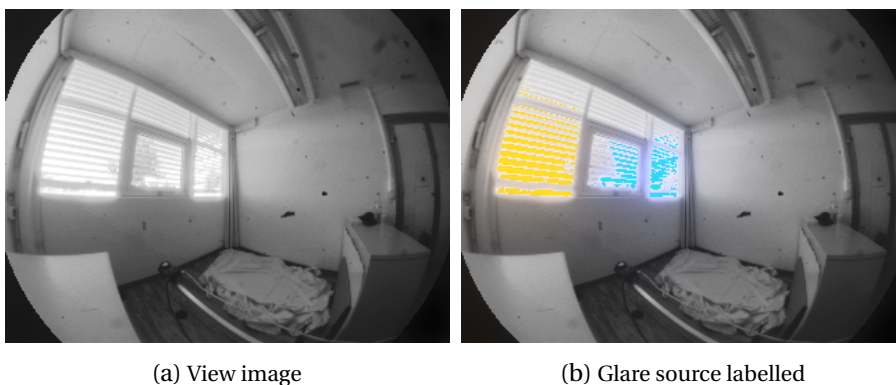
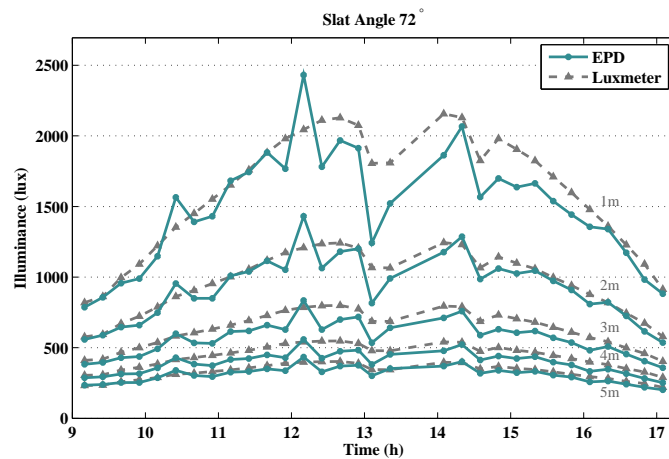


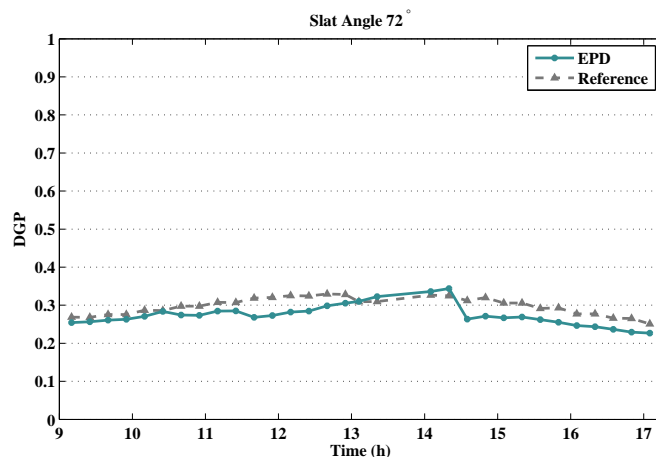
Fig. 5.10. Captured HDR view images by the reference camera

The simulated horizontal illuminance calculated by the EPD is illustrated in Figure 5.11 a)

denoted by green lines, compared with reference values measured by lux-meter sensors (grey lines). The stacked lines show the illuminance at locations from 1 m to 5 m distance to the façade respectively. The average root mean square error (RMSE) of horizontal illuminance for the 5 positions is 8.9%, 6.3%, 10.9%, 10.8%, and 7.1% respectively. Figure 5.11 b) presents the simulated DGP (green line) on EPD compared with reference values recorded by the IcyCam: its relative RMSE is 9.0%.



(a) Horizontal illuminance



(b) Daylight glare probability (DGP)

Fig. 5.11. Simulated variables by the EPD compared with reference values

5.4.2 EVB control

Although shading control is completely dependent on the simulation results of the EPD, in order to assess the shading control performance, five lux-meter sensors were re-arranged and positioned at the corners and center of the virtual rectangle work-plane, defined in Section 5.3.4, to monitor horizontal illuminance, the average of which was regarded as WPI. The sensors were connected to a data logger to simultaneously record illuminance values every

Chapter 5. Automated Venetian blinds

30 s. The EPD, positioned outside, performed shading control every 15 min from morning to evening, based on the monitored sky luminance distribution and real-time daylighting computation, according to the methods presented in Section 5.3.4. Experiments were conducted to evaluate daylight control, with no electric lighting indoors, during multiple weeks covering three seasons, including summer (Jul. 3rd ~ 24th), autumn (Sept. 2nd ~ 8th), and winter (Jan. 4th ~ 19th), and under various sky conditions, including clear, partly cloudy, and overcast skies.

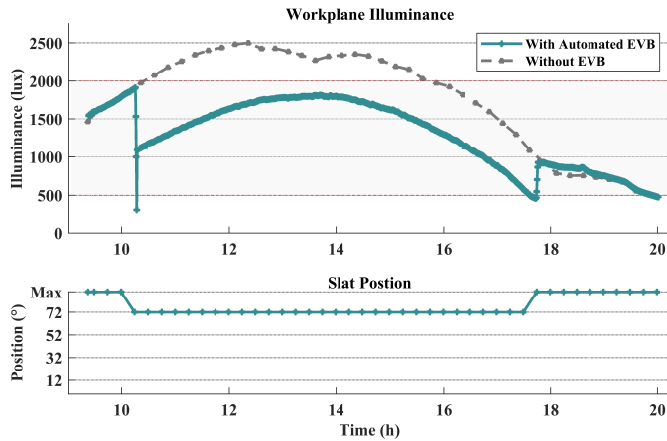


Fig. 5.12. Set-up of lux-meter sensors to monitor WPI as reference

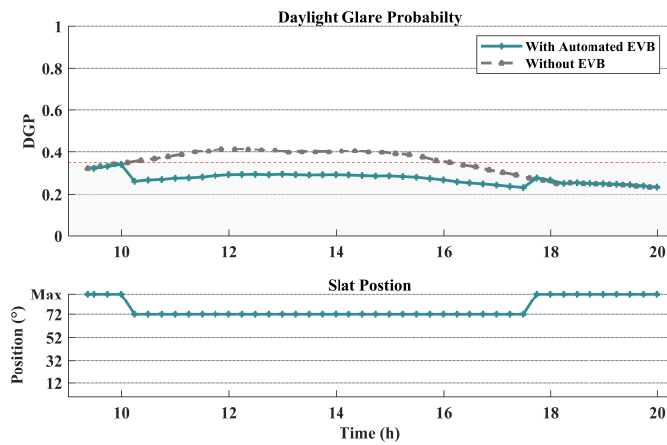
Figure 5.13 shows the WPI and DGP results on Jul. 11th for a clear sky in summer. The WPI monitored by lux-meter sensors in the module is denoted by green curves in the upper section of Figure 5.13 a), showing the regulated daylight provision achieved by the automated EVB. To contrast its performance, the WPI in the same module with a clear double glazing (without shading) was simulated by the EPD represented by the grey curve, as a reference case. It can be noticed that the density of data points on the green curve is higher than that on the grey curve, since the lux-meter recorded illuminance every 30 s, while the EPD performed simulations at 15 min intervals. The lower section of Figure 5.13 a) and b) shows the real-time position of the automated EVB, with 'Max' denoting the fully retracted position and numerical values representing the tilt angle of slats at the fully extended position, arranged in an order of descending openings. According to Figure 5.13 a), the EPD starts shading control in the morning, with the EVB initially at fully retracted position, contributing to the overlap of the monitored (green) and simulated (grey) WPI. The overlap section of the two curves also confirms the daylighting simulation quality of EPD without noticeable mismatch. Before WPI exceeded the upper bound of 2000 lux at 10:10, the shading slats were lowered and turned to the horizontal position (72° tilt angle). The movement of the shading caused the falling and rising edge of WPI, due to the EVB mechanical design the slats reaching the vertical position (0° tilt angle) first before turning to the horizontal position from the retracted state. The slats were maintained at 72° tilt angle as optimized by the EPD controller, when the external daylight condition varied smoothly under a clear sky. When the WPI reached the lower bound of 500

lux at 17:40 in the evening, the EPD lifted the slats into the shading shell (retracted position) to allow sufficient daylight admission.

The upper section of Figure 5.13 b) shows the simulated DGP values achieved at the EPD optimized shading position (green curve) optimized by EPD, compared with the simulated DGP without shading protection. The data point densities of the two curves are identical, since they are both simulated by the EPD at 15 min intervals. When the sun caused glare to the right view perspective at 10:10, the DGP exceeding 0.35 triggered the movement of EVB slats to descend to horizontal position. Although DGP exceeded comfort level without EVB protection between 10:10 and 16:20, the optimized horizontal position of slats kept the DGP from both view directions from left and right within the visual comfort range. In order to dampen the disturbing vertical movement of shading as mentioned in Section 5.3.4, the slats were not lifted to 'Max' at 16:20, even though it satisfied the constraint of visual comfort (highlighted region in Figure 5.13). The slats only returned to the fully retracted position when it was the only solution at 17:40.



(a) Workplane illuminance (WPI)

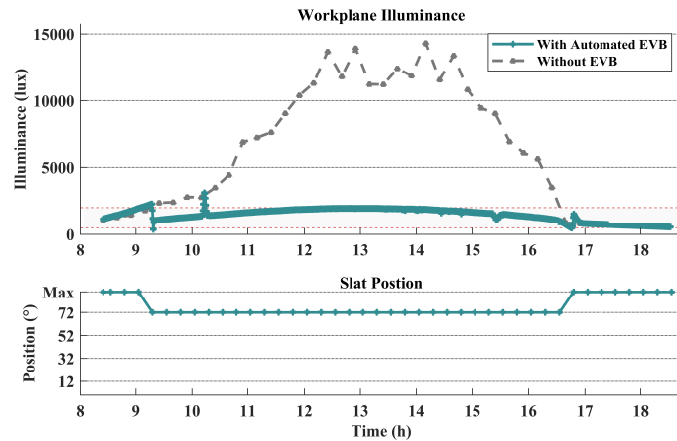


(b) Daylight glare probability (DGP)

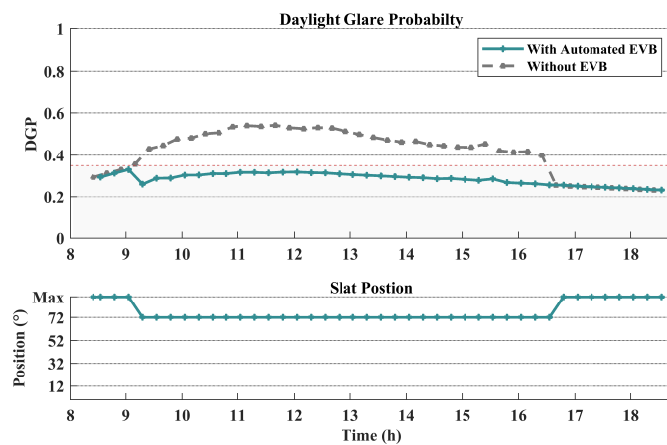
Fig. 5.13. WPI and DGP with/without automated EVB (summer, clear sky)

In autumn, when the solar elevation angle is lower than that in summer, direct sunlight penetrates into deeper regions of the building interior, potentially raising the glare risk for occupants. Figure 5.14 presents the WPI and DGP achieved on Sept. 8th under a clear sky. Comparing Figure 5.14 and Figure 5.13, both the WPI and DGP are larger without shading protection, since the lower elevation angle increases the fraction of work-plane exposed to direct sunlight. In the morning at 9:20 as shown in Figure 5.14 a), the exceeding WPI at the upper bound of 2000 lux triggered the EVB to stretch down, with its slats optimized at the horizontal position (72° tilt angle). The WPI regulated by the automated EVB stayed within the constraint throughout the day, except for a WPI spike at 10:10 sensed by the right front lux-meter exposed to direct sun rays through gaps between slats. When the external daylight source was dim enough to reduce the WPI to the lower bound of 500 lux at 16:40, the EVB slats were lifted up to allow sufficient daylight provision, resulting in the increased WPI. Although the DGP without EVB protection entered the intolerable glare range (above 0.45) [53], the DGP

regulated by the automated EVB remained below 0.35 within the imperceptible range. It was found that, under clear skies, two EVB movements are enough to provide occupants visual comfort regarding WPI and DGP and to maximize their view outwards in summer and autumn, as suggested by the daylighting standard EN 17037 [50]. The automated EVB controlled by the EPD was demonstrated to extend and retract shading slats timely, without introducing redundant movement or oscillation for adjustment which can disturb occupants.



(a) Workplane illuminance (WPI)

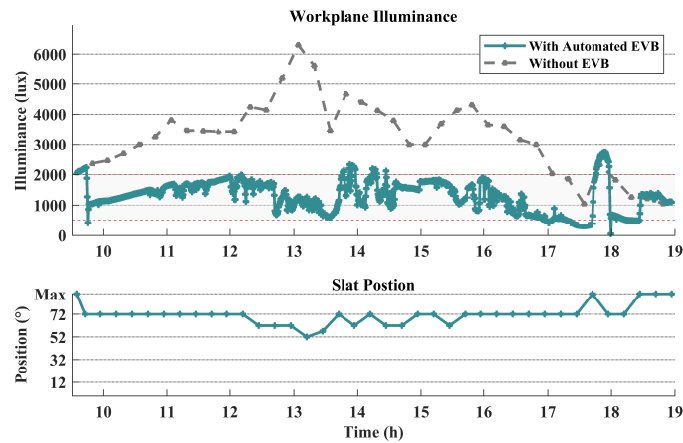


(b) Daylight glare probability (DGP)

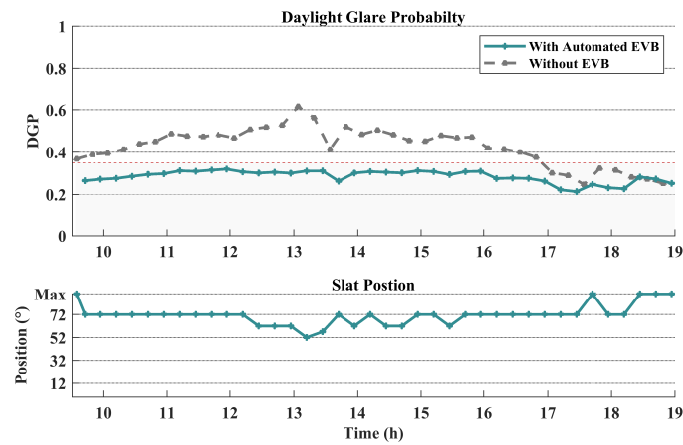
Fig. 5.14. WPI and DGP with/without automated EVB (autumn, clear sky)

Under a partly cloudy sky, shading control is challenging and complicated. The sky can repetitively alternate between bright and dim conditions, and the rapidly moving clouds can occlude the sun and then move away frequently. Furthermore, moving clouds in various shapes and dimensions make the sky luminance distribution peaky. The resulting sky luminance also changes drastically in strength and direction. The shading position has to be adjusted accordingly, tuning daylight injection through the window according the rhythm of dynamic sky conditions.

Figure 5.15 shows the performance of the automated EVB in WPI and DGP during one of the partly cloudy days, on Jul. 14th. In the morning, when the controller (EPD) started to operate, both the WPI and DGP exceeded constraints, and the shading slats were adjusted by the EPD to stretch down and turn to the horizontal position (72° tilt angle), thereby bringing WPI and DPG into the visual comfort range. When the WPI reached the upper bound of 2000 lux at 12:10, the EVB slats were turned to the 62° tilt angle, to avoid increasing the WPI. Due to a rising sky brightness at 13:10, the increased DGP due to inter-reflection between slats was suppressed below 0.35 by further closing the slats to the 52° tilt angle, which simultaneously reduced WPI. After the daylight external source became moderate at 13:25, the EVB was adjusted to the 57° and then 72° tilt angle, which increased the opening to admit sufficient daylight. Due to a drastic change of sky conditions after 13:40, the EVB adjusted its tilt angle multiple times to maintain WPI and DGP within constraints. Owing to the improved actuator with stepper motor, the slow rotatory motion of EVB slats diminished disturbance to occupants, despite an increased number of movements (14 times) under a partly cloudy sky. Although the WPI fluctuated throughout the day, both the WPI and DGP were maintained within the constraints by the automated EVB, achieving visual comfort and maximizing the outside view for occupants. Since the lux-meters recorded WPI every 30 s, while the EPD operated at 15 min intervals, the controller could ignore certain instantaneous spikes of WPI due to the mismatch of operating frequency, which can be improved by employing advanced computation hardware or simplified calculation algorithm.



(a) Workplane illuminance (WPI)



(b) Daylight glare probability (DGP)

Fig. 5.15. WPI and DGP with/without automated EVB (summer, partly cloudy sky)

Figure 5.16 presents the time fraction of WPI satisfying the target illuminance constraint of [500, 2000] lux achieved by the automated Venetian blind (color bars) for each date while discomfort glare is tempered, in comparison with that achieved without shading protection (dashed bars). Different bar colors are assigned to denote various sky conditions during the day, including clear sky (blue), hybrid sky between clear and partly cloudy condition (cyan), hybrid sky between partly cloudy and overcast condition (light green), and overcast sky (grey), during summer, autumn (shaded grey background), and winter (shaded darker grey background). According to the figure, the automated blind achieves optimal performance in regulating daylight provision under clear skies, providing indoor lighting conditions within the constraint more than 90% of time (96% on average) to provide sufficient daylight provision for reading and writing and to prevent excessive SHG. The performance under hybrid skies between clear and partly cloudy conditions follows closely (in constraint for 88% of the time on average), despite rapidly changing daylighting conditions due to the motion of clouds. Since

Chapter 5. Automated Venetian blinds

thick clouds impair daylight availability indoor, the ratio (79% on average) under hybrid skies between partly cloudy and overcast condition is relatively low when dense clouds, occluding the sun, contribute to insufficient daylighting. The overall lower ratio in winter is a result of low daylight availability due to shorter daytime. For overcast skies, the ratio is essentially the same as that without EVB protection, since shading remains in the retracted position to allow a maximal daylight transmission. The minor mismatch is caused by the sampling frequency differences between the EPD (15 min) and the lux-meter (0.5 min). Figure 5.17 shows the ratio of mitigated WPI with integration of time achieved by the shading automation for each date in summer. Assuming the solar heat gain (SHG) is proportional to the horizontal illuminance [181], the projected mitigation in SHG is estimated to reach 47% on average in a warm season.

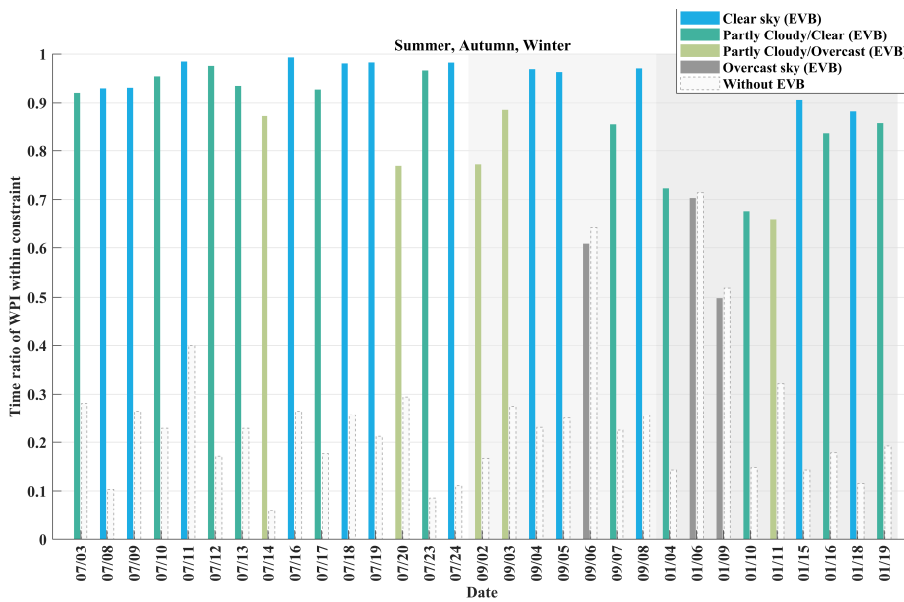


Fig. 5.16. Time fraction of WPI satisfying the constraint [500, 2000] lux achieved by automated EVB compared with no shading protection under various sky conditions

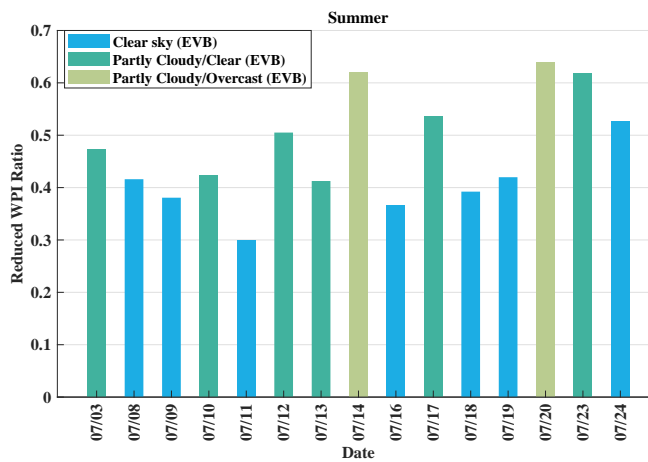


Fig. 5.17. Reduced WPI ratio during summer time

5.4.3 Veiling glare

Since the automated 'Eye-sight' Venetian blind is designed to analyse information from the exterior space, veiling glare due to specular reflections from the environment can be sensed by its integrated imaging system and processed by the EPD in daylighting calculation: the shading position can then be optimized to exclude veiling glare from the exterior. Its functionality in preventing veiling glare was demonstrated by physically inserting a curved mirror in front of the module to reflect sun light through the façade, as shown in Figure 5.18. The experiment was conducted on July 19, 2018, under a clear sky. The EPD performed an evaluation every 15 min from morning to evening. The glare source was positioned in front of the façade at 15:00, before one of EPD evaluations at 15:05. It was kept at the same position for 15 min and removed at 15:15 before next EPD evaluation at 15:20, affecting only one period. Figure 5.19 a) shows the shading position from a right view perspective before EPD evaluation, with the glare source in the FOV and slats initially inclined at 72° (horizontal slats). When the EPD started its evaluation, the glare source was sensed with its peaky luminance recorded in the sky vector \mathbf{s} . Then the EPD investigated all the possible shading positions that satisfy a minimal daylight provision and the DGP limit for imperceptible glare. Finally, the maximum opening position among them was selected to actuate the blinds, which was 32° , as shown in Figure 5.19 b). The glare source was precisely blocked by the slats of EVB.



Fig. 5.18. Set-up of a curved mirror inserted manually as the glare source

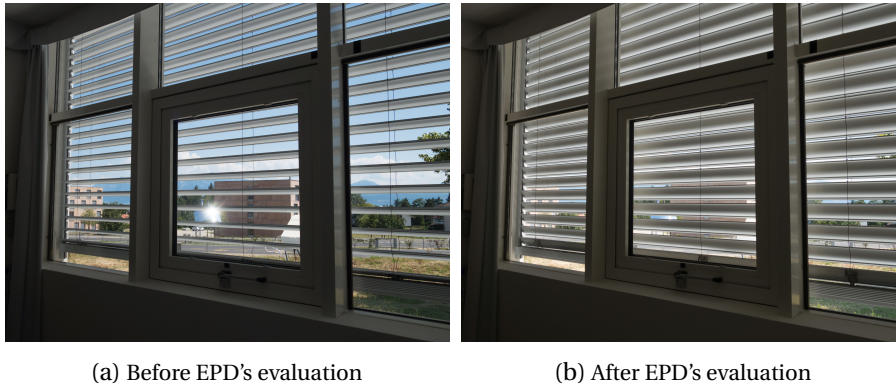
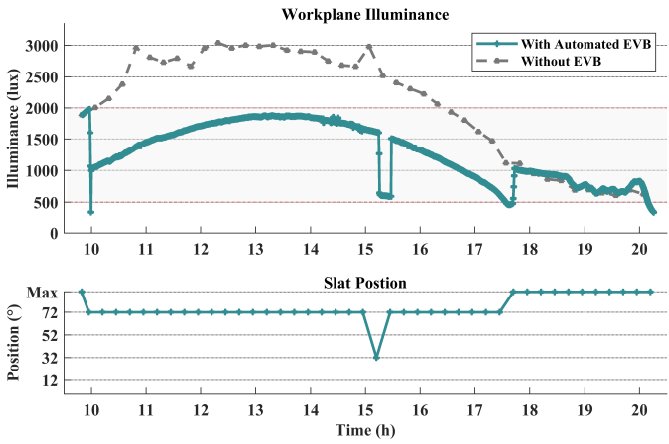
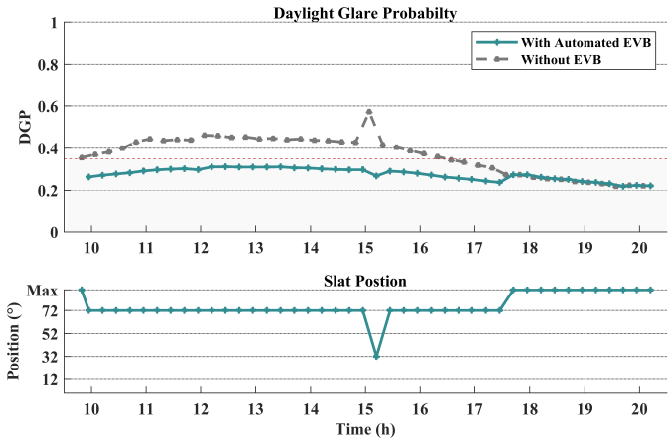


Fig. 5.19. Automated EVB blocking veiling glare from environment (interior view)

Figure 5.20 presents the corresponding WPI and DGP recorded on July 19, 2018. According to Figure 5.20 b), the veiling glare was sensed by the EPD at 15:05 with a spike of DGP in the grey curve without EVB protection case. After an optimization calculation, the slat tilt angle was changed to 32° from the initial 72° . Although it consequently contributed to the dip of WPI in Figure 5.20 a) after excluding the veil glare, sufficient daylight provision was secured by maintaining the WPI above 500 lux. After the glare source was removed at 15:15, the EPD found a new optimal tilt angle and the shading slats were re-opened to 72° (horizontal position) resuming the maximal view outside and admitting sufficient daylight provision in the test module. In this way, the efficiency of the automated 'Eye-sight' Venetian blinds was demonstrated in both veiling glare prevention and re-opening slats timely once daylight conditions improved.



(a) Workplane illuminance (WPI)



(b) Daylight glare probability (DGP)

Fig. 5.20. Measured WPI and simulated DGP in the module

5.5 Survey on users' satisfaction

From Jan. 22nd to Feb. 13th, 2019, 34 subjects (26 males, 8 females) with an age between 20 and 30 volunteered to participate in assessing the daylighting performance of the automated shading system in the daylighting test module, excluding electric lighting. In each section, two subjects seated opposite to each other on the left and right side of the room respectively, as shown in Figure 5.21. Therefore, occupants were able to sense glare from left and right view perspective respectively towards the window, as the defined view position and direction illustrated in Figure 5.6. The EPD performed sky luminance monitoring, lighting computation, and shading position adjustment every 15 min (without manual override). Subjects performed both computer work and paper-based activities, including reading, writing, and typing, during three hours either in the morning (09:00-12:00) or afternoon (13:00-16:00). At the end of each hour, they were requested to fill in a questionnaire, as presented in Appendix A.2, to

Chapter 5. Automated Venetian blinds

show their levels of visual satisfaction on the daylight controlled by the automated shading system. Questions were evaluated at a scale from 1 to 5 about occupants' level of satisfaction or dissatisfaction on perspectives including daylight provision, glare sensation, system response, and view outwards. Experiments were conducted for four days under a clear sky, for two days under a hybrid sky between clear and partly cloudy, for one day under a hybrid sky between partly cloudy and overcast, and for two days under an overcast sky. The average elevation angle of the sun at noon was 25° during this period, when it was challenging for a shading device to prevent discomfort glare, since the sun could be in at least one of the two occupants' visual field during the experiment without occlusion of shading or clouds.



Fig. 5.21. Subjects evaluating performance of the automated shading system

Based on the survey results, the average mark of each question and its corresponding 95% confidence interval were calculated and illustrated in Figure 5.22. Four different color bars denote questions from different perspectives, including daylight provision, glare and contrast sensation, system response, and view outwards. To outline results clearly, mark of each question was transformed and normalized to 1 in order that a higher mark represents a more positive answer. According to the results, Question 2 "The lighting in this room is comfortable" receives a 0.89 average mark. Actually, Questions 1-4 receive relatively high ratings between 0.85 and 0.93 on average, which indicates majority of occupants were satisfied with the daylight provision or WPI to perform reading, writing, and typing tasks. The result of Question 3 (0.93) also reflects that automated shading prevented excessive daylight ingress (or SHG). A minor portion of subjects also showed inclination on a higher level of WPI, which is suggested by the lower bound of the 95% confidence interval of Question 4 "Sufficient light for proper reading/writing/typing", due to the variance of users' preference and sensitivity to light. Regarding glare sensation, Question 6 "I had no glare feeling" has a 0.87 rating, which suggests the majority of occupants' glare sensation was either imperceptible or below perceptible level. It also indicates the shading system generally managed to occlude glare sources in winter with low solar elevation angle, which is suggested by the result (0.85) of Question 7 "Shading blocked the glare source successfully". Since the actuator of shading was improved with smooth motion, Question 9 investigates occupants' distraction from shading movement. Its rating (0.86) indicates occupants' satisfaction on the reduced noise level and

5.5. Survey on users' satisfaction

smooth motion. Although view outwards was secured for occupants, according to Question 10 (0.76), advice including using smaller slats was received to improve view quality. Moreover, the relatively low rating (0.73) of Question 8 "Shading responded quick enough according to variation of weather condition" suggests the performance of the shading can be further improved by the increasing the computation speed and operating frequency (15 min), to improve the performance under partly cloudy sky with rapid motion of clouds, which can occlude the sun and move away in approximately 5 min.

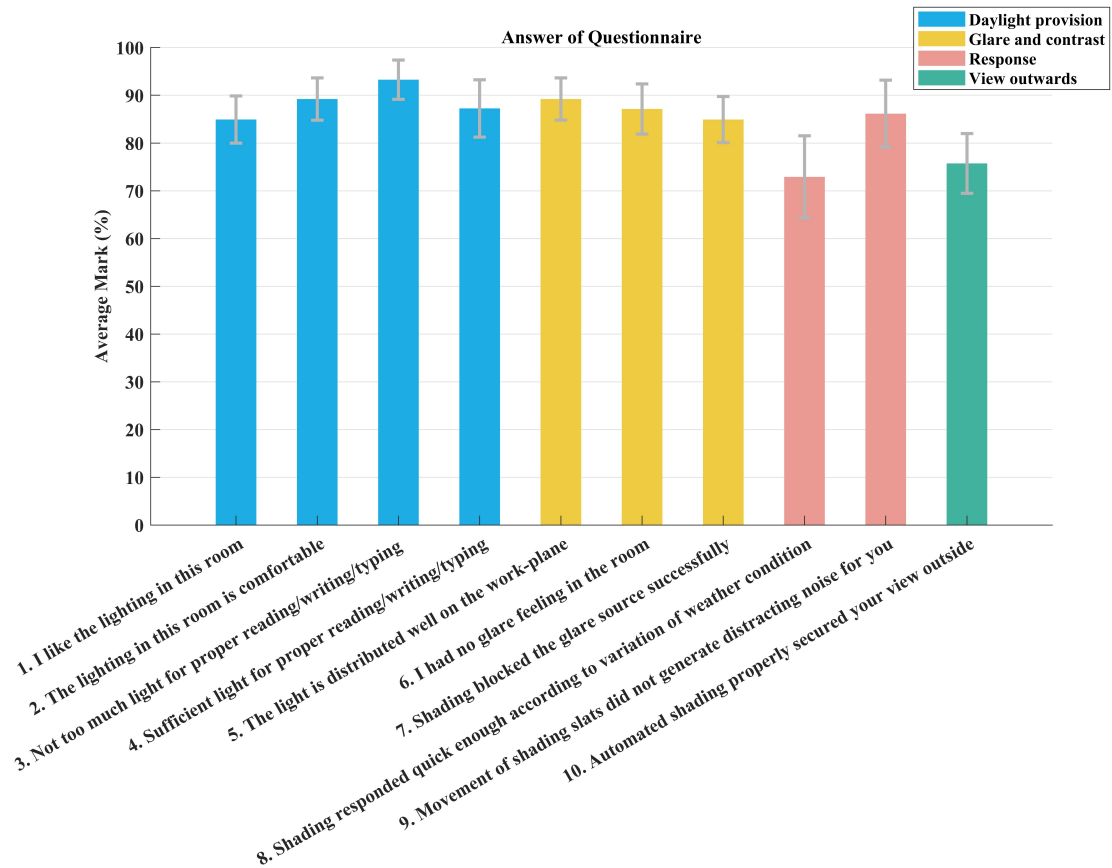


Fig. 5.22. Survey results on visual satisfaction

The survey also asked occupants about their overall comments (or suggestions) on the performance of the automated shading system. Certain occupants also compared its performance with their experience on conventional automated exterior Venetian blinds based on solar irradiance in the "Rolex Learning Center" (RLC), an open-plan library in the EPFL campus, as show in Figure 1.2 d). The provided comments spanned a wide range of options and are categorized as follows, in an order from positive to negative (comments are reproduced verbatim and not edited for proper grammar):

- *Overall satisfaction:*

- *I think that the shading system was better than standard shading system. The distribution of light on the work-plane is very pleasant.*
- *During the three hours, you can really see the difference in terms of shading. Towards [10:30/12:00], the system responds very well.*
- *At the end of the experiment when the shading system was turned off, we could see the difference! The system is very usefull and works well. The work is much better with this shading system.*
- *Glare protection:*
 - *Good shading system, way much better than the one in "Rolex Learning Center". The glare is stopped directly whenever there is too much of it.*
 - *I barely could notice the glare, compared to what I usually notice at the Rolex Learning Center.*
 - *The glare feeling was completely imperceptible from my point of view. I felt really at ease, the lighting was just perfect as well as the level of noise.*
- *Slats motion:*
 - *Comparison with the Rolex Learning Center (RLC): the system in the RLC makes more noise than this one. The movement of shading slats of the experience is softer than the one of the RLC. So this shading changes very slowly (more comfortable while studying.)*
 - *When compared to conventional shading systems, the major improvements one can notice are the fact that the system makes no noise, and that changes (slat movement) are not sudden, but rather gradual (smooth).*
 - *Overall the lighting is consistently comfortable. Minor adjustment is transparent which almost cannot be distinguished without paying extra attention to the shading.*
- *Systematic respond (limited by the EPD's calculation time):*
 - *The system responded quickly enough matching the weather condition without making noise.*
 - *Sometimes the automated shading reacts slowly according to variation of weather condition. Generally, I think that the automated shading is really interesting and permits to have a great lighting without doing anything.*
 - *Prefer the shading to respond more quickly.*
- *Daylight provision:*
 - *I would not mind a bit more light to read or write but for the screen it is adequate.*
 - *The brightness may be marginally increased.*
- *View outwards:*

- *Everything is smoothly controlled for the lighting. But it is true that there the view is not always secured, but this is a defect compared to the efficiency of the automated shading.*
- *Regarding Question 10, it would be nice to have a sort of transparent shading system with a protective film to control the intensity of the light.*
- *Smaller plates to have a better view of the outside and let a bit more luminosity come inside.*

5.6 Commissioning issues

The EPD's real-time daylighting simulation is based on the monitored sky luminance distribution and modelled scene. Regarding the applicability of the automated 'Eye-sight' Venetian blinds in different scenarios, although luminance monitoring quality of the EPD and BTDF of the shading system (light transmission behavior) can be quantified before delivery to users, the modelling of the scene can involve mismatches without proper commissioning. The mismatch between the modelled scene and reality can impact the simulation accuracy and control performance, which is investigated in this section.

Table 5.2 shows the physically measured surface material property of the module interior, regarding reflectance and specularity, as described in Section 5.3.1. The reflectance of each surface material is distinct, ranging from 5.8% of the chair surface to 93.2% of the metallic frame of the door. Their specularity also spans a wide range from 1.2% to 95.0%. The European standard on lighting (EN 12464-1) [49] provides a range of useful reflectance values for major interior surfaces, including wall (0.3 ~ 0.8), ceiling (0.6 ~ 0.9), and floor (0.1 ~ 0.5). Since ceiling and floor commonly have the same area, the average reflectance of ceiling and floor is between 0.35 and 0.7, which is close to the that of the wall. The defined reflectance value was investigated with regard to its influence on lighting computing in an extreme case, assuming a module interior with homogeneous surface reflectance and lambertian reflection. The reflectance of each surface material was set to the same value 'val' in the scene model, as shown in Table 5.2, and their specularity was set to zero.

The interior reflectance value ('val') was investigated at 0, 0.2, 0.4, 0.6, 0.8, and 1.0, respectively, with 0 and 1.0 as two unreachable extremes. Based on the results achieved in Section 5.4.1 on cross validation, an identical simulation input and method were employed, except for the modified reflectance and specularity of the interior material. Sub-figures in Figure 5.23 show the simulated horizontal illuminance in the scene employing various interior reflectance values respectively, contrasting with the reference illuminance recorded by lux-meter sensors (grey line), where stacked lines denote different distances to the façade, from 1 m to 5 m, as explained in Section 5.4.1. Comparing Figure 5.23 b) and Figure 5.11, the simulated horizontal illuminance employing a reflectance value of 0.8, which is close to the average physical reflectance of the wall, ceiling and floor, for all surface materials homogeneously, achieves

Table 5.2 – Reflectance and specularity of surface material in modelled scene

Material	Reflectance		Specularity	
	measured	new	measured	new
Wall	81.3%	val	2.3%	0
Ceiling	81.3%	val	2.3%	0
Floor	29%	val	8.5%	0
Table surface top	52.3%	val	22%	0
Table leg	8.2%	val	16.9%	0
Table surface bottom	83.2%	val	29.2%	0
Table separator	59.2%	val	95.0%	0
Window Frame	82.1%	val	52.1%	0
Floor edge	24.7%	val	17%	0
Floor blanket	62.5%	val	2.5%	0
Door interior	83%	val	73.5%	0
Door Frame	93.2%	val	82.7%	0
Cabinet surface	53.2%	val	23%	0
Chair Top	5.8%	val	1.2%	0
Chair Leg	6.4%	val	24.7%	0
Curtain	69.2%	val	3.4%	0

an equivalent performance to that using physically measured reflectance and specularity values. The significance of average reflectance can be explained by the fact that the surface area associated with reflection is dominated by the wall, ceiling and floor in the module. Higher reflectance values contribute to incrementing horizontal illuminance (Figure 5.23 a)), while lower reflectance values contribute to its reduction (Figure 5.23 e)). The impact is more pronounced on locations farther away from the façade, which can be explained by the fact that the main light flux received by the sensors in deep spaces issues from reflections on interior surfaces, instead of direct rays from the sky.

5.6. Commissioning issues

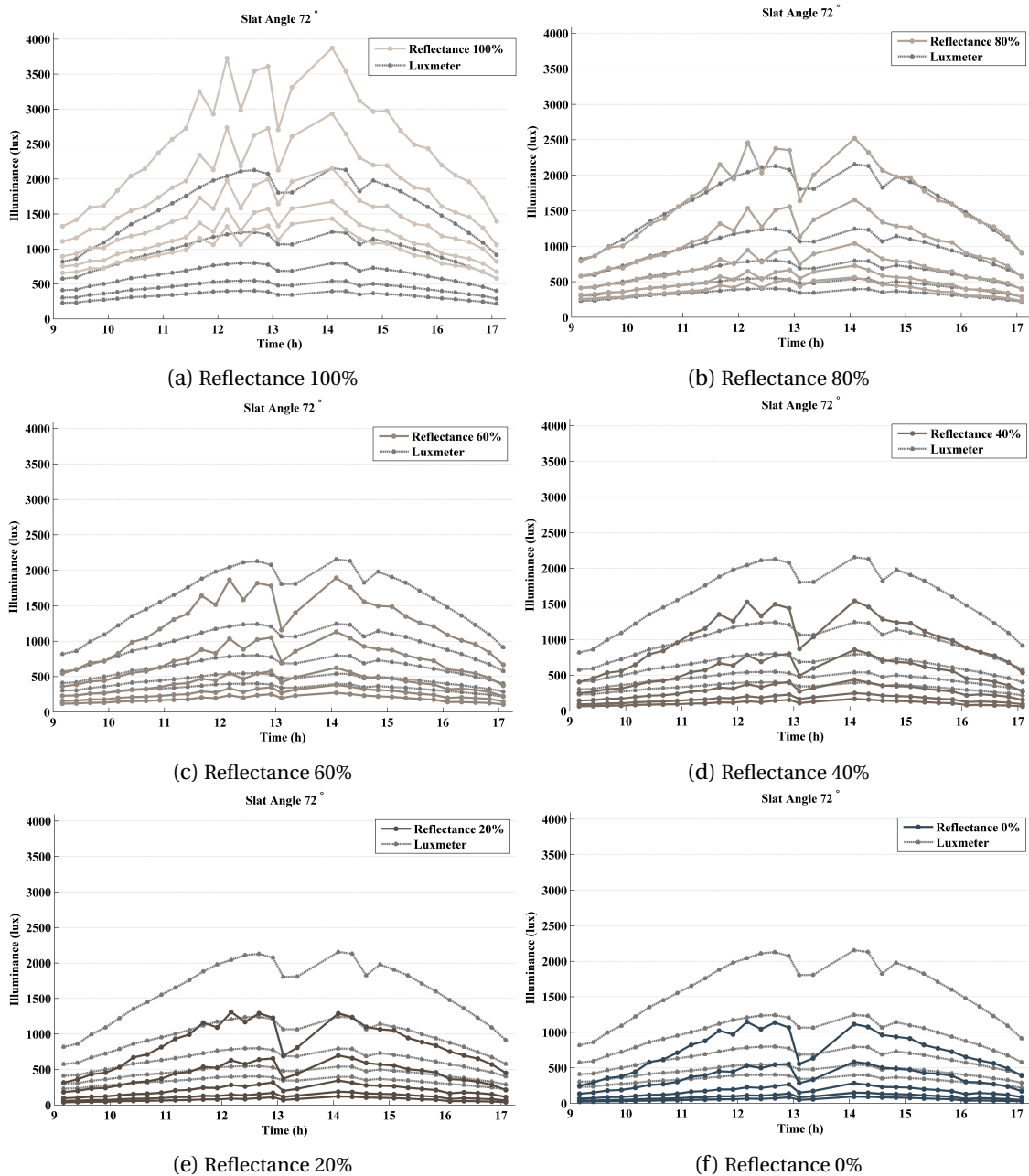


Fig. 5.23. Simulated horizontal illuminance employing the same reflectance for each interior surface

To quantify the impact, the relative average bias of horizontal illuminance versus interior reflectance variation was calculated for different positions, as shown in Figure 5.24. The bias for a position close to the façade is relatively moderate, especially for the work-plane center position defined at a 1.5 m distance for EVB control, as described in Section 5.3.4. Since extreme reflectance of both 0 and 1 is not achievable in reality for a building interior, the deviation of illuminance for a reflectance varying between 0.3 and 0.8 is highlighted for the position at a distance of 1.5 m to the façade; this range is between -45% and 5%. In the

worst case, when reflectance of the interior is set to an arbitrary value far away from reality, a maximum of 45% deviation of WPI can be expected at 1.5 m distance to the façade diluting the target WPI range [500,2000] lux to be [275, 3600] lux in reality for shading control.

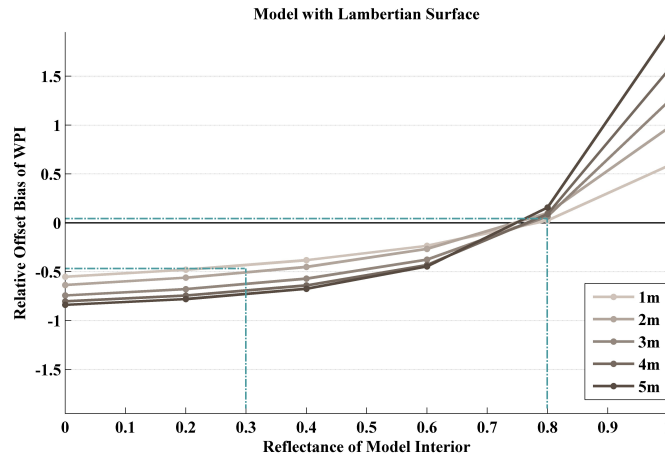
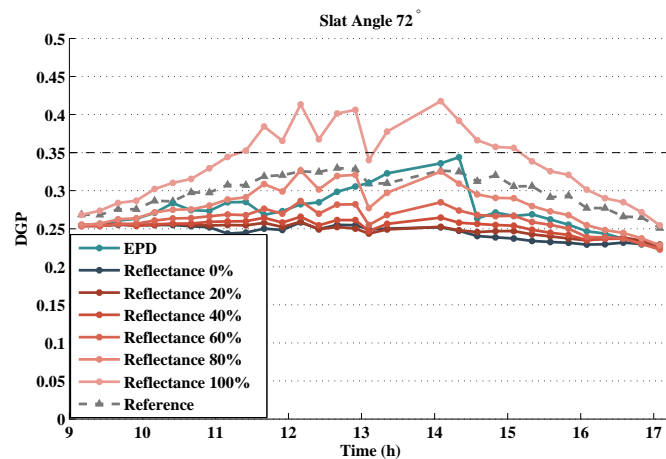
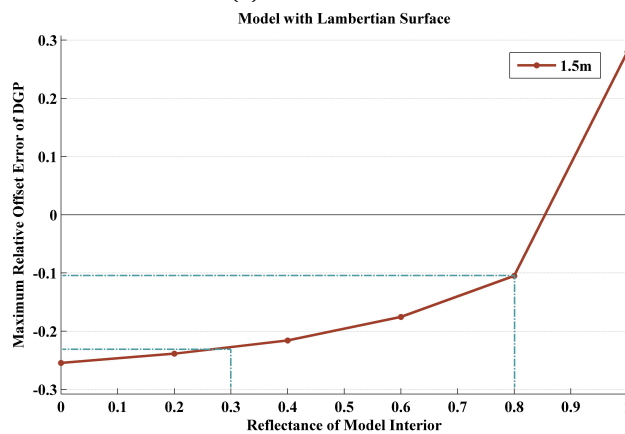


Fig. 5.24. Deviation of horizontal illuminance versus reflectance of scene interior

The impact of the indoor reflectance on DGP was also investigated based on the simulation performed in Section 5.4.1 on cross validation, as presented in Figure 5.25 a). The green and grey curves show the results achieved in Section 5.4.1 by the EPD and reference camera respectively, while shaded red curves illustrate the simulated DGP based on various interior reflectance values, using the same sky luminance map monitored by EPD. A comparable performance is achieved with a reflectance value of 0.8 for all surface materials as with physically measured reflectance values. Figure 5.25 b) presents the maximum relative offset versus a variation of the reflectance value at 1.5 m distance to the façade, where the deviation contributed by reflectance range [0.3, 0.8] is highlighted. The worst case of setting an incorrect value can entail a -22% deviation of DGP, shifting the target DGP below 0.35 to be below 0.44.



(a) DGP deviation



(b) Maximum relative offset of DGP

Fig. 5.25. Simulated DGP employing the same reflectance for each interior surface

5.7 Conclusion

This chapter presents the design and validation of a highly integrated shading automation system, namely the automated 'Eye-sight' Venetian blind, which optimizes the position of blinds to satisfy occupants' visual comfort and maximizes their view outwards. Its control is based on monitoring of the sky (and landscape) luminance distribution and real-time lighting simulation for building interior performed by an embedded photometric device (EPD) in the blind frame (or shell), which determines an optimal shading position according to the dynamic sky conditions. The shading is demonstrated to reduce glare risk and to regulate daylight provision in a building interior within a confined range ([500, 2000] lux) of WPI, saving artificial lighting and preventing excessive cooling load due to solar heat gain (SHG) in warm seasons.

The EPD, acting as both a sensing unit and controller for shading automation, was demon-

strated to achieve a simulation accuracy with 10% RMSE in work-plane illuminance and glare risk (DGP) calculation, by cross validating with lux-meters and a reference camera inside a daylighting testbed. The shading control experiment was conducted during multiple weeks, spreading across summer, autumn, and winter, under various sky conditions including clear, partly cloudy, and overcast. The results showed that the controller was able to close and re-open shading timely under different sky conditions. It was found that two movements of slats during a day with clear skies were sufficient to secure sufficient WPI and prevent glare for the EVB during summer and autumn, when the WPI was regulated within a confined range ([500, 2000] lux) during 97% of working time. Under partly cloudy skies, the controlled shading position was able to respond following the rhythm of dynamic sky conditions, when the WPI was constrained within the range of [500, 2000] lux during between 70% and 93% of working time depending on cloud density. Although the number of movements of the shading slats increased to more than 10 times per day to cope with the variation of sky conditions, disturbance for occupants was reduced by means of an improved actuator with smooth motion and the priority of controller in tilt angle adjustment. Its efficiency in veiling glare protection due to secondary reflection on specular surfaces from the surrounding environment was also demonstrated by using a physically inserted glare source. The shading managed to occlude the glare source and re-open slats timely when the glare source was removed. Based on a reduction in WPI, the projected SHG mitigation was estimated to reach 47% on average in a warm climate.

A study on 34 subjects experiencing the shading system in winter showed occupants' visual satisfaction on sufficient daylight provision, efficient glare protection, and quietness of slat movement. Regarding its commissioning in practice, the reflectance value of the modelled interior material was investigated with regard to its impact on simulated WPI and DGP values. According to the results, matching of the overall interior reflectance is adequate for the simulation quality in WPI and DGP computation, without exact reflectance of each material. In the worst case, if defining an incorrect reflectance for building interior, the controlled constraints can be diluted with a 45% bias in WPI and 20% bias in DGP.

By integrating all the components, including the microprocessing unit (MPU), sensors, and actuators, into a Venetian blind, this integrated design has the following merits and can potentially address the limitations of conventional shading control systems as mentioned in Section 2.4 and the first, second and third research questions of the thesis in Section 2.6:

- Since EPD's imaging system points at the exterior space, privacy issue of using cameras for assessing the building interior can be avoided, and occupants' movements in buildings do not occlude the FOV of the imaging system of EPD.
- The shading control based on the optimization process excludes distracting oscillation of a close-loop system, in regulating WPI and DGP.

- Daylight control performance is secured via the real-time lighting simulation accuracy based on the luminance monitoring of the sky (and landscape).
- The controlled shading can prevent discomfort glare due to inter-reflections between shading slats, since glare risk for various slat tilt angles is analysed in real-time through lighting simulation.
- Its feature has been demonstrated in preventing veiling glare due to secondary reflections on specular surfaces from the surroundings, since the control is based on the analysis of exterior information.
- The controller is able to close shading to suppress daylight penetration and re-open slats timely when daylight provision is insufficient.
- As a decentralized stand-alone system, the automated shading is not limited by the availability of weather data or weather stations.
- Pre-knowledge of location and window orientation are not required, since a relative coordinate is established in the controller.
- As an integrated shading device, the system excludes the installation of sensors or connection wires in the building interior, which saves cost and complexity in commissioning and simultaneously enhance convenience of application.

Although convincing results have been achieved on unilateral façades, its application in open-plan offices will be further investigated in the future. Since daylight provision can be calculated with precision by the controller, its integration with artificial lighting control is possible when daylighting is insufficient. Also to be studied are the controller's operating frequency, improvement of computation speed by using advanced hardware, and reduction of computation loads by employing a simplified algorithm.

6 Automated electrochromic glazing

6.1 Introduction

Well-designed electrochromic (EC) glazing control can improve energy performance of buildings and visual comfort of occupants in highly glazed buildings. This chapter designed and demonstrated a compact integrated EC glazing automation system to control tint states of a split-pane EC window according to variations in sky conditions. The control is based on monitoring the luminance distribution of the sky and real-time lighting computation for building interior, using an embedded photometric device (EPD). It optimizes tint states of EC glass to offer sufficient daylight provision, mitigate excessive solar heat gain in buildings, and temper discomfort glare for occupants. 'In-situ' experiments were conducted in a full-scale testbed to demonstrate the performance under various sky conditions. Experimental results showed 83% of the working time for work-plane illuminance (WPI) and 95% of the time for daylight glare probability (DGP) were constrained within comfort range ($WPI \in [500, 2000]$ lux, $DGP \leq 0.35$) by the automated EC glazing (controlled by EPD) under clear skies, 68% of the time for WPI and 94% of the time for DGP in comfort range under clear skies with thin clouds, 62% of the time for WPI and 85% of the time for DGP in comfort range under partly cloudy skies. The chapter is based on the article "Split-pane electrochromic window control based on an embedded photometric device with real-time daylighting computing" submitted to the "Building and Environment" journal by Wu et al.

6.2 Design

6.2.1 Systematic set-up of the automated EC glazing

The design of the automated EC glazing integrates an embedded photometric device (EPD) that is attached on the glass, with its imaging system targeted towards outdoors as illustrated in Figure 6.1, to control glazing tints with optimized visual comfort for occupants, as a stand-alone system. The EPD acts as both a sensing unit and a controller for the EC glass. With a vision of outdoor space, the EPD monitors luminance distribution of the sky vault and

landscape faced by the façade, including the sun, clouds, sky background, and landscape objects. Based on a generated luminance map together with a geometric model of the building interior, EC tint states are determined by the real-time lighting simulation performed on the EPD. It evaluates work-plane illuminance (WPI) and glare risk for various combinations of glass tint; the optimal tint state is determined to offer sufficient daylight provision and minimal discomfort glare for occupants within the building interior. The highly integrated design enhances convenience during installation and application, since sensors or wiring connections are not required within the building interior. Privacy issues of using cameras with vision of a building interior are avoided, since the imaging system of the EPD targets the outdoor space. Furthermore, the circuitry of an EPD is compatible with that of an EC glass driver, since both are driven by low DC (direct-current) voltage, which can be integrated together on a single printed circuit board (PCB).

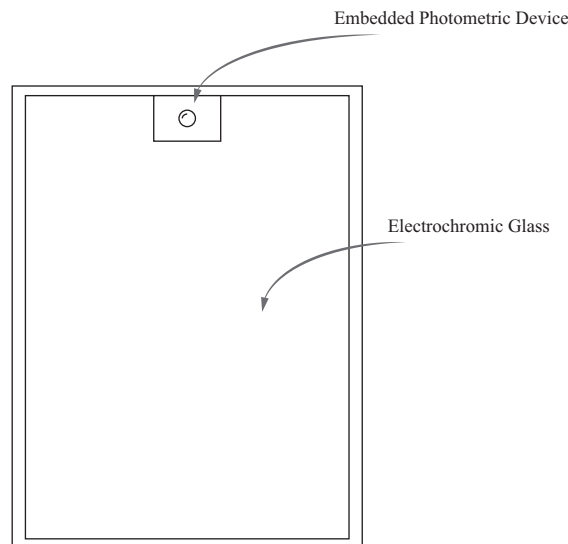


Fig. 6.1. Design of an EC glazing integrated with an EPD (view from the outdoors towards the glass surface)

6.2.2 Embedded photometric device (EPD)

The EPD, proposed and demonstrated by Wu et al. [145, 178], mainly comprises a low-cost image sensor, lens, and a field programmable gate array (FPGA) processor. The imaging system of the EPD was deliberately calibrated in the spectral response, vignette effect, signal response curves, and geometric mapping. After spectral correction by optical filters, spectral response of the imaging system matched the CIE photopic luminosity function $V(\lambda)$ [174], which emulates the response of human eyes. The spectral correction error f'_1 reaches 8.89% for photometric variable measurements. Based on its fast shutter speed, the EPD has a wide range of luminance

detection from 120 cd/m^2 to $3.78 \times 10^9 \text{ cd/m}^2$ (150 dB) based on HDR imaging techniques, which covers both the luminance of shadowed landscape during daytime and that of the direct sun orb ($\leq 1.6 \times 10^9 \text{ cd/m}^2$) as the two extremes. The EPD monitors the luminance distribution of the sky vault and landscape, within a 1.3 second acquisition time, and generates a luminance map of 1.2 million patches. In conjugation with a modelled scene, the real-time daylighting simulation can be performed on the EPD to assess indoor lighting conditions. Based on a high-resolution luminance map, accuracy of lighting simulation performed on the EPD was validated in studies for façades with clear glass on the EPFL campus in Lausanne, Switzerland [145, 3] which achieved below 20% error in simulating of WPI distribution under dynamic sky conditions. Details of the EPD and lighting simulation capability are also illustrated in Chapter 3.

6.3 Methodology

6.3.1 Daylighting testbed

The space selected for this study is a full-scale outdoor testbed (Advanced Windows Testbed, Building 71t) with three parallel office rooms located at the Lawrence Berkeley National Laboratory in Berkeley, CA. The three rooms are designated as Room A, B, and C, with Room A to the east, Room B in the center, and Room C to the west, from right to left as shown in Figure 6.2 a). The dimension of each office room is $3 \times 4.5 \times 3.3 \text{ m}^3$, furnished with an identical interior set-up and a south facing unilateral façade with a 0.64 window-to-wall ratio. Each façade of the two rooms (Room B and C) is equipped with a split-pane EC glass, of which the upper daylight section and lower view section can be controlled independently. The EC glazing (from Sage Glass) has four states of visible light transmittance: 60%, 18%, 6%, and 1%, according to Table 6.1. It takes 10 ~ 30 min for transition from the clear (60% transmittance) to fully tinted (1% transmittance) state, depending on incident solar radiation and outdoor temperature. The façade of Room A on the right side is a low-emittance double glass with 62% visible light transmittance is used as a reference. The modelled scene of each office is illustrated in Figure 6.2 b).

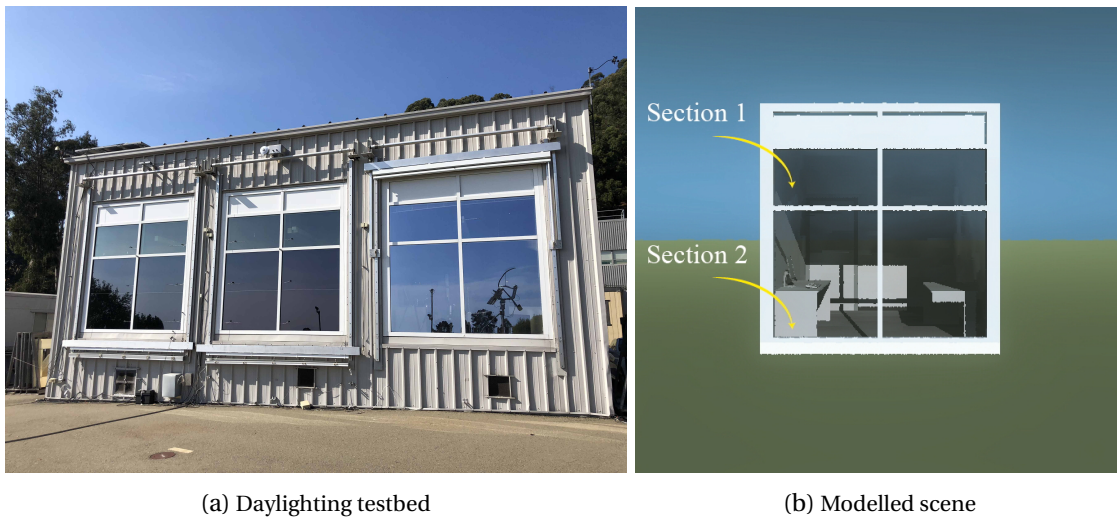


Fig. 6.2. A daylighting testbed with three parallel offices

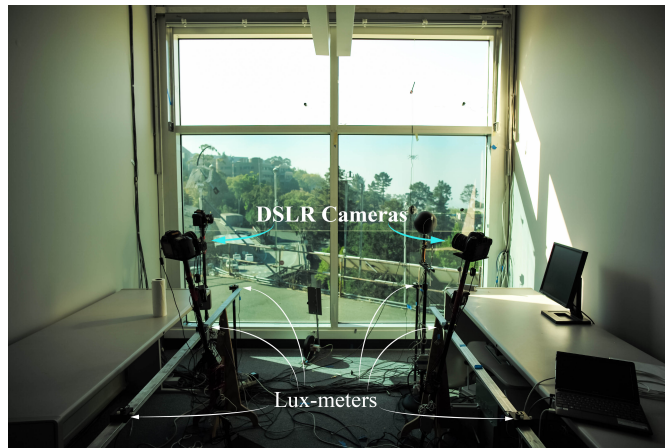
Table 6.1 – Property of the EC glass at four tint states

Tint state	Visible transmittance	Solar transmittance	SHGC	U-factor
Clear	60%	33%	0.41	0.28
Light tint	18%	7%	0.15	0.28
Medium tint	6%	2%	0.1	0.28
Full tint	1%	0.4%	0.09	0.28

In the prototyping phase, the EPD was positioned outdoors in front of the EC façade (0.5 m distance to the façade, 1.5 m above the ground) with its axis of lens in the orthogonal plane of the façade for experimental convenience, as shown in Figure 6.3 a), instead of attaching the EPD to the glass as designed. It is assumed that the position translation of the imaging system has negligible influence on the lighting simulation. The EPD, as a controller, was connected to the EC glass driver to provide tint state signal, according to optimization results. The optimized tint states were determined by the real-time lighting simulation results based on the monitored luminance distribution of the sky (and landscape) performed by the EPD. In each room interior, lux-meters (LiCor LI-210SA, $\pm 3\%$ of reading,) and cameras (Canon EOS 5D) were positioned to measure WPI and monitor discomfort glare as a reference, for purposes of cross validation and assessment of control performance. The digital single-lens reflex (DSLR) camera, employing HDR imaging techniques, composites multiple low dynamic range images into an HDR image. The HDR image, calibrated by the vertical illuminance measured by an adjacent vertical sensor, is used to calculate glare risk metrics, including daylight glare probability (DGP), using the evalglare program in RADIANCE software [182] from the captured view point.



(a) EC glass with EPD controller (Prototyping)



(b) Lux-meters and cameras offering reference measurement (Validation)

Fig. 6.3. Experimental set-up

6.3.2 Daylighting simulation

In this chapter, WPI and DGP are two metrics that are used to evaluate visual satisfaction of occupants in the EC glazing control. Although quasi real-time lighting simulation results can be realized using the backward ray-tracing algorithms [183], the iterative computation of these algorithms is time consuming to assess lighting for various tint state combinations of EC glass, especially on a compact platform. Therefore, a matrix algebraic approach [177, 160] of lighting simulation is employed on the EPD platform in order to make iterative calculation more time-efficient. The idea is to employ the RADIANCE software [182] to pre-compute a set of matrices that relate the sky luminance in each direction to the contributed WPI in building interior. Instead of using the original five-phase method developed for sky models [160], the matrix algebraic approach is modified for split-pane EC glazing control based on high-resolution monitoring of the sky luminance distribution as shown in Equation (6.1), where numeric subscripts 1 and 2 denote the independent contribution of the upper daylight

window section and of the lower view window section respectively, as illustrated in Figure 6.2 b). Equation (6.1) calculates the horizontal illuminance vector of work-plane \mathbf{i}_{wp} , in which the mean is regarded as WPI in EC glazing control. Equation (6.1) separates the contribution from the sky vault and the sun due to the different resolution required for both of them. The product of \mathbf{VTDs} calculates the horizontal illuminances (HI) at work-plane contributed by the sky vault and landscape, while product of $\mathbf{C}_{ds}\mathbf{s}_{sun}$ computes the HI contributed by the direct component of sunlight, through the upper daylight window section or through the lower view window section. Noticeable error in illuminance calculation using the five-phase matrix algebraic approach has been reported by Lee et al. [111], which is due to the resolution mismatch between the transmission matrix \mathbf{T} (commonly 10 – 15° resolution) and the sun disk which only spans an apex angle of 0.53°. In order to reduce the simulation error and to resolve the veiling glare due to secondary reflection on specular surfaces from the surrounding environment, matrices in Equation (6.1) employ a high resolution angular basis, based on the subdivided Tregenza angular basis [156], instead of the commonly used Klems angular basis (10 – 15° resolution) [176]. In Equation (6.1), each element of sky vector \mathbf{s} (Reinhart MF:5, 3602 elements or directions) spans an apex angle of 2.4°, and each incident and exiting direction in transmission matrix \mathbf{T} (Reinhart MF:4, 2305 × 2305) subtends an apex angle of 3°. Therefore, after generating the luminance map of the sky and landscape with 1.2 million patches on the EPD, the solar component is extracted from the luminance map and it is sub-sampled with 3602 elements to generate a sky vector \mathbf{s} after being pre-filtered. The sun position is discretized into 5176 locations (Reinhart MF:5) in \mathbf{s}_{sun} , each spanning an apex angle of 0.53°, and the sun is approximated to the nearest location with a maximal 1.5° bias. Although preparation of these matrices is relatively time consuming, the iterative calculation of horizontal illuminances \mathbf{i}_{wp} (performed on the EPD) only involves matrix multiplication, which is substantially more time-efficient. To generate view images (resolution 500 × 500) for DGP calculation, the routine is similar to that of the horizontal illuminance vector \mathbf{i}_{wp} in Equation (6.1); the only differences are matrices \mathbf{V} and \mathbf{C}_{ds} that are modified into arrays of view images.

$$\mathbf{i}_{wp} = \mathbf{V}_1\mathbf{TD}_1\mathbf{s} + \mathbf{C}_{ds1}\mathbf{s}_{sun} + \mathbf{V}_2\mathbf{TD}_2\mathbf{s} + \mathbf{C}_{ds2}\mathbf{s}_{sun} \quad (6.1)$$

- \mathbf{C}_{ds1} is the solar coefficient matrix for the upper daylight window section, which is associated with the contribution from the solar luminance to the horizontal illuminances at corresponding positions on the work-plane through the upper daylight window section
- \mathbf{C}_{ds2} is the solar coefficient matrix for the lower view window section, which is associated with the contribution from the solar luminance to the horizontal illuminances at corresponding positions on the work-plane through the lower view window section
- \mathbf{D}_1 is the daylight matrix for the upper daylight window section, which relates the luminance of each sky patch to each incident direction on the front EC glass plane of the upper daylight section

- \mathbf{D}_2 is the daylight matrix for the lower view window section, which relates the luminance of each sky patch to each incident direction on the front EC glass plane of the lower view section
- \mathbf{i}_{wp} is a vector containing the computed illuminance at defined position on the work-plane in the testbed
- \mathbf{s} is the sky vector, each element of which contains the luminance value from a sky patch, excluding the solar component
- \mathbf{s}_{sun} is the direct sun vector, a sparse vector containing only the luminance of the solar component with an apex angle of 0.53°
- \mathbf{T} is the transmission matrix (BTDF) of the EC glass, which relates light flux transfer from each incident direction on the front glass plane to an emergent direction on the glass interior plane
- \mathbf{V}_1 is the view matrix for the upper daylight window section, which is associated with the light contribution from each emergent direction from the upper daylight window section (interior plane) to the horizontal illuminances at corresponding positions on the work-plane
- \mathbf{V}_2 is the view matrix for the lower view window section, which is associated with the light contribution from each emergent direction from the lower view window section (interior plane) to the horizontal illuminances at corresponding positions on the work-plane

The bi-directional transmittance distribution function (BTDF) is employed in the lighting simulation as the matrix \mathbf{T} in Equation (6.1). BTDF, which characterizes light transmission behavior of a complex fenestration system (CFS), is defined as the ratio of emergent luminance to incident illuminance on the incident sample plane [106]. BTDF has been commonly used to represent a CFS in lighting simulation without knowledge of material property or geometry of a CFS, which speeds up computation. In this chapter, the 'genBSDF' program in RADIANCE software was employed to generate the BTDF data of the EC glazing at different tint states. The original genBSDF program was modified to generate a BTDF based on the Tregenza angular basis subdivided by a factor of 16 (Reinhart MF:4, 2305×2305) instead of the default Klems angular basis (145×145), to resolve small-scale glare source in lighting simulation. Figure 6.4 illustrates the tone-mapped HDR image of the BTDF matrix of EC glazing at 18% transmittance, which is essentially a diagonal matrix (black region denotes zero).

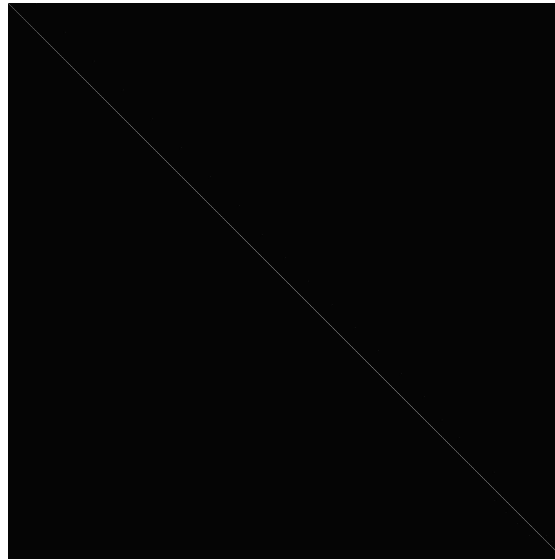


Fig. 6.4. Tone mapped image of the BTDF matrix of EC glass at 18% transmittance

6.3.3 Control logics

EC glass tint control is an optimization process to ensure visual comfort for occupants, satisfy minimum daylight provision requirements defined by EN12464-1, and maximize occupants' view outwards, according to Equation (6.2). The work-plane is defined as a $1.3 \times 1.5 \text{ m}^2$ rectangle at the height of 0.8 m above the floor in the center of the office, as a virtual desk enclosed by the six lux-meters as shown in Figure 6.3 b). The horizontal illuminances at the same positions of lux-meters (at 0.75 m, 1.5 m, 2.25 m distance to the façade) are calculated by the EPD based on a monitored luminance map of the sky, the mean of which is regarded to be WPI. The WPI is constrained to be greater than 500 lux, which satisfies minimal daylight provision requirement (En 12464-1 [49]), and to be lower than 2000 lux, which mitigates excessive daylight provision and solar heat gain [184]. Two view perspectives are defined at the mid-point of two parallel edges of the virtual desk at the height of 1.2 m, orienting 45° and 135° respectively, towards the façade with a 10° elevation angle, which makes both the window and sunlit area on the wall to be in the center of FOV, as the lens direction of cameras shown in Figure 6.3 b). The defined view directions emulate two occupants sitting on two sides of the virtual desk and facing the façade as one of the worst cases regarding glare risk, since major potential glare sources (light transmitted through the window or reflected from the wall) are in the FOV of occupants. The larger DGP value from the left (DGP_L) or right (DGP_R) perspective is constrained below 0.35 by the EPD controller, which limits the glare risk within the imperceptible level for both view directions. When the EC glass approaches a lower transmittance state, the outside view becomes darker and is tinted with a blueish color shift. To optimize the view quality for occupants, the cost function is established to maximize transmittance of the lower view window section β_2 , provided that the constraint is satisfied with regard to the daylight provision (WPI) and glare risk (DGP).

Maximize:

$$\beta_2 \quad (6.2a)$$

Subject to:

$$500 \text{ lux} < \text{WPI} < 2000 \text{ lux} \quad (6.2b)$$

$$\text{DGP} = \sup\{\text{DGP}_l, \text{DGP}_r\} < 0.35 \quad (6.2c)$$

Figure 6.5 illustrates a flowchart of EPD evaluation in tuning tint states of the split-pane EC glass to optimize the visual satisfaction of occupants. The time consumption required for each stage is labelled next to the corresponding diagram block. The EPD starts with monitoring the luminance distribution of the sky vault and ground facing the façade, including that of the sun, clouds, the sky vault, and landscape. A high-resolution luminance map is generated and is then transformed into a sky vector \mathbf{s} with 3602 elements and a direct sun vector \mathbf{s}_{sun} with solar luminance in one of its 5176 elements, as defined in Equation (6.1). Following matrix multiplication in Equation (6.1), the WPI is calculated for 16 EC tint combinations, with four tint states of the upper daylight window section and four states of the lower view window section, the computation of which is accomplished in 10 ~ 20 s. The EC tint combinations with corresponding WPI within the constraint are selected for further assessment of glare risk. If no combination satisfies the WPI range, this suggests the WPI is lower than 500 lux for all tint combinations and the optimal tint states should be clear (60% transmittance) for both EC glass sections to admit a maximal daylight flux, since it is impossible for WPI to exceed 2000 lux when both glazing sections show a 1% transmittance. Next, the HDR view images are generated for selected tint combinations, which requires 400 ~ 500 s, and then the corresponding DGP is calculated from left and right view perspectives. The optimal tint combination is the one that satisfies its DGP below the perceptible glare threshold, with the clearest possible tint in the lower view window section to secure outwards view quality. Finally, the EPD sends a control signal of the determined tint combination to the EC glass driver to adjust the daylight injection into buildings. Although one EPD run of control algorithms requires 8-10 min, this paper employs an interval of 15 min, to leave a 50% time margin and to synchronize with reference apparatuses for comparison.

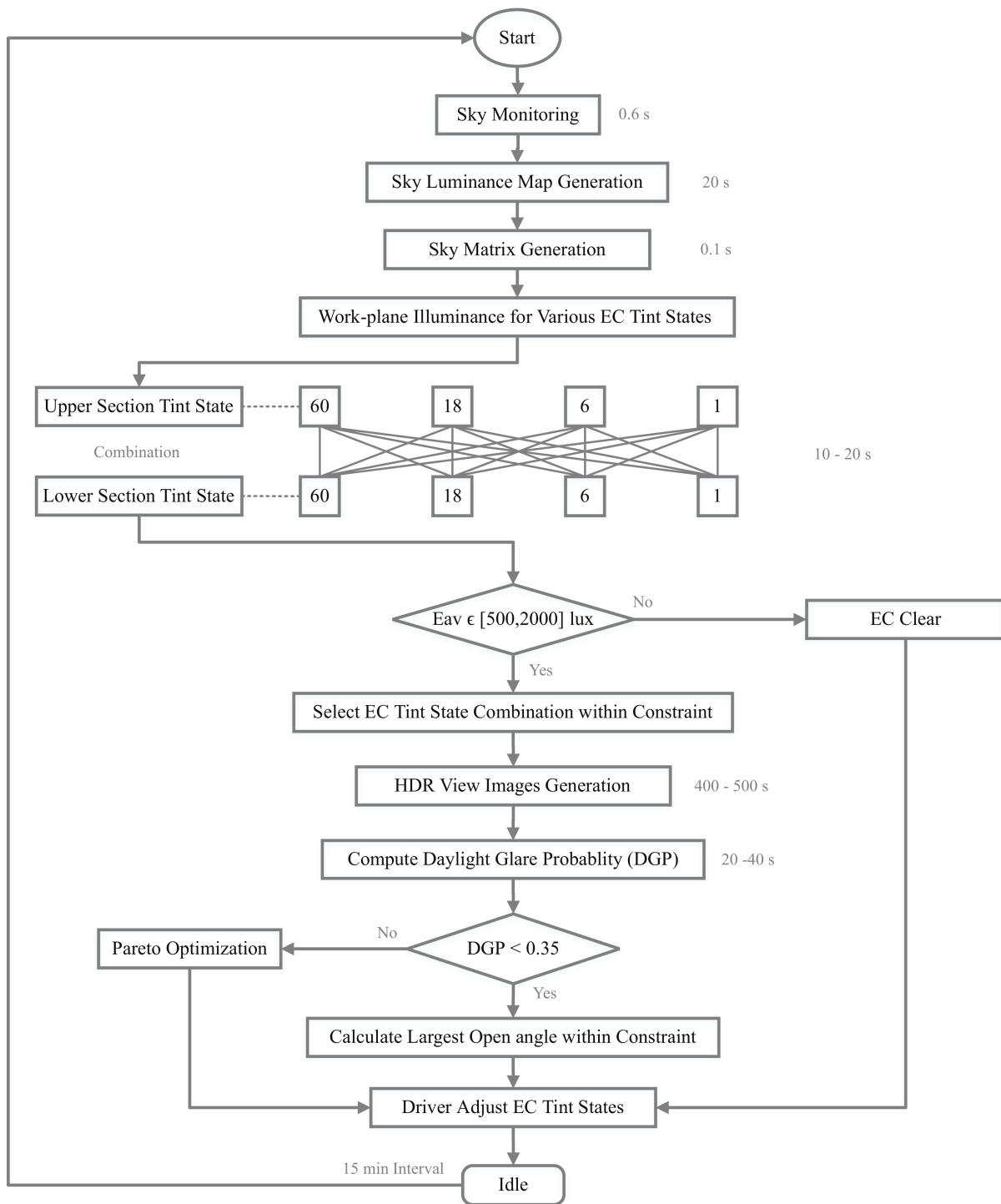


Fig. 6.5. Flowchart of each EPD run in EC glass control

In order to outline the performance of daylighting, regulated daylight condition in Room C, with its EC glass control performed by the EPD, was compared with that in Room A and B, as illustrated in Figure 6.6. The interior set-ups are identical for the three rooms with identically

positioned lux-meters and reference cameras; the only difference is the window glass states. The EC glazing of Room B is controlled based on the weather data (direct normal and diffuse horizontal irradiance) at LBNL; Perez all-weather model is used as input to the same matrix algebraic approach introduced in Section 6.3.2, as a conventional control case. With low-emittance double glazing, Room A acts as a reference case illustrating a daylit environment without dynamic control.

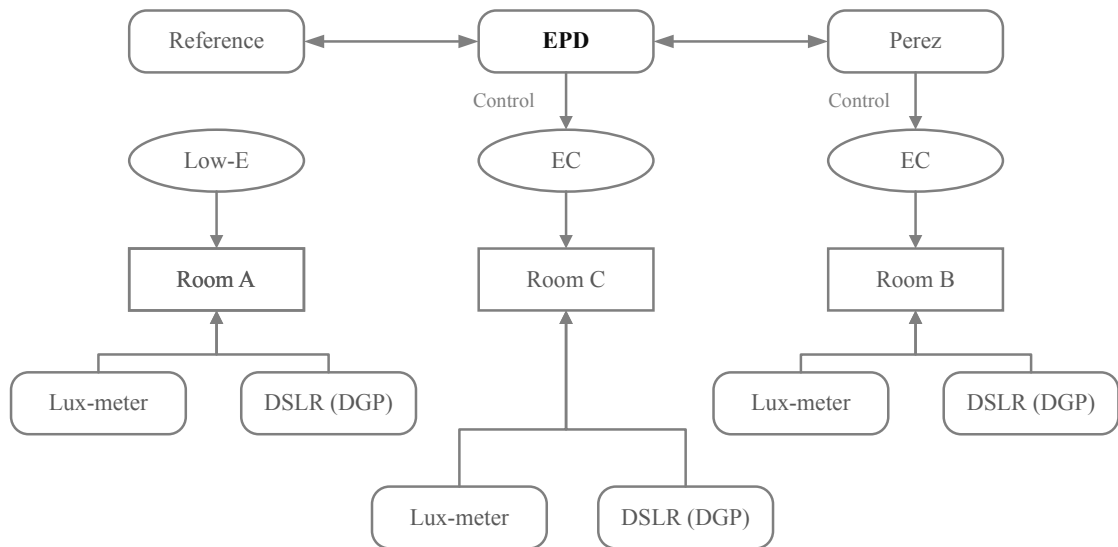


Fig. 6.6. Parallel experiments assessing EC glazing control

6.4 Empirical validation

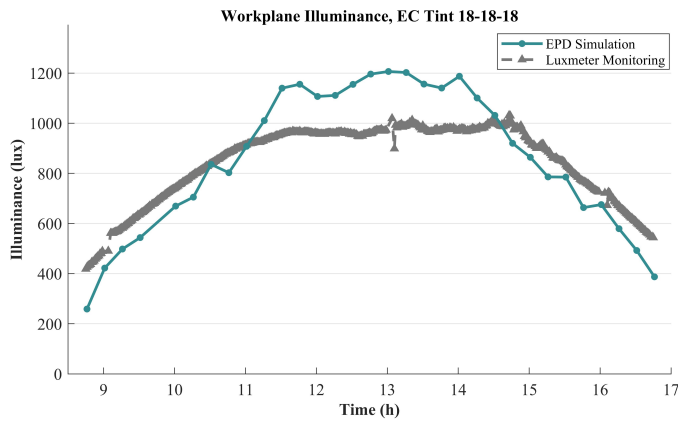
6.4.1 Cross comparison

Although the EPD was demonstrated in its capability of real-time lighting simulation of work-plane illuminance by Wu et al. [145, 180] in several studies, which is also illustrated in Section 3.4, a cross comparison experiment was conducted to further assess the performance of EPD in WPI, image rendering, and DGP calculation in the testbed with static tinted EC glazing.

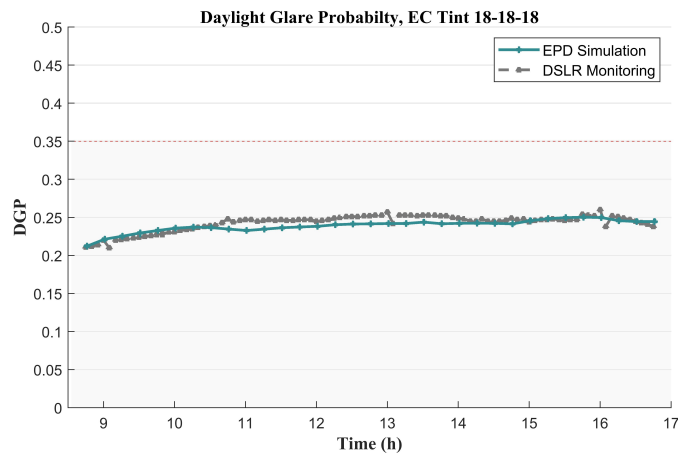
The experiment was implemented under a clear sky on Sept. 21st (maximum solar elevation angle 53°). The EC façade was tinted at 18% transmittance (light tint) for both the upper daylight and lower view window sections throughout the day. The EPD was positioned in front of the testbed to monitor luminance distribution of the sky and to perform a lighting simulation in WPI and DGP every 15 min from morning to evening at the defined interior positions as described in Section 6.3.3. As a reference, lux-meters were used to monitor the WPI every minute and cameras recorded HDR view images at 5 min intervals, based on which reference DGP was computed. Figure 6.7 shows the WPI and DGP in sub-figures a) and b)

Chapter 6. Automated electrochromic glazing

respectively, where green curves denote simulated value performed on the EPD, and grey curves represent the measured quantity from reference apparatuses. The density of data points on the green and grey curves are different, since the EPD performed the lighting simulation at a lower frequency as compared to the sampling frequency of the reference lux-meters and cameras. The average root-mean-square error (RMSE) of the simulated WPI is 17.6% and that of DGP is 2.7%, as compared to reference values.



(a) Workplane illuminance (WPI)



(b) Daylight glare probability (DGP)

Fig. 6.7. WPI and DGP with EC glazing at 18% transmittance

In a second comparison, the upper daylight glass section was set to 1% transmittance and the lower view glass section was set to 6% transmittance. Figure 6.8 shows a rendered view image performed on the EPD and an image captured by the camera on the right side in the testbed respectively at the same time from identical view perspectives. Good correspondence on the sunlit area and shadow on the wall can be found between the two sub-figures. Although the landscape of sub-figure a) has a mosaic pattern due to the sub-sampling process in generating the sky vector, the landscape profile is discernible and match the captured HDR view image as shown in sub-figure b).

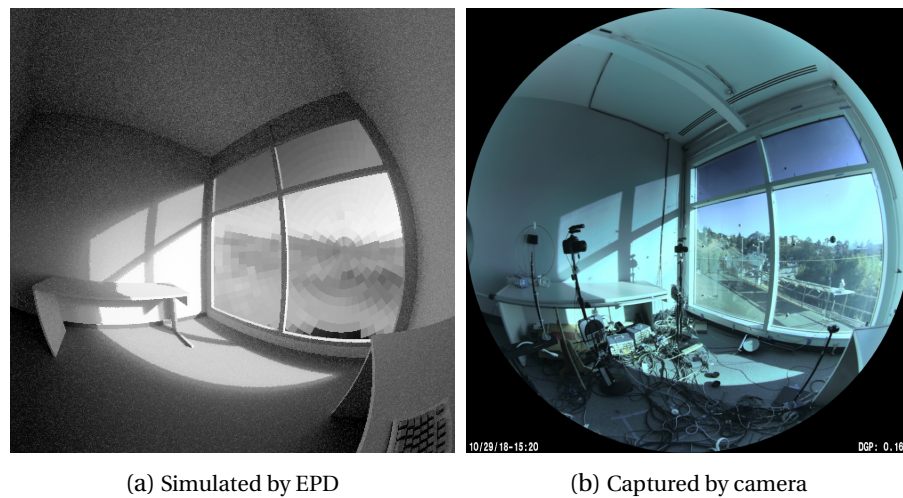


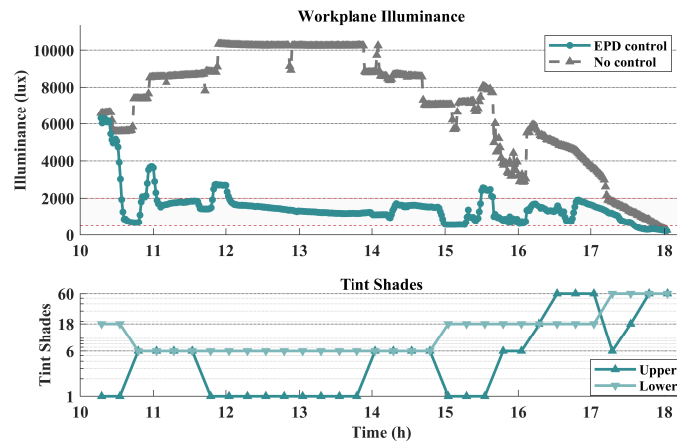
Fig. 6.8. View images with EC glazing at 1% (upper) and 6% (lower) transmittance

6.4.2 EC glazing control

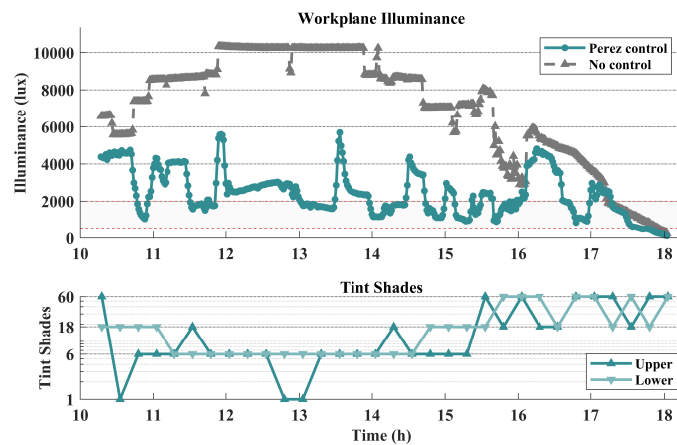
For EC glazing control, the EPD monitored luminance distribution of the sky, simulated interior WPI and DGP at defined positions, and optimized tint states for EC glazing, following the flowchart in Figure 6.5. The EPD evaluated and controlled the EC tint combination of Room C every 15 min, as described in Section 6.3.3. To outline the performance of EPD, weather data (direct normal and diffuse horizontal irradiance) from a weather station at LBNL was used with the same lighting simulation method (matrix algebraic approach) employing the Perez all-weather model, as described in Section 6.3.2, to control the EC glazing simultaneously in Room B, as a conventional control strategy based on weather data. Room A provided uncontrolled daylighting conditions with fixed glazing transmittance (low-emittance window) as reference. To simultaneously evaluate the glazing control performance in the three parallel rooms, lux-meters and cameras were used to monitor WPI and DGP respectively. Experiments were conducted from Oct. 22nd to 28th, 2018, under various sky conditions, including clear, clear with thin clouds, and partly cloudy.

Figure 6.9 shows the result of WPI on Oct. 24th (maximum solar elevation angle 40°) under a clear sky. Sub-figure a) shows the mean horizontal illuminance monitored by six lux-meters as WPI in Room C with its EC glazing controlled by EPD, denoted by green curves in the upper section of Figure 6.9 a). The grey curve represents the WPI monitored by lux-meters in Room A without daylight control by EC glazing as a reference. The lower section in Figure 6.9 a) illustrates the optimized tint states for EC glazing in the upper daylight and lower view sections. Before the EPD started the first evaluation, WPI had exceeded the upper constraint bound (2000 lux). Therefore, the controller switched the EC glazing to 1% transmittance in the upper section and to 18% in the lower section from the initial clear tint state (60% transmittance). The WPI dropped accordingly into the constraint (500~2000 lux, the highlighted region), in which

the computation time of EPD and the response time of EC glazing (10~30 min) contributed to the delay. When the sky luminance surged at 10:40, the EPD further tinted the lower window section to 6%, which lowered the increased WPI below 2000 lux. Throughout the day, the WPI was maintained within the constraint, as the glass tint states were optimized dynamically according to variation in the luminance distribution of the sky. In the evening, when the WPI approached the lower bound (500 lux), the EC glazing was bleached to allow in sufficient daylight. Figure 6.9 b) illustrates the daylighting performance with the EC glazing control in Room B based on real-time weather data of direct normal and diffuse horizontal irradiance and the Perez all-weather model. The green curve in the upper section of the figure shows the WPI monitored by lux-meters in Room B with its EC glazing control based on sky model, while the grey curve represents the same WPI monitored in Room A without daylight control as a reference. Due to the limited accuracy of real-time lighting simulation based on weather data and the Perez sky model [145], the corresponding WPI shows a higher frequency of exceeding the upper limit compared with that controlled by the EPD. The time fraction when WPI remain within the constraint is 83% for the EC glazing control based on the EPD in Room C, while it is 41.2% for the EC glazing control based on weather data and Perez all-weather model in Room B, as compared with 9.0% without daylight control in Room A, under a clear sky.



(a) Control based on EPD



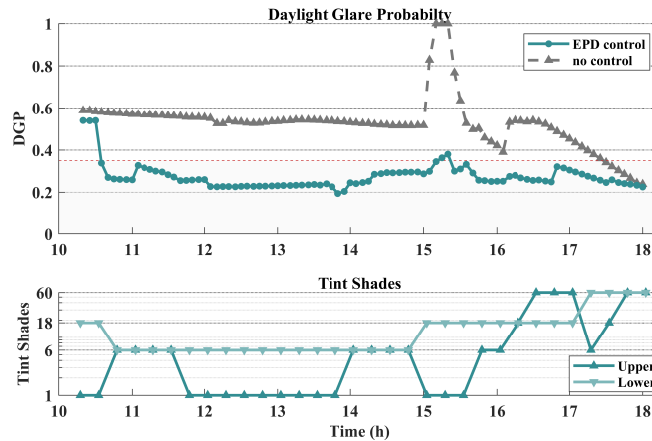
(b) Control based on weather data and Perez sky model

Fig. 6.9. WPI with EC glazing controlled by different method (clear sky)

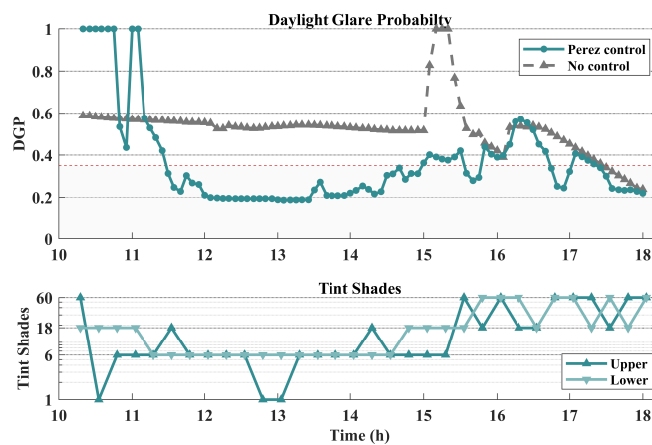
Figure 6.10 a) shows the maximum DGP monitored by the two cameras in room C with EC glazing controlled by the EPD (green curve) on the same day, as compared with that in room A without dynamic EC glazing (grey curve). Since cameras recorded DGP at a five min interval, the data points are sparser than those in Figure 6.9. The DGP was reduced from above intolerable (> 0.59) to imperceptible level (< 0.35) after EPD started to operate. Although the DGP in room A without EC glazing protection exceeded the comfort zone, the DGP in room C with automated EC glazing tints based on EPD control was maintained in the imperceptible glare range, except when it reached a perceptible level ($[0.35, 0.4]$) at 15:10 when the sun was in the FOV of the left camera through the upper window section. Even though the upper daylight window section was tinted to the full tint state (1% transmittance), the DGP still slightly exceeded the imperceptible limit due to the intensive luminance of the sun disk, which is one limitation of regulating the disability glare due to the sun with EC glazing. Figure 6.10 b) presents the DGP monitored by cameras in room B with EC control based on real-time

Chapter 6. Automated electrochromic glazing

weather data and the Perez all-weather model (green curve). The curve shows a relatively high probability of exceeding the comfort range; the frequency of variation of tint states is increased. The time fraction that DGP was maintained within comfort range is 94.6% for the EC glazing control based on the EPD in Room C, while it is 61.2% for the EC glazing control based on weather data and Perez all-weather model in Room B: it can be favourably compared to 7.5% without daylighting control in Room A, under a clear sky.



(a) Control based on EPD

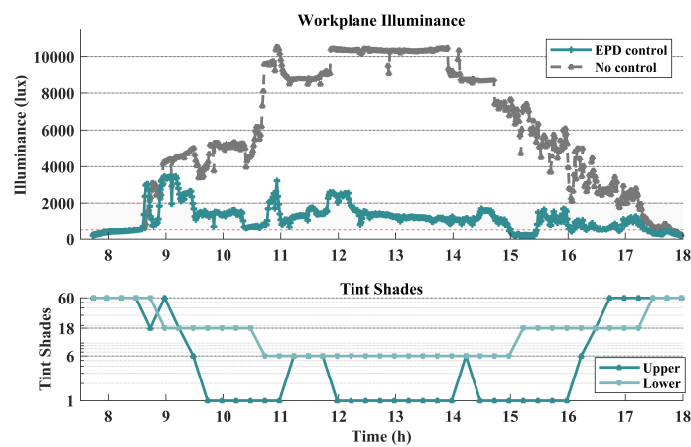


(b) Control based on weather data and Perez sky model

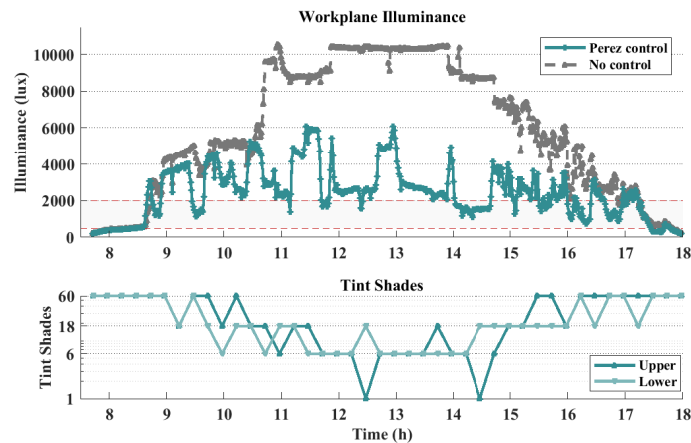
Fig. 6.10. DGP with EC glazing controlled by different methods (clear sky)

Under a clear sky with thin clouds, the motion of clouds contributed to the fluctuation of daylight provision in the building interior on Oct. 27th (maximum solar elevation angle 40°), as the WPI illustrated in Figure 6.11. Sub-figure a) shows the WPI monitored by lux-meters in Room C with EC glazing controlled by the EPD (green curve), compared with that in Room A with a static low-emission window. Although the external daylight condition varied throughout day, the WPI tuned by the EC glazing controlled by the EPD was maintained within the [500, 2000] lux range 70.3% of the time, as compared to 9.7% without EC glazing protection. The

rapid movement of clouds and response delay of both the EPD and EC glazing contributed to the over-suppression of WPI below 500 lux at 15:00. Sub-figure b) presents the WPI monitored by lux-meters in Room B with EC glazing control based on real-time weather data and the Perez all-weather model (green curve). Since a sky model does not resolve cloud pattern distribution in real-time, the daylight provision cannot be simulated accurately based on an assumed smooth sky luminance distribution model; the WPI exceeded the 2000 lux upper limit multiple times; this was possibly a result of underestimated WPI simulation, with 25.8% of the time within constraint. EC tint states controlled by the EPD shows a relatively better stability with less variations than those of EC glazing control based on weather data and sky model.



(a) Control based on EPD



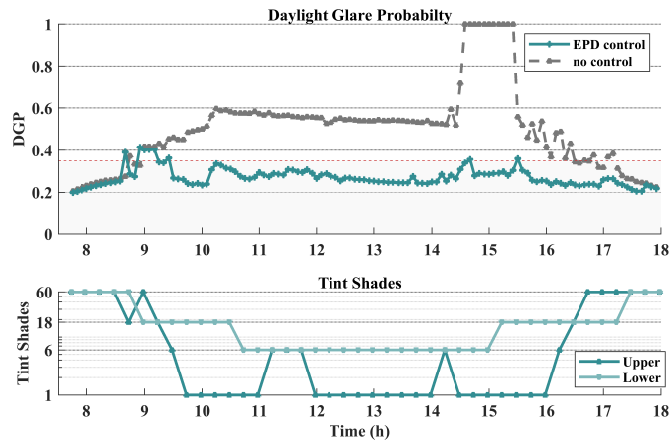
(b) Control based on weather data and Perez sky model

Fig. 6.11. WPI with EC glazing controlled by different methods (thin clouds)

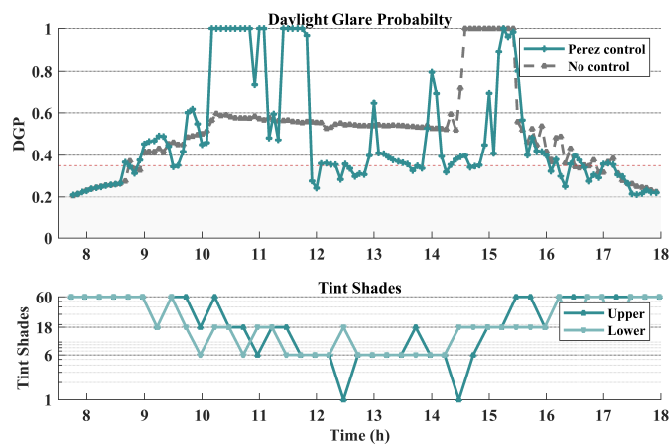
Figure 6.12 a) shows the DGP monitored by cameras in Room C with EC glazing controlled by the EPD (green curve), as compared with that monitored by cameras in Room A without any protection (grey curve). The DGP fluctuated throughout the day due to the movement

Chapter 6. Automated electrochromic glazing

of thin clouds, occluding the sun occasionally. The ratio of DGP within the imperceptible range reached 93.5% with EC glazing controlled by the EPD, while it reached 35.8% with a control based on weather data and sky model as shown in Figure 6.12 b); it can be favourably compared to 22.8% without any protection. The EC glazing control based on the EPD showed a pronounced advantage over the control based on weather data in regulating daylight provision and tempering discomfort glare under a clear sky with thin clouds.



(a) Control based on EPD

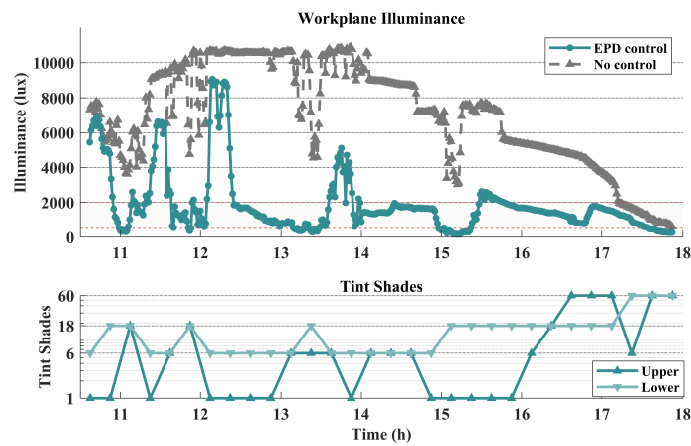


(b) Control based on weather data and Perez sky model

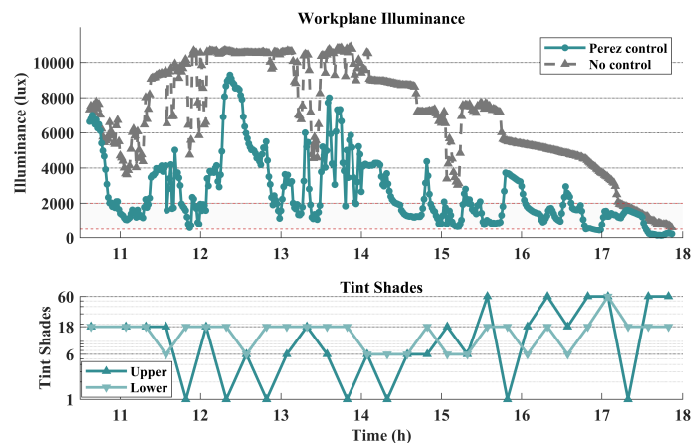
Fig. 6.12. DGP with EC glazing controlled by different methods (thin clouds)

Partly cloudy skies are the most challenging condition for the EC glazing control, since daylight availability varies drastically in both magnitude and frequency due to movement of thick clouds, the performance of EPD being limited by its computation time consumption and delay of EC window response. Figure 6.13 shows the WPI recorded by lux-meters in room C with the EC window controlled by the EPD (green curve) on Oct. 23rd (maximum solar elevation angle 40°) under a partly cloudy sky, as compared to that in Room A with a low-emission window (grey curve). When the EPD started the evaluation and sent a signal to modify EC tint states, the

external daylight decreased sharply in intensity and the WPI was over-suppressed marginally below 500 lux at 11:00 due to the delay of EPD evaluation and EC glazing response. The tint states of EC window at 11:00 were optimized for the daylight condition 20 min before. The overshoot or over-suppression of WPI was also due to the response delay at 11:30, 12:10, 13:30, 13:50, 15:10, and 15:30. Although the rapid motion of clouds deteriorated EPD performance, the EPD outperformed the weather data and sky model based control in regulating WPI as shown in Figure 6.13 b) (green curve), with 63.3% of the time within constraint rather than 49.1% of the time based on weather data and a sky model, as compared to 9.1% without EC glazing protection.



(a) Control based on EPD



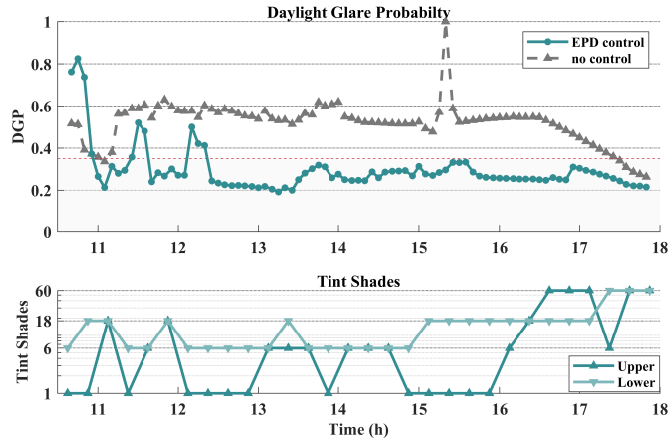
(b) Control based on weather data and Perez sky model

Fig. 6.13. WPI with EC glazing controlled by different methods (partly cloudy)

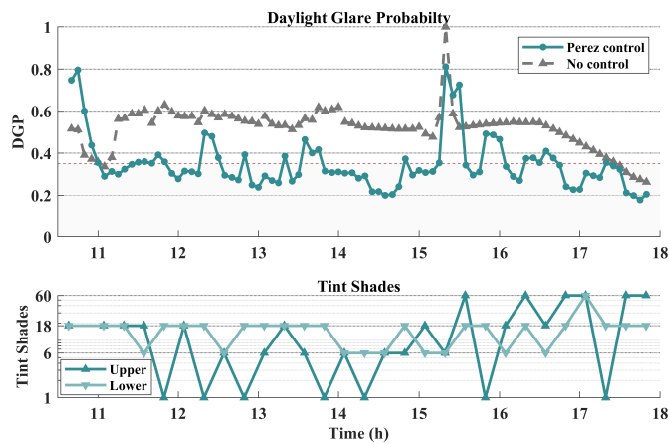
The DGP, monitored by cameras in Room C with EC glazing controlled by the EPD, fluctuated under the partly cloudy sky as shown in Figure 6.14 a) (green curve). With daylight control by the optimized EC tint states based on the EPD, the ratio of DGP within imperceptible level reached 88.5% of the time, while it reached 63.2% of the time with EC glazing control based

Chapter 6. Automated electrochromic glazing

on weather data and a sky model as shown in 6.14 b), as compared to 6.8% in Room A with a low-emission coated glazing.



(a) Control based on EPD



(b) Control based on weather data and Perez sky model

Fig. 6.14. DGP with EC glazing controlled by different methods (partly cloudy)

Table 6.2 summarizes the time fraction that WPI and DGP were maintained within constraint with the window façades controlled by different strategies under various sky conditions for the visual satisfaction of occupants. It can be observed that EPD control achieved the largest ratio of daylight provision (83% on average) and glare risk (95% on average) in constraint range under clear skies when the external daylight condition changed slowly. The EPD controlled EC glazing (68% for WPI, 94% for DGP on average) showed a more favourable behaviour as compared with EC glazing control based on weather data and the Perez all-weather model (28% for WPI, 41% for DGP on average) under clear skies with thin clouds: since the EPD based on sky luminance monitoring was able to resolve the varying cloud patterns achieving enhanced accuracy of real-time daylighting simulation. Although the EPD was limited by its computation time and delay of EC glazing response under partly cloudy skies with rapid

motion of clouds, it was able to dampen the variation of daylight provision and glare risk for occupants. Its performance can be improved by reducing the computation time via advanced hardware or simplified algorithms, and by employing the new EC glazing technology with fast transition period.

Table 6.2 – Ratio of time regarding WPI and DGP within constraints

Date	Sky type	WPI			DGP			Total time (min)
		EPD	Perez	Static	EPD	Perez	Static	
10/22	Clear Sky	84.5%	53.8%	9.0%	98.7%	81.3%	6.7%	435
10/24	Clear Sky	83%	41.2%	9.0%	94.6%	61.2%	7.5%	465
10/25	Clear Sky	80.5%	36.2%	6.6%	93.1%	63.2%	3.4%	435
10/26	Clear/thin clouds	66.1%	29.4%	6.9%	95.4%	47.1%	9.2%	435
10/27	Clear/thin clouds	70.3%	25.8%	9.7%	93.5%	35.8%	22.8%	615
10/23	Partly Cloudy	63.3%	49.1%	9.1%	88.5%	63.2%	6.8%	435
10/28	Partly cloudy	61.2%	42.3%	15.9%	81.8%	40.5%	28.6%	630

Note: the constraint of WPI is [500, 2000] lux, that of DGP is ≤ 0.35 , according to Equation (6.2)

6.5 Discussion

In this chapter, EPD performance on the DGP simulation was compared with DSLR cameras based on captured HDR images in Section 6.4.1. Although DSLR cameras with high-quality fish-eye lens have been widely used by researchers to quantify discomfort glare, cameras commonly require a relatively long exposure time (commonly approximately 30 s) to achieve a wide luminance detection range and a low-transmittance neutral density (ND) filter to attenuate solar luminance due to its limitation of shutter speed when the sun is in FOV. Researchers also depend on the linear transformation of color space to generate luminance values from captured images, the spectral response mismatch with the photopic luminosity function $V(\lambda)$ being commonly unidentified. With spectral correction by optical filters, the EPD has a close spectral response to the $V(\lambda)$ ($f'_1 = 8.89\%$) in monitoring sky luminance distribution. Its high-speed shutter makes the exposure time relatively short (in 0.5 s), with dynamic range of 150 dB for luminance detection, which is advantageous in capturing fast-moving clouds regarding effects of motion blur. Moreover, a single EPD is able to simulate DGP values at multiple defined positions and view directions simultaneously, while multiple cameras must be used to accomplish the task using captured images despite their actual positions. In EC glazing or shading control, it is impractical to place multiple DSLR cameras at occupants' view positions, due to privacy issues and occupants' random motions occluding the FOV of DSLR cameras.

In EC window control, the EPD operates at 15 min intervals to change tint states of EC glass continually according to dynamic sky conditions under a partly cloudy sky. When the sky varies more rapidly than the evaluation frequency of EPD, the EPD can miss the sky's instantaneous

variation, or delayed response of EPD together with that of the EC glass can contribute to overshooting or over-suppression of WPI and DGP. Figure 6.15, captured by a DSLR camera in Room A, illustrates the overshooting of WPI at local time (LT) 12:10 in Figure 6.13 on Oct. 23rd. As highlighted in Figure 6.15 a), a cloud was on the right side of the window, 2 min before the EPD evaluation at LT 11:52. After evaluation (3 min later), the cloud moved to the left side of the window, as highlighted in Figure 6.15 b). In fact, the cloud occluded the sun when EPD evaluated the sky conditions at LT 11:52. Therefore, the resulting low daylight availability, at that moment, caused the EPD to increase the transmittance of the EC glazing to 18% for both window sections. After 15 min, when the tint states reached 18% transmittance and the cloud moved away, the excessive daylight injection contributed to the overshoot of WPI at LT 12:10 in Figure 6.13. To resolve the uncommonly fast moving clouds, advanced hardware can be applied to enhance the computation speed of EPD if the cost is acceptable to users. Alternatively, employing simplified algorithms can also increase EPD's evaluation frequency despite sacrificing simulation accuracy.

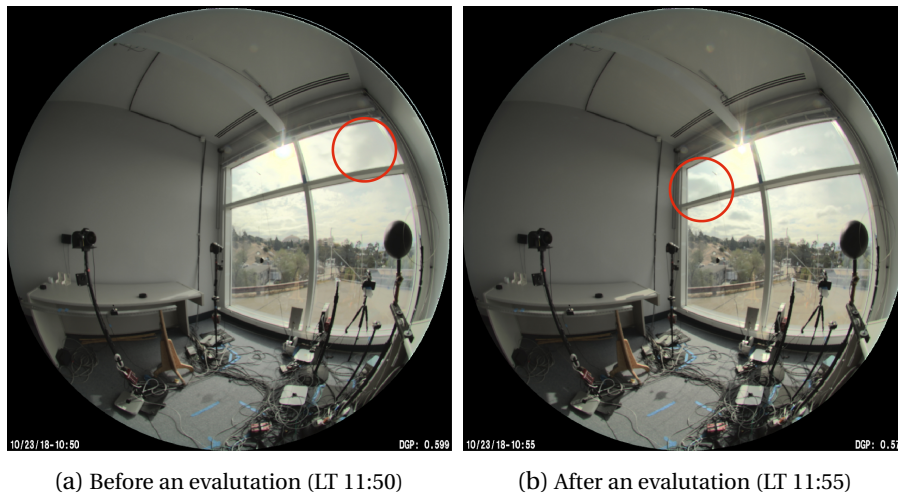


Fig. 6.15. Rapid motion of clouds (captured in Room A)

6.6 Conclusion

The integration of EC glazings with an efficient tint control system is a major challenge for the broad application of EC glass. This chapter presents a highly integrated design of a stand-alone EC glazing control system to improve visual comfort for occupants. An EPD, which acts both as a sensing unit and a controller, can monitor the luminance distribution of the sky and landscape and perform real-time lighting simulation of building interior. Based on simulated results, tint states of a split-pane EC glazing are optimized to maintain sufficient work-plane illuminance, to prevent excessive solar heat gain, and to mitigate discomfort glare of occupants, which answers the fourth research question of the thesis in Section 2.6.

A cross comparison was performed to demonstrate the lighting simulation capability of EPD in WPI, image rendering, and DGP calculation, with lux-meters and calibrated cameras. Based on a matrix algebraic approach, the EPD was able to assess WPI and DGP in the building interior for 16 tint combinations of a split-pane EC window and to optimize EC glass tint to achieve visual comfort within 8-10 min. 'In-situ' experiments of split-pane EC glass control were carried out in a daylighting testbed under various sky conditions. Three parallel office rooms illustrated daylight conditions by EC glazing with EPD control, with conventional weather data and sky model control, and without control (clear glazing) respectively. The results showed that the WPI was within the confined range ($WPI \in [500, 2000]$ lux) 83% of the working time and the DGP within comfort range ($DGP \leq 0.35$) 95% of the time with daylight regulated by the automated EC glass based on the EPD under clear skies; under clear skies with thin clouds, the WPI was within confined range during 68% of the time and the DGP during 94% of the time. Although the computation time of EPD and response delay of EC glass limited the performance of daylighting control under partly cloudy skies, the EPD controlled EC glazing was able to dampen the WPI and DGP variation when daylight condition varies rapidly, during 62% and 85% of the time constrained in comfort range respectively. The split-pane EC window controlled by the EPD was superior at reaching visual comfort as compared to conventional EC glazing control based on weather data and sky models.

Furthermore, the EC control system also features merits in installation convenience, since the integrated design avoids installation of separate sensors and wiring issues in the building interior. As a decentralized system, the designed EC control system is independent of weather data or weather stations which commonly require the access to a non-shadowing roof. Additionally, pre-knowledge of window position and direction is not required since a relative coordinate is established in the EPD controller. Moreover, veiling glare due to secondary reflection on specular surfaces from surroundings can be protected, since the EPD monitors the luminance distribution of the exterior space.

Investigation on the application of the integrated EC control system in open-planned offices will be conducted in the future. Improvement in the response delay of EPD will be studied by employing simplified algorithms and advanced computation hardware and by using faster responding EC glazing.

7 Conclusion

The main objective of this thesis is to deliver a daylighting control system for non-residential buildings to foster daylighting in buildings from an energy saving perspective and to secure occupants' visual satisfaction from a productivity and visual comfort perspective, especially in highly glazed buildings equipped with solar protection or EC glazing. To cope with dynamic and complex sky conditions, an embedded photometric device (EPD) was designed and validated for real-time lighting computing based on sky luminance monitoring. The EPD was then used both as a sensor and a controller to manage the position of Venetian blinds and tint states of EC glazings according to the sky variations, as an integrated decentralized system. 'In-situ' experiments demonstrated the performance of this automated daylighting system in offering sufficient daylight provision, mitigating excessive solar heat gain, tempering discomfort glare for occupants, and simultaneously offering optimal views outwards. The main achievements of the thesis are summarised in Section 7.1. Section 7.2 discusses the merits and limitations of the daylighting control system from the perspective of application and practical use. Section 7.3 outlines potential improvement to be made in future work.

7.1 Main achievements

7.1.1 Embedded photometric device

In order to overcome the limitation of standard sky models in resolving local climate at a short time scale for lighting simulation, an EPD was designed and validated regarding real-time lighting computing based on the luminance distribution monitoring of the sky and landscape. The EPD is composed of a low-cost image sensor and a field programmable gate array (FPGA) processor, which is able to map the outdoor luminance distribution with 1.2×10^6 patches. After an 'ad hoc' calibration, the spectral response of the imaging system is close to the photopic luminosity function $V(\lambda)$, with a spectral correction error f'_1 achieving 8.9%. Within 1.3 s acquisition time, the EPD can span a luminance detection range of $1.2 \times 10^2 \sim 3.78 \times 10^9$ cd/m² (150 dB), with two extremes covering the luminance of shadowing landscape during daytime and that of the sun orb (maximum 1.6×10^9 cd/m²). Therefore, the EPD is able to monitor the

Chapter 7. Conclusion

luminance distribution of the sky vault and the ground fraction simultaneously, including the sun, the sky background, clouds, and surrounding landscape during daytime, and thus avoids the difficulty of modelling surrounding buildings and vegetation in daylighting simulation.

The EPD demonstrated its lighting simulation accuracy of image rendering as well as for the work-plane illuminance distribution, compared with a common practice employing the Perez all-weather model. In a daylighting test module (DEMONA), the simulated work-plane illuminance was cross validated with a lux-meter array ($\pm 2\%$ accuracy) at multiple distances to the façade under different hybrid sky types, with a mismatch below 10%, compared to a 20% ~ 40% mismatch when using the Perez all-weather model and real-time weather data. Its performance in tracking solar luminance and sun elevation and azimuth angle was also cross validated with a pyranometer and the reference NOAA data, with a mismatch below 10%. Although it is not practical to replace sky models with the EPD in annual daylighting simulation, the EPD will see its merits in applications requiring real-time lighting computation, including shading and lighting control.

7.1.2 BTDF compression

The BTDF is commonly applied in lighting computing to represent a CFS without the pre-knowledge of material property and physical structure. However, for daylighting simulation in visual comfort studies, the BTDF implies bulky data which challenges transmission and storage on compact computing platforms. A compression scheme based on planar wavelet transforms was used to overcome the limitations of the conventional compression method, including compression ratio and restrictions on angular bases. Trading off between BTDF fidelity and data volume, the compression scheme was investigated on compressing medium-resolution BTDFs (145×1297) of five paradigmatic CFS samples at various compression ratios. The performance was evaluated in regards to intrinsic (generic) errors (RMSE of compressed data) and contributed mismatch in daylighting simulation based on the Perez all-weather sky model. According to the results, the WPI and DGP are not influenced for a compression ratios below 100, while the uniformity factor g_1 is relatively sensitive to BTDF compression. The compression on a high-resolution BTDF data set (2305×2305) of an external Venetian blind was also considered in WPI simulation based on monitored luminance distribution of the sky by the EPD, achieving an unnoticeable error (below 3%) for BTDF compression ratio below 100. Although only BTDF data was investigated, the compression scheme is also potentially applicable on daylighting matrices when the 5-phase matrix algebraic approach is used in lighting simulation, to further reduce data storage load on compact computing platforms.

7.1.3 Automated Venetian blinds

In order to use daylight in a more intensive way and improve the visual satisfaction of occupants in office buildings under dynamic sky conditions, a highly integrated automated

Venetian blind was designed employing the EPD both as a sensing unit and a processor in blinds position control. The compact decentralized system avoids privacy issues (of cameras imaging the building interior) and reduces installation issues (no separate sensors or wiring in the building interior) as well as commissioning difficulties. The shading control is based on real-time daylighting simulations of the EPD with the monitored luminance distribution of the sky (and landscape) and a geometric model of the building interior. The matrix algebraic approach was employed to accelerate the computation of each iterative process of shading control evaluation. According to the simulation results, the EPD determines an optimal shading position to secure sufficient WPI, to mitigate excessive solar heat gain (SHG) in buildings, to temper discomfort glare to an imperceptible level, and to maximize occupants' outside views.

'In-situ' experiments were conducted in a daylighting test module with a unilateral façade on the EPFL campus in Lausanne, Switzerland during summer, autumn, and winter under various sky conditions. The monitoring data showed that the WPI was maintained within the confined range [500,2000] lux during 96% of working time under clear skies and during between 79% and 88% of working time under partly cloudy skies, with moderated discomfort glare. The related mitigation of cooling loads due to excessive solar heat gain (SHG) was estimated to reach 47% in warm periods. The shading system was also demonstrated to successfully block a veiling glare source due to sunlight occurring on a specular mirror located in front of the façade and reopens the shading timely after the glare source was removed. A survey study with 34 subjects experiencing the automated shading system showed users' satisfaction with daylight provision, glare protection, and quiet motion of slats in adjustment. A sensibility analysis of the interior surface reflectances illustrates the commissioning improvement, the automated system being not sensitive to the exact reflectance value of each surface material, as long as the overall reflectance of walls and ceilings does not have a pronounced mismatch with reality.

7.1.4 Automated EC glazing

The EPD was also integrated with a split-pane electrochromic (EC) glazing to handle its tint states according to the varying sky conditions. The control of tint states is based on real-time lighting computation based on the monitored luminance distribution of the sky (and landscape) and a geometric model of the building interior. It controls tint combinations of the upper daylighting section of the EC window and the lower view section simultaneously, optimizing the daylight ingress to offer sufficient daylight provision, mitigate excessive solar heat gain, and temper discomfort glare for occupants, while preserving their outwards view quality.

The daylighting performance of the EC window was demonstrated in a full-scale testbed at Lawrence Berkeley National Laboratory, Berkeley, CA. For performance assessment, a lux-meter array and calibrated DSLR cameras were positioned in the testbed to monitor WPI and

DGP respectively as reference values. Experimental results showed that the WPI was within the confined range ($WPI \in [500, 2000]$ lux) 83% of the working time and the DGP within comfort range ($DGP \leq 0.35$) 95% of the time with daylighting regulated by the automated EC glazing based on the EPD under clear skies; under clear skies with thin clouds, the WPI was within confined range during 68% of the time and the DGP during 94% of the time; finally, under partly cloudy skies, the WPI was within confined range during 62% of the time and the DGP during 85% of the time. The performance of the EC window was also compared with that of an EC window using a conventional control approach based on the Perez all-weather model and weather data, contrasting the advantage of EPD control. The EPD controlled EC glass showed pronounced advantage in regulating daylight as compared to the control based on weather data and the Perez all-weather model under clear skies with thin clouds, since the EPD based on sky luminance monitoring was able to resolve the varying cloud patterns achieving enhanced accuracy of real-time daylighting simulation. Since the response of EC glazing tint was not instant, the limitation of the EC glass delay together with time consumption in lighting computation on EPD are discussed with regard to the performance under partly cloudy skies with rapid motion of clouds.

7.2 Perspectives of application

The compact daylighting control system features multiple advantages for application in buildings. Since all the components are integrated into a shading system or on EC glazing, including the sensing unit, the micro-processor, and driver of the actuator, the stand-alone system allows for plug and play operation and avoids the installation complexity of sensors and connection wires placed indoors, preserving the building interior from an aesthetic perspective. In addition, it avoids the privacy issue of using cameras to monitor the building interior, since the EPD imaging system points at outdoor space. Thanks to the relative coordinates established on the imaging system, pre-knowledge of location and window orientation is not required, reducing commissioning complexity. As a decentralized system, the automated shading device is not restricted by the availability of weather data or weather station, since office owners commonly have limited access to a non-shadowing roof or a weather station nearby. Moreover, since the controller monitors outdoor conditions, the shading reopens timely after a glare source disappears, enhancing the utilization of daylight in buildings. The automated daylighting system is ideal for applications in highly glazed buildings which are sensitive to glare, since the system shows merits of moderating discomfort glare both from the direct sunlight and potentially from secondary reflections in surroundings, including opposite glazed buildings or windscreens of parked vehicles. The control of shading is based on real-time daylighting simulations, which calculates the glare risk due to inter-reflection between slats of Venetian blinds. The novel method of shading control avoids the slats oscillation of commonly used closed-loop control systems based on ceiling mounted sensors. Last but not least, the improved actuator of a DC step motor is able to adjust inclined slats of Venetian blinds precisely with quiet and smooth motion, which reduces disturbance to occupants.

The original design of the daylighting system implies the integration of a single EPD in each shading device or EC window. For application in open-planned offices, multiple shadings or EC windows are commonly used on each façade. In this case, multiple shading devices or EC windows can share one EPD controller, as long as they are oriented in the same direction, which saves hardware cost. If cost is not an issue, maintaining the density of one EPD controller for each shading device or EC window can secure the performance in tempering discomfort glare especially from secondary reflections on specular surfaces in surroundings, since the denser the EPD controller the higher chance that it detects a glare source with a relatively small solid angle from the sampling perspective, which reduces the parallax error. Moreover, the EPD controller can not only be applied to control Venetian blinds and EC windows but also to control other operable shading devices, including roller blinds and shutters. Therefore, the research questions of the thesis raised in Section 2.6 have been addressed.

7.3 Future outlook

Although the daylighting control system performs well under the majority of sky conditions, the computation time (8-10 min) still limits its performance under partly cloudy skies with rapid motion of clouds, that can occlude the sun and move away in 5 min. Therefore, the acceleration of computation will be studied in the future either by employing advanced computing hardware or by improving algorithms in lighting computation. In addition, the trade-off between simulation accuracy and response speed will be studied.

In this thesis, the shading or EC window control system was not integrated with the user override functionality. Due to the nature of humans' variability in preference and sensitivity to light, a user interaction feature must be developed on the shading controller. Furthermore, an adaptive control algorithm will be studied for shading control according to occupants' preference to enhance user acceptance.

A Appendix A

A.1 Plans of the daylighting test module (DEMONA)

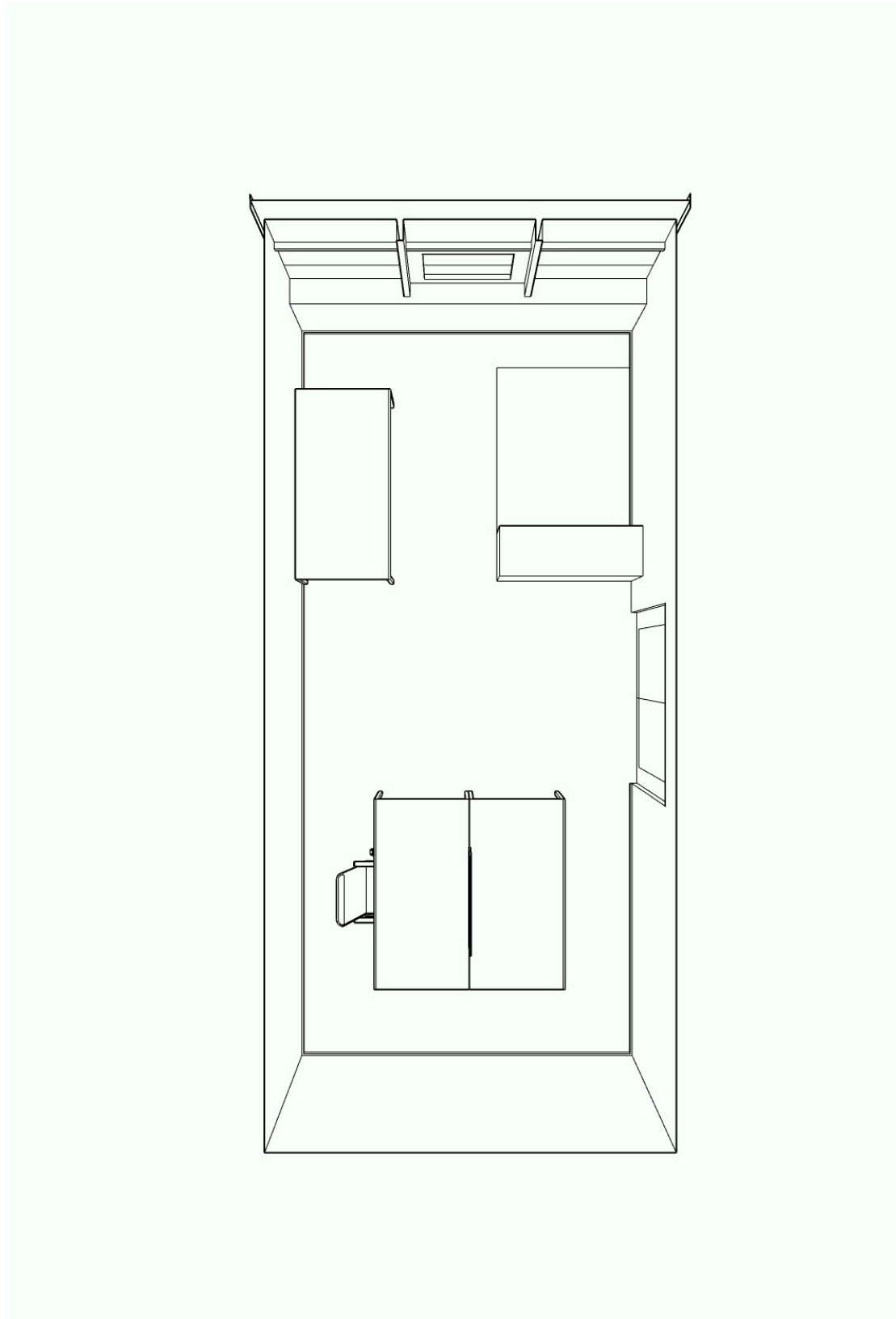


Fig. A.1. Floor plans of the daylighting test module (DEMONA)

A.2 Questionnaire on visual satisfaction

Gender: M/F

Date: __/__/__ M/A

__/3

Survey on Visual Comfort

L/R

1) I like the **lighting** in this room:

No 1-----2-----3-----4-----5 **Yes**

2) Generally, the **lighting** in this room is comfortable:

No 1-----2-----3-----4-----5 **Yes**

3) There is **too much** light for proper reading/writing/typing (on the desk):

No 1-----2-----3-----4-----5 **Yes**

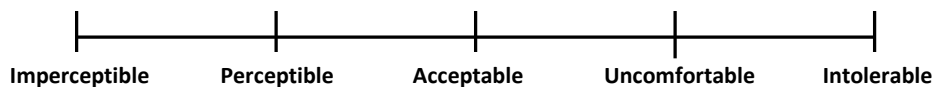
4) There is **not enough** light for proper reading/writing/typing (on the desk):

No 1-----2-----3-----4-----5 **Yes**

5) The light is **poorly distributed** on the work-plane (desk):

No 1-----2-----3-----4-----5 **Yes**

6) I had the **glare** feeling in the room:



7) Did the automated shading **blocked** the **glare** source successfully:

No 1-----2-----3-----4-----5 **Yes**

8) Did the shading **respond** quick enough according to variation of weather condition:

No 1-----2-----3-----4-----5 **Yes**

9) Did the movement of shading slats generate distracting **noise** for you:

Imperceptible 1-----2-----3-----4-----5 **Intolerable**

10) Did the automated shading properly secure your **view** outside, while providing optimal daylight:

No 1-----2-----3-----4-----5 **Yes**

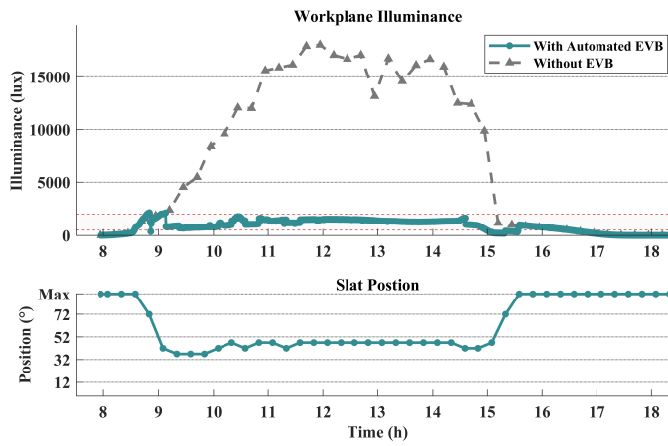
Comments/Suggestions:

Sky type: C / Tn / Tk / O

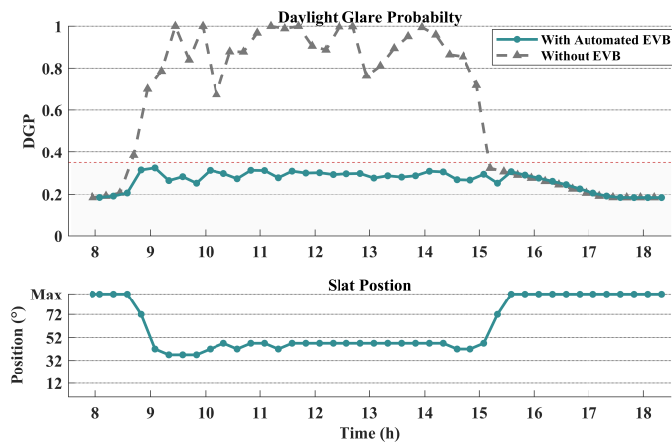
B Appendix B

B.1 Daylighting regulation by the automated EVB

B.1.1 Clear sky



(a) Workplane illuminance (WPI)

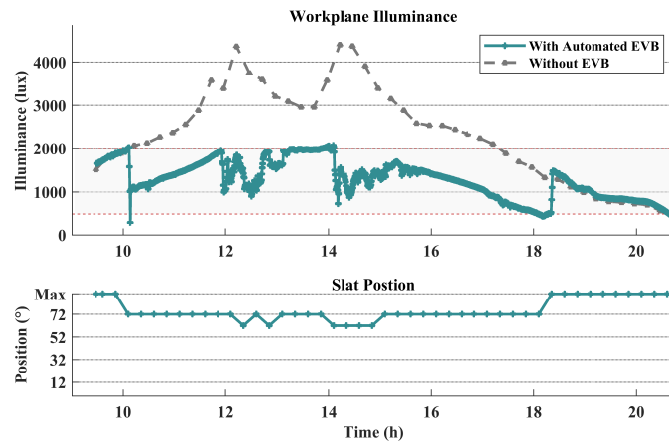


(b) Daylight glare probability (DGP)

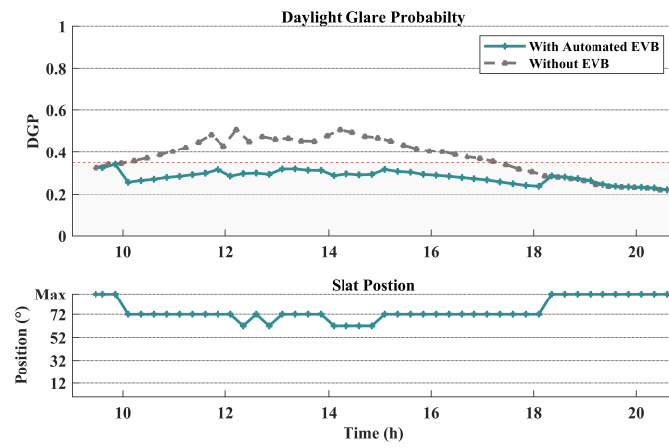
Fig. B.1. WPI and DGP with/without automated EVB on Jan. 15, 2019 (winter, clear sky)

B.1.2 Partly cloudy/clear sky

B.1. Daylighting regulation by the automated EVB

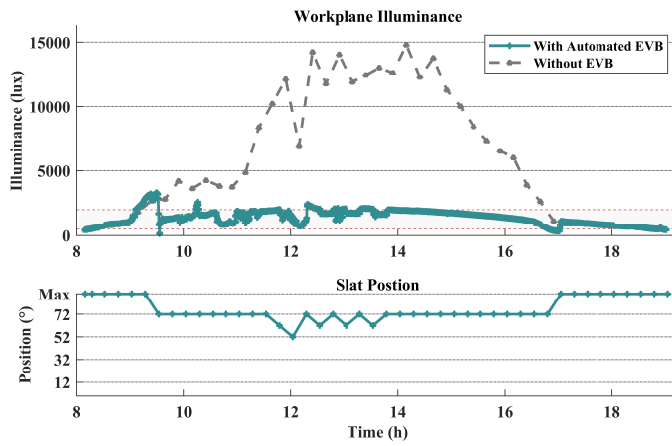


(a) Workplane illuminance (WPI)

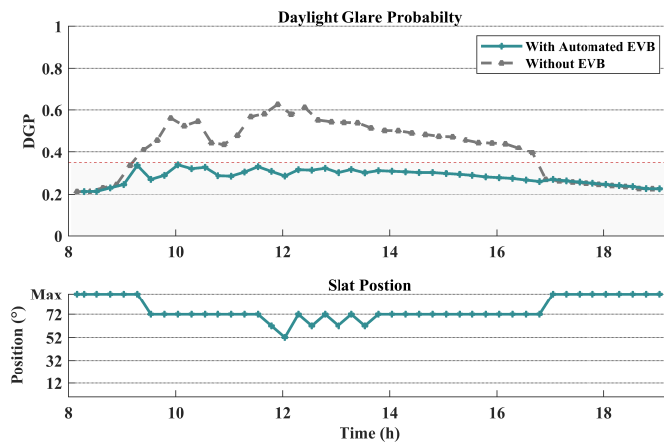


(b) Daylight glare probability (DGP)

Fig. B.2. WPI and DGP with/without automated EVB on Jul. 12, 2018 (summer, partly cloudy/clear sky)



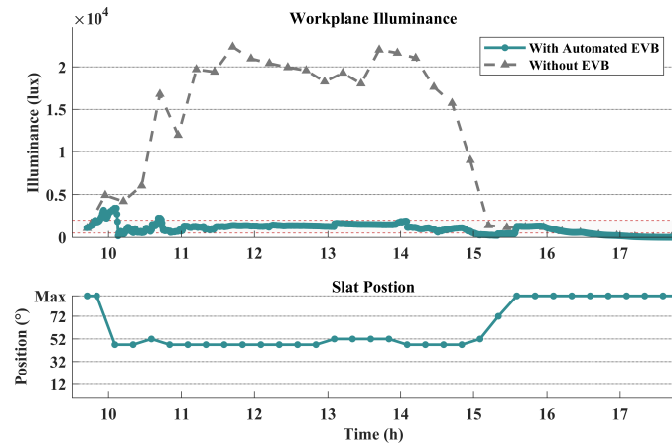
(a) Workplane illuminance (WPI)



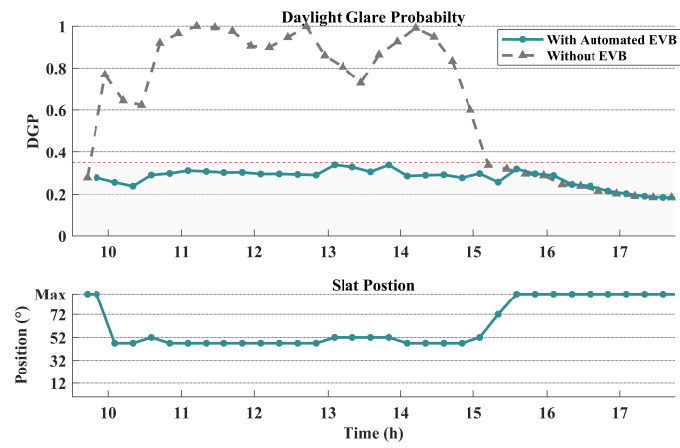
(b) Daylight glare probability (DGP)

Fig. B.3. WPI and DGP with/without automated EVB on Sept. 07, 2018 (autumn, partly cloudy/clear sky)

B.1. Daylighting regulation by the automated EVB



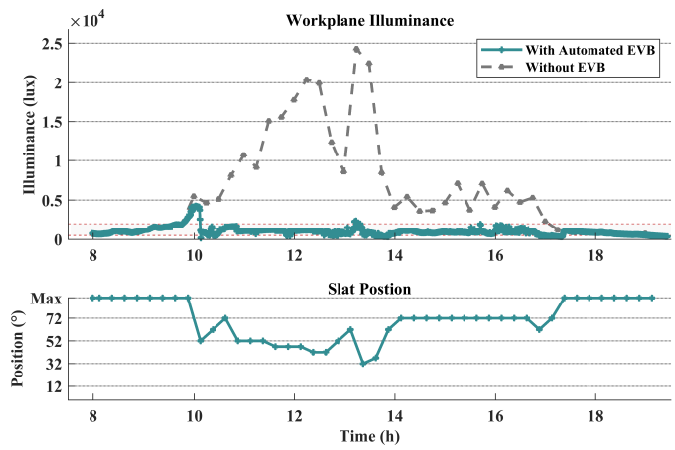
(a) Workplane illuminance (WPI)



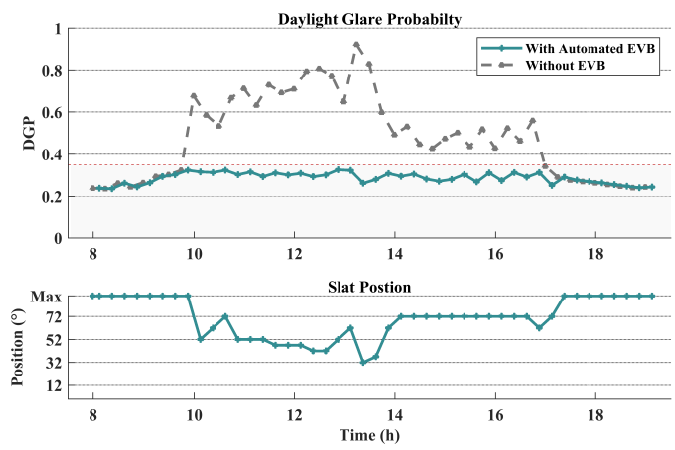
(b) Daylight glare probability (DGP)

Fig. B.4. WPI and DGP with/without automated EVB on Jan. 19, 2019 (winter, partly cloudy/clear sky)

B.1.3 Partly cloudy/overcast sky



(a) Workplane illuminance (WPI)

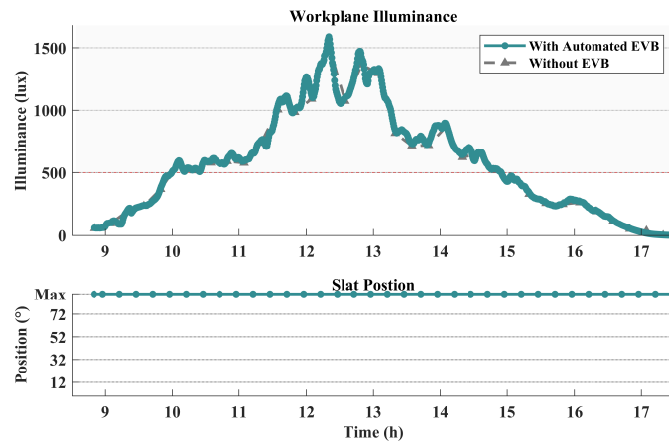


(b) Daylight glare probability (DGP)

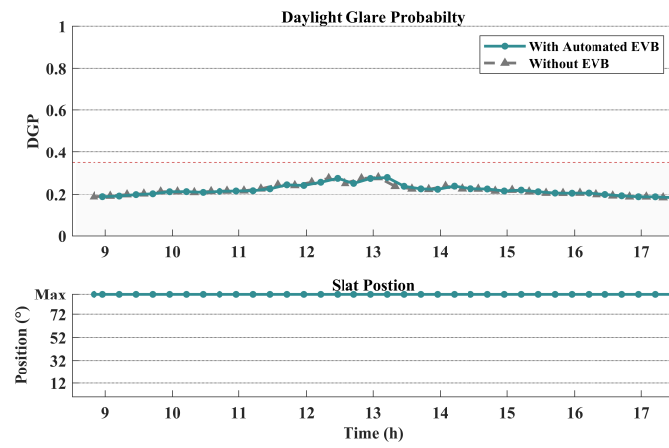
Fig. B.5. WPI and DGP with/without automated EVB on Sept. 03, 2019 (autumn, partly cloudy/overcast sky)

B.1.4 Overcast

B.1. Daylighting regulation by the automated EVB

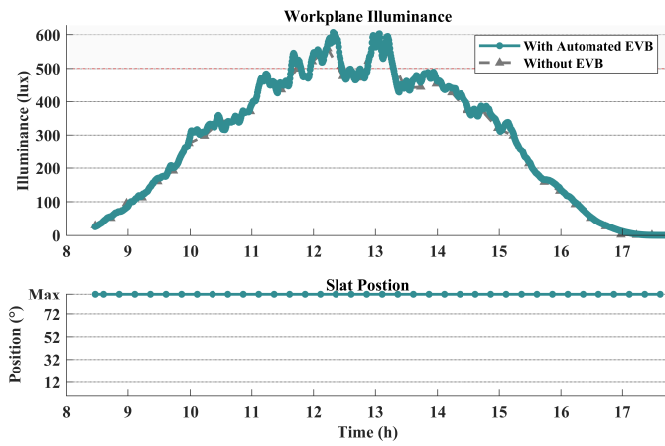


(a) Workplane illuminance (WPI)

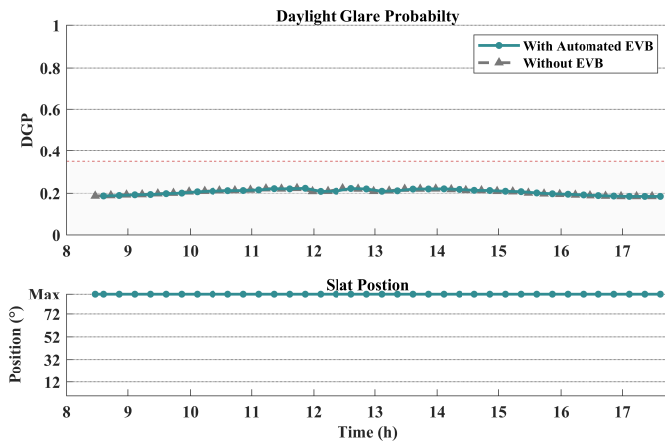


(b) Daylight glare probability (DGP)

Fig. B.6. WPI and DGP with/without automated EVB on Jan. 06, 2019 (winter, overcast sky)



(a) Workplane illuminance (WPI)

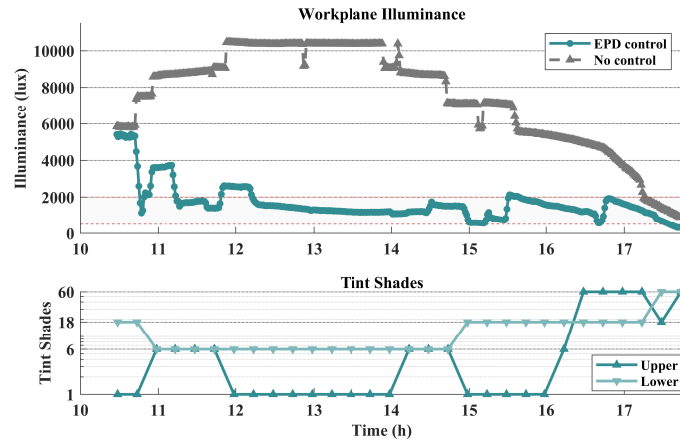


(b) Daylight glare probability (DGP)

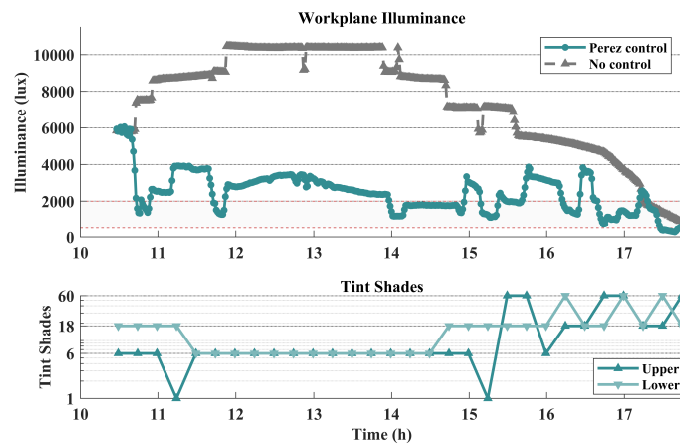
Fig. B.7. WPI and DGP with/without automated EVB on Jan. 07, 2019 (winter, overcast sky)

B.2 Daylighting regulation by the automated EC glazing

B.2.1 Clear sky

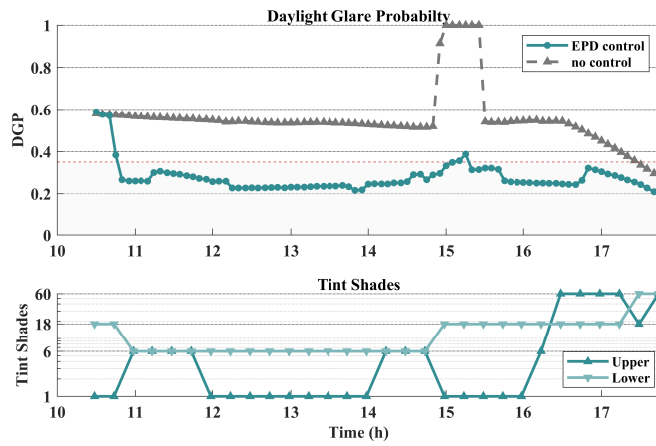


(a) Control based on EPD

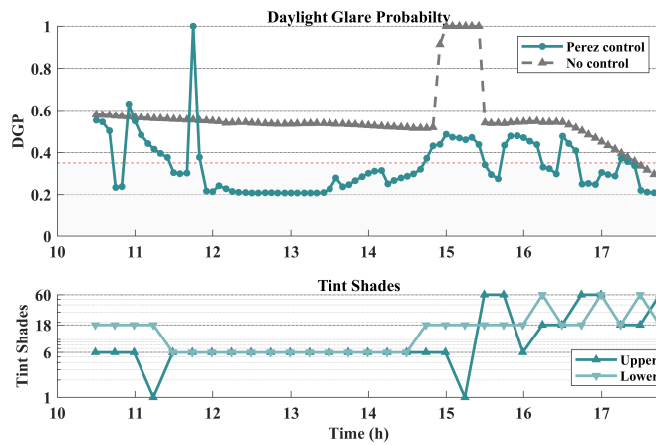


(b) Control based on weather data and Perez sky model

Fig. B.8. WPI with EC glazing controlled by different method on Oct. 25, 2018 (clear sky)



(a) Control based on EPD

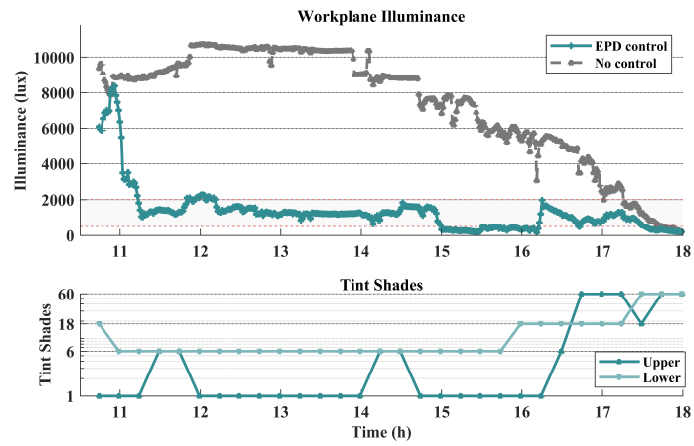


(b) Control based on weather data and Perez sky model

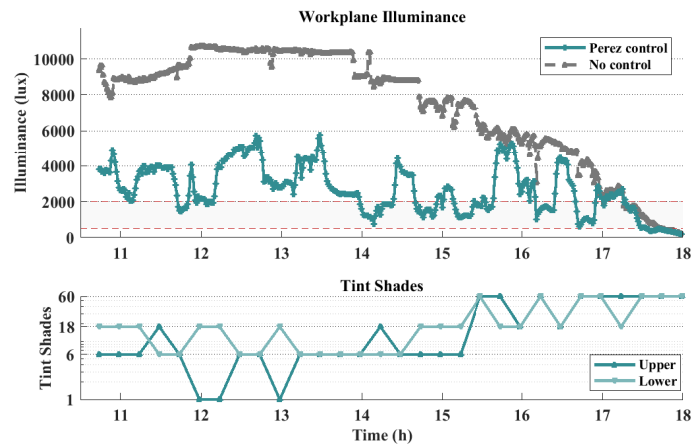
Fig. B.9. DGP with EC glazing controlled by different methods on Oct. 25, 2018 (clear sky)

B.2.2 Partly cloudy/clear sky

B.2. Daylighting regulation by the automated EC glazing

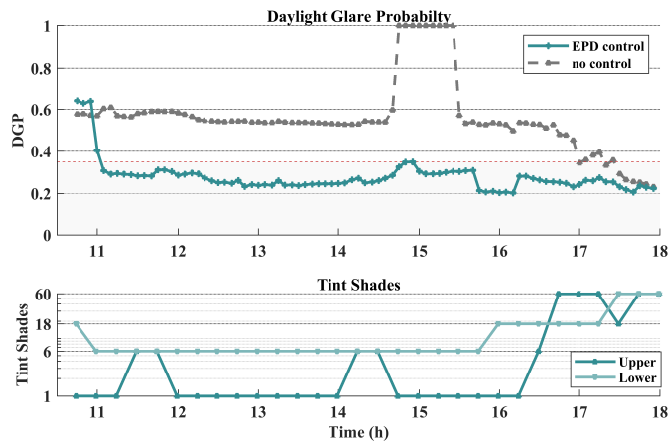


(a) Control based on EPD

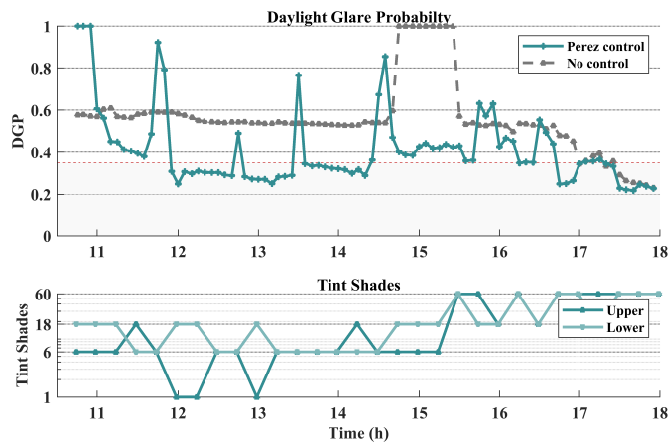


(b) Control based on weather data and Perez sky model

Fig. B.10. WPI with EC glazing controlled by different method on Oct. 26, 2018 (Partly cloudy/clear sky)



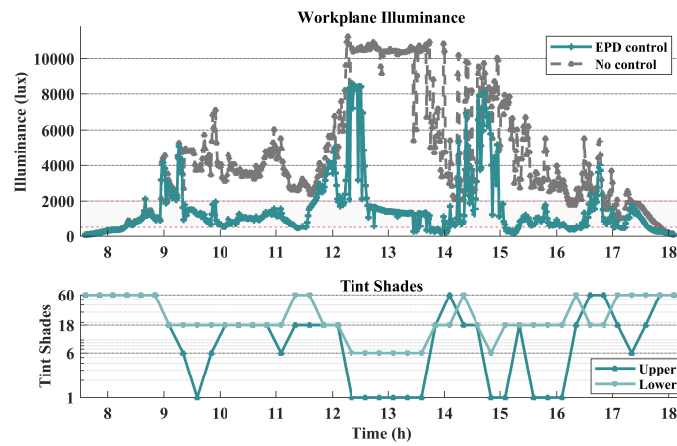
(a) Control based on EPD



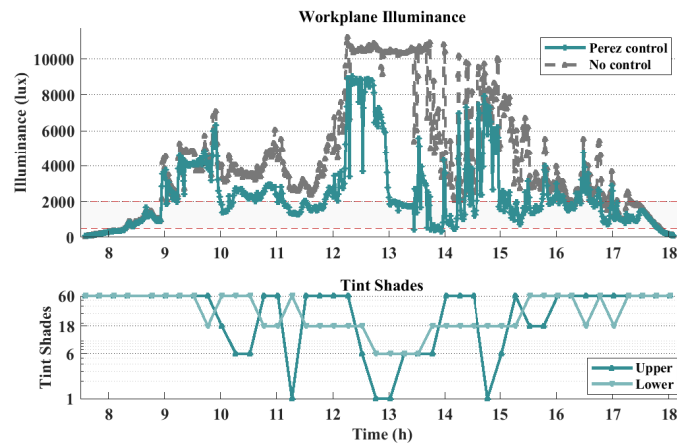
(b) Control based on weather data and Perez model

Fig. B.11. DGP with EC glazing controlled by different methods on Oct. 26, 2018 (Partly cloudy/clear sky)

B.2.3 Partly cloudy/overcast sky

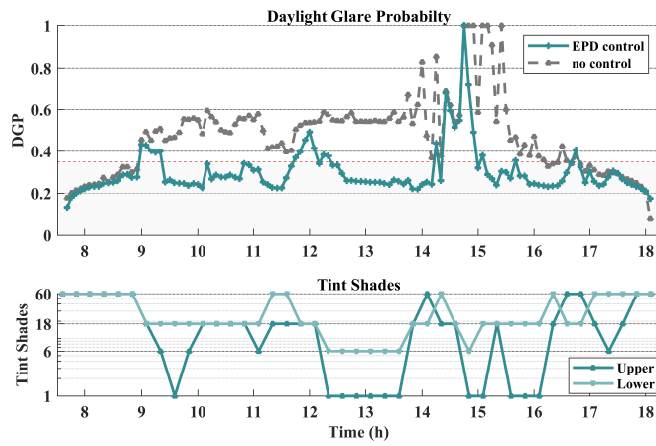


(a) Control based on EPD

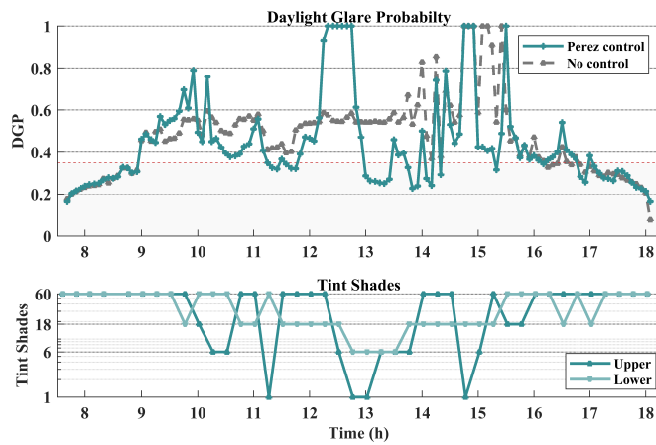


(b) Control based on weather data and Perez sky model

Fig. B.12. WPI with EC glazing controlled by different method on Oct. 28, 2018 (Partly cloudy/overcast sky)



(a) Control based on EPD



(b) Control based on weather data and Perez sky model

Fig. B.13. DGP with EC glazing controlled by different methods on Oct. 28, 2018 (Partly cloudy/overcast sky)

References

- [1] Sage Glass [Digital image], “Retrieved from <https://www.sageglass.com/de/produkte/sageglass>,” 2019.
- [2] E. Lee, D. DiBartolomeo, and S. Selkowitz, “The effect of venetian blinds on daylight photoelectric control performance,” *Journal of the Illuminating Engineering Society*, vol. 28, no. 1, pp. 3–23, 1999.
- [3] Y. Wu, J. H. Kämpf, and J.-L. Scartezzini, “Characterization of a quasi-real-time lighting computing system based on hdr imaging,” *Energy Procedia*, vol. 122, pp. 649–654, 2017.
- [4] E. H. Borgstein and R. Lamberts, “Developing energy consumption benchmarks for buildings: Bank branches in brazil,” *Energy and Buildings*, vol. 82, no. Supplement C, pp. 82 – 91, 2014.
- [5] M. Levine, D. Fridley, H. Lu, and C. Fino-Chen, “Key china energy statistics 2011,” tech. rep., Lawrence Berkeley National Lab.(LBNL), Berkeley, CA (United States), 2012.
- [6] A. Reinders, J. C. Diehl, and H. Brezet, eds., *The Power of Design: Product Innovation in Sustainable Energy Technologies*. West Sussex, UK: John Wiley Sons, November 2012.
- [7] L. Halonen, E. Tetri, and P. Bhusal, eds., *Guidebook on Energy Efficient Electric Lighting for Buildings*. Espoo, Finland: Aalto University School of Science and Technology, 2010.
- [8] E. R. Masanet, *Energy Technology Perspectives 2017: Catalysing Energy Technology Transformations*. OECD, 2017.
- [9] “An assessment of energy technologies and research opportunities,” quadrennial technology review, Department of Energy, USA, Sept 2015.
- [10] M. A. ul Haq, M. Y. Hassan, H. Abdullah, H. A. Rahman, M. P. Abdullah, F. Hussin, and D. M. Said, “A review on lighting control technologies in commercial buildings, their performance and affecting factors,” *Renewable and Sustainable Energy Reviews*, vol. 33, no. Supplement C, pp. 268 – 279, 2014.
- [11] J. C. Lam, D. H. Li, and S. Cheung, “An analysis of electricity end-use in air-conditioned office buildings in hong kong,” *Building and Environment*, vol. 38, no. 3, pp. 493 – 498, 2003.

References

- [12] G. Lowry, "Energy saving claims for lighting controls in commercial buildings," *Energy and Buildings*, vol. 133, no. Supplement C, pp. 489 – 497, 2016.
- [13] A. Williams, B. Atkinson, K. Garbesi, F. Rubinstein, and E. Page, "A meta-analysis of energy savings from lighting controls in commercial buildings," tech. rep., Ernest Orlando Lawrence Berkeley National Laboratory, Berkeley, CA (US), 2011.
- [14] S. N. Kamaruzzaman, R. Edwards, E. M. A. Zawawi, and A. I. Che-Ani, "Achieving energy and cost savings through simple daylighting control in tropical historic buildings," *Energy and Buildings*, vol. 90, no. Supplement C, pp. 85 – 93, 2015.
- [15] D. Salem and E. Elwakil, "Daylighting-based assessment of occupant performance in educational buildings," *Journal of Professional Issues in Engineering Education and Practice*, vol. 143, no. 1, p. 04016014, 2017.
- [16] A. Tsangrassoulis, A. Kontadakis, and L. Doulos, "Assessing lighting energy saving potential from daylight harvesting in office buildings based on code compliance & simulation techniques: A comparison," *Procedia Environmental Sciences*, vol. 38, pp. 420 – 427, 2017. Sustainable synergies from Buildings to the Urban Scale.
- [17] J. Huang, J. Hanford, and F. Yang, *Residential heating and cooling loads component analysis*. Building Technologies Department, Environmental Energy Technologies Division, 1999.
- [18] Y. F. Lian, "Lighting energy-saving design for industrial factory building," in *Green Power, Materials and Manufacturing Technology and Applications III*, vol. 484 of *Applied Mechanics and Materials*, pp. 737–741, Trans Tech Publications, 3 2014.
- [19] S. Chun, C.-S. Lee, and J.-S. Jang, "Real-time smart lighting control using human motion tracking from depth camera," *Journal of Real-Time Image Processing*, vol. 10, pp. 805–820, Dec 2015.
- [20] L. Song and G. Y. Yao, "Design of library lighting energy saving system based on internet of things," in *Frontiers of Manufacturing and Design Science IV*, vol. 496 of *Applied Mechanics and Materials*, pp. 1690–1693, Trans Tech Publications, 4 2014.
- [21] J. Liu, W. Zhang, X. Chu, and Y. Liu, "Fuzzy logic controller for energy savings in a smart led lighting system considering lighting comfort and daylight," *Energy and Buildings*, vol. 127, no. Supplement C, pp. 95 – 104, 2016.
- [22] M. Wei and S. Chen, "Impact of spectral power distribution of daylight simulators on whiteness specification for surface colors," *Color Research & Application*, vol. 43, no. 1, pp. 27–33, 2018.
- [23] S. M. Pauley, "Lighting for the human circadian clock: recent research indicates that lighting has become a public health issue," *Medical Hypotheses*, vol. 63, no. 4, pp. 588 – 596, 2004.

-
- [24] C. Cajochen, "Alerting effects of light," *Sleep Medicine Reviews*, vol. 11, no. 6, pp. 453 – 464, 2007.
- [25] M. Andersen, S. J. Gochenour, and S. W. Lockley, "Modelling 'non-visual' effects of daylighting in a residential environment," *Building and Environment*, vol. 70, no. Supplement C, pp. 138 – 149, 2013.
- [26] M. L. Amundadottir, S. Rockcastle, M. S. Khanie, and M. Andersen, "A human-centric approach to assess daylight in buildings for non-visual health potential, visual interest and gaze behavior," *Building and Environment*, vol. 113, no. Supplement C, pp. 5 – 21, 2017. Advances in daylighting and visual comfort research.
- [27] R. G. Stevens, D. E. Blask, G. C. Brainard, J. Hansen, S. W. Lockley, I. Provencio, M. S. Rea, and L. Reinlib, "Meeting report: the role of environmental lighting and circadian disruption in cancer and other diseases," *Environmental health perspectives*, vol. 115, no. 9, p. 1357, 2007.
- [28] G. Costa, "The impact of shift and night work on health," *Applied Ergonomics*, vol. 27, no. 1, pp. 9 – 16, 1996. Shiftwork.
- [29] S. S. Intille, "Designing a home of the future," *IEEE pervasive computing*, vol. 1, no. 2, pp. 76–82, 2002.
- [30] M. Hillman and J. Parker, "More daylight, less electricity," *Energy Policy*, vol. 16, no. 5, pp. 514 – 515, 1988.
- [31] T. Sarver, A. Al-Qaraghuli, and L. L. Kazmerski, "A comprehensive review of the impact of dust on the use of solar energy: History, investigations, results, literature, and mitigation approaches," *Renewable and Sustainable Energy Reviews*, vol. 22, pp. 698 – 733, 2013.
- [32] J. Strømman-Andersen and P. Sattrup, "The urban canyon and building energy use: Urban density versus daylight and passive solar gains," *Energy and Buildings*, vol. 43, no. 8, pp. 2011 – 2020, 2011.
- [33] J. Mardaljevic, L. Heschong, and E. Lee, "Daylight metrics and energy savings," *Lighting Research & Technology*, vol. 41, no. 3, pp. 261–283, 2009.
- [34] L. Sanati and M. Utzinger, "The effect of window shading design on occupant use of blinds and electric lighting," *Building and Environment*, vol. 64, no. Supplement C, pp. 67 – 76, 2013.
- [35] M. Wigginton and M. Pidgeon, *Glass in architecture*. Phaidon London, UK, March 1996.
- [36] M.-C. Dubois and Åke Blomsterberg, "Energy saving potential and strategies for electric lighting in future north european, low energy office buildings: A literature review," *Energy and Buildings*, vol. 43, no. 10, pp. 2572 – 2582, 2011.

References

- [37] “Lighting energy savings potential of split-pane electrochromic windows controlled for daylighting with visual comfort,” *Energy and Buildings*, vol. 61, pp. 8 – 20, 2013.
- [38] K. Konis, “Evaluating daylighting effectiveness and occupant visual comfort in a side-lit open-plan office building in san francisco, california,” *Building and Environment*, vol. 59, pp. 662 – 677, 2013.
- [39] M. Velds, “User acceptance studies to evaluate discomfort glare in daylit rooms,” *Solar Energy*, vol. 73, no. 2, pp. 95–103, 2002.
- [40] A. Borisuit, F. Linhart, J.-L. Scartezzini, and M. Münch, “Effects of realistic office daylighting and electric lighting conditions on visual comfort, alertness and mood,” *Lighting Research & Technology*, vol. 47, no. 2, pp. 192–209, 2015.
- [41] P. D. Gamlin, D. H. McDougal, J. Pokorny, V. C. Smith, K.-W. Yau, and D. M. Dacey, “Human and macaque pupil responses driven by melanopsin-containing retinal ganglion cells,” *Vision research*, vol. 47, no. 7, pp. 946–954, 2007.
- [42] P. Khademagha, M. Aries, A. Rosemann, and E. van Loenen, “Implementing non-image-forming effects of light in the built environment: A review on what we need,” *Building and Environment*, vol. 108, pp. 263–272, 2016.
- [43] J. McArthur, C. Jofeh, and A.-M. Aguilar, “Improving occupant wellness in commercial office buildings through energy conservation retrofits,” *Buildings*, vol. 5, no. 4, pp. 1171–1186, 2015.
- [44] F. Beute and Y. A. de Kort, “Salutogenic effects of the environment: Review of health protective effects of nature and daylight,” *Applied Psychology: Health and Well-Being*, vol. 6, no. 1, pp. 67–95, 2014.
- [45] B. Thayer, “Daylighting and productivity at lockheed,” *Solar Today*, vol. 9, no. 3, pp. 26–29, 1995.
- [46] G. Kats, *Green building costs and financial benefits*. Massachusetts Technology Collaborative Boston, 2003.
- [47] S. Tom, “Managing energy and comfort,” *ASHRAE Journal*, vol. 50, no. 6, pp. 18–27, 2008.
- [48] Y. Al Horr, M. Arif, A. Kaushik, A. Mazroei, M. Katafygiotou, and E. Elsarrag, “Occupant productivity and office indoor environment quality: A review of the literature,” *Building and environment*, vol. 105, pp. 369–389, 2016.
- [49] Comité Européen de Normalisation, “En 12464-1: Light and lighting-lighting of work places, part 1: Indoor work places,” *Brussels: CEN*, 2002.
- [50] Comité Européen de Normalisation, “prEN 17037: Daylight of buildings,” *Brussels: CEN*, 2016.

-
- [51] C. F. Reinhart and K. Voss, "Monitoring manual control of electric lighting and blinds," *Lighting research & technology*, vol. 35, no. 3, pp. 243–258, 2003.
- [52] K. Konis, "Predicting visual comfort in side-lit open-plan core zones: results of a field study pairing high dynamic range images with subjective responses," *Energy and Buildings*, vol. 77, pp. 67–79, 2014.
- [53] J. Wienold and J. Christoffersen, "Evaluation methods and development of a new glare prediction model for daylight environments with the use of ccd cameras," *Energy and buildings*, vol. 38, no. 7, pp. 743–757, 2006.
- [54] R. G. Hopkinson, "Glare from daylighting in buildings," *Applied Ergonomics*, vol. 3, no. 4, pp. 206–215, 1972.
- [55] Commission Internationale de l'Eclairage, "Discomfort glare in interior lighting," CIE, 1995.
- [56] S. K. Guth, "A method for the evaluation of discomfort glare," *Illuminating Engineering*, vol. 58, no. 5, pp. 351–364, 1963.
- [57] T. IWATA, M. TOKURA, M. SHUKUYA, and K.-i. KIMURA, "Experimental study on discomfort glare caused by windows part 2: Subjective response to glare from actual windows," *Journal of Architecture, Planning and Environmental Engineering (Transactions of AIJ)*, vol. 439, pp. 19–31, 1992.
- [58] Y. Inoue, "Methodological study of dynamic evaluation for discomfort glare," *Journal of Architecture, Planning and Environmental Engineering*, vol. 398, pp. 9–18, 1989.
- [59] A. Mahić, K. Galicinao, and K. Van Den Wymelenberg, "A pilot daylighting field study: Testing the usefulness of laboratory-derived luminance-based metrics for building design and control," *Building and Environment*, vol. 113, pp. 78–91, 2017.
- [60] I. Konstantzos, A. Tzempelikos, and Y.-C. Chan, "Experimental and simulation analysis of daylight glare probability in offices with dynamic window shades," *Building and Environment*, vol. 87, pp. 244 – 254, 2015.
- [61] J. Y. Suk, M. Schiler, and K. Kensek, "Development of new daylight glare analysis methodology using absolute glare factor and relative glare factor," *Energy and Buildings*, vol. 64, pp. 113–122, 2013.
- [62] K. V. D. Wymelenberg and M. Inanici, "A critical investigation of common lighting design metrics for predicting human visual comfort in offices with daylight," *LEUKOS*, vol. 10, no. 3, pp. 145–164, 2014.
- [63] S. Carlucci, F. Causone, F. De Rosa, and L. Pagliano, "A review of indices for assessing visual comfort with a view to their use in optimization processes to support building integrated design," *Renewable and sustainable energy reviews*, vol. 47, pp. 1016–1033, 2015.

References

- [64] J. Y. Suk, "Luminance and vertical eye illuminance thresholds for occupants' visual comfort in daylight office environments," *Building and Environment*, 2018.
- [65] W. O'Brien, K. Kapsis, and A. K. Athienitis, "Manually-operated window shade patterns in office buildings: A critical review," *Building and Environment*, vol. 60, pp. 319 – 338, 2013.
- [66] K. Anderson, *Design energy simulation for architects: Guide to 3D graphics*. Routledge, 2014.
- [67] Griesser [Digital image], "Retrieved from <https://www.griesser.ch/en/home>," 2019.
- [68] CrosbyBlinds [Digital image], "Retrieved from <http://www.crosbyblinds.co.uk>," 2019.
- [69] R. French, *Venetian blinds : A survey of the foundation and development of the Venetian blind, its uses, advantages and applications together with the modern modus operandi of manufacture and selling, copiously illustrated : A standard text book for the furnishing and blind-making trades*. Manchester: Thomas French & Sons Limited, 1941.
- [70] F. Nasrollahi, *Climate and Energy Responsive Housing in Continental Climates: The Suitability of Passive Houses for Iran's Dry and Cold Climate*. Univerlag tuberlin, 2009.
- [71] B. Paule, J. Boutillier, and S. Pantet, "Global lighting performance," tech. rep., Swiss Federal Office of Energy, 2014.
- [72] V. Gavan, M. Woloszyn, F. Kuznik, and J.-J. Roux, "Experimental study of a mechanically ventilated double-skin façade with venetian sun-shading device: A full-scale investigation in controlled environment," *Solar Energy*, vol. 84, no. 2, pp. 183 – 195, 2010.
- [73] J. Mardaljevic, R. K. Waskett, and B. Painter, "Electrochromic glazing in buildings: A case study," *Electrochromic Materials and Devices*, pp. 571–592, 2013.
- [74] J. Mardaljevic, R. Kelly Waskett, and B. Painter, "Neutral daylight illumination with variable transmission glass: Theory and validation," *Lighting Research & Technology*, vol. 48, no. 3, pp. 267–285, 2016.
- [75] C. M. Lampert, "Smart switchable glazing for solar energy and daylight control," *Solar Energy Materials and Solar Cells*, vol. 52, no. 3-4, pp. 207–221, 1998.
- [76] M. Moeck, E. S. Lee, M. D. Rubin, R. Sullivan, and S. E. Selkowitz, "Visual quality assessment of electrochromic and conventional glazings," in *SPIE Optical Materials Technology for Energy Efficiency and Solar Energy Conversion XV*, (Freiburg, Germany), 09/1996 1996.
- [77] E. Lee and D. DiBartolomeo, "Application issues for large-area electrochromic windows in commercial buildings," *Solar Energy Materials and Solar Cells*, vol. 71, no. 4, pp. 465 – 491, 2002.

- [78] D. Stekovic, B. Arkook, G. Li, W. Li, E. Bekyarova, and M. E. Itkis, "High modulation speed, depth, and coloration efficiency of carbon nanotube thin film electrochromic device achieved by counter electrode impedance matching," *Advanced Materials Interfaces*, vol. 5, no. 20, p. 1800861, 2018.
- [79] P. C. da Silva, V. Leal, and M. Andersen, "Influence of shading control patterns on the energy assessment of office spaces," *Energy and Buildings*, vol. 50, pp. 35 – 48, 2012.
- [80] V. Inkarojrit, "Monitoring and modelling of manually-controlled venetian blinds in private offices: a pilot study," *Journal of Building Performance Simulation*, vol. 1, no. 2, pp. 75–89, 2008.
- [81] A. Mahdavi and C. Pröglhöf, "User behavior and energy performance in buildings," *Wien, Austria: Internationalen Energiewirtschaftstagung an der TU Wien (IEWT)*, pp. 1–13, 2009.
- [82] C. F. Reinhart and S. Herkel, "The simulation of annual daylight illuminance distributions — a state-of-the-art comparison of six radiance-based methods," *Energy and Buildings*, vol. 32, no. 2, pp. 167 – 187, 2000.
- [83] J. Mardaljevic, *Daylight simulation: validation, sky models and daylight coefficients*. PhD thesis, © John Mardaljevic, 2000.
- [84] N. Igawa and H. Nakamura, "All sky model as a standard sky for the simulation of daylight environment," *Building and Environment*, vol. 36, no. 6, pp. 763 – 770, 2001. Building and Environmental Performance Simulation: Current State and Future Issues.
- [85] Y. Uetani, S. Aydinli, A. Joukoff, J. Kendrick, R. Kittler, Y. Koga, *et al.*, "Spatial distribution of daylight-cie standard general sky," *Vienna, Austria*, 2003.
- [86] R. Perez, R. Seals, and J. Michalsky, "All-weather model for sky luminance distribution—preliminary configuration and validation," *Solar energy*, vol. 50, no. 3, pp. 235–245, 1993.
- [87] A. H. Fakra, H. Boyer, F. Miranville, and D. Bigot, "A simple evaluation of global and diffuse luminous efficacy for all sky conditions in tropical and humid climate," *Renewable Energy*, vol. 36, no. 1, pp. 298–306, 2011.
- [88] CIE, Standard, "Spatial distribution of daylight-cie standard general sky," *CIE S 011.1/E*, 2003.
- [89] C. E. Shannon, "Communication in the presence of noise," *Proceedings of the IRE*, vol. 37, no. 1, pp. 10–21, 1949.
- [90] M. Inanici, "Evaluation of high dynamic range image-based sky models in lighting simulation," *The Journal of the Illuminating Engineering Society of North America*, vol. 7, no. 2, pp. 69–84, 2010.

References

- [91] G. C. Holst and T. S. Lomheim, *CMOS/CCD sensors and camera systems*, vol. 408. JCD publishing USA, 2007.
- [92] S. Borkar and A. A. Chien, “The future of microprocessors,” *Communications of the ACM*, vol. 54, no. 5, pp. 67–77, 2011.
- [93] J. Stumpfel, C. Tchou, A. Jones, T. Hawkins, A. Wenger, and P. Debevec, “Direct hdr capture of the sun and sky,” in *Proceedings of the 3rd international conference on Computer graphics, virtual reality, visualisation and interaction in Africa*, pp. 145–149, ACM, 2004.
- [94] D. Wüller and H. Gabele, “The usage of digital cameras as luminance meters,” in *Proc. SPIE 6502*, p. 65020U, Digital Photography III, 2007.
- [95] M. Moeck and S. Anaokar, “Illuminance analysis from high dynamic range images,” *Leukos*, vol. 2, no. 3, pp. 211–228, 2006.
- [96] A. Borisuit, M. Münch, L. Deschamps, J. Kämpf, and J.-L. Scartezzini, “A new device for dynamic luminance mapping and glare risk assessment in buildings,” in *Proc. of SPIE Vol*, vol. 8485, pp. 84850M–1, 2012.
- [97] A. Borisuit, J. Kämpf, M. Münch, A. Thanachareonkit, and J.-L. Scartezzini, “Monitoring and rendering of visual and photo-biological properties of daylight-redirecting systems,” *Solar Energy*, vol. 129, pp. 297–309, 2016.
- [98] A. Laouadi, “Thermal performance modelling of complex fenestration systems,” *Journal of Building Performance Simulation*, vol. 2, no. 3, pp. 189–207, 2009.
- [99] S. Vera, D. Uribe, W. Bustamante, and G. Molina, “Optimization of a fixed exterior complex fenestration system considering visual comfort and energy performance criteria,” *Building and Environment*, vol. 113, pp. 163–174, 2017.
- [100] A. Laouadi and A. Parekh, “Optical models of complex fenestration systems,” *Lighting Research & Technology*, vol. 39, no. 2, pp. 123–145, 2007.
- [101] C. Reinhart and A. Fitz, “Findings from a survey on the current use of daylight simulations in building design,” *Energy and Buildings*, vol. 38, no. 7, pp. 824–835, 2006.
- [102] A. Laouadi, C. F. Reinhart, and D. Bourgeois, “Efficient calculation of daylight coefficients for rooms with dissimilar complex fenestration systems,” *Journal of Building Performance Simulation*, vol. 1, no. 1, pp. 3–15, 2008.
- [103] M. Andersen, L. Michel, C. Roecker, and J.-L. Scartezzini, “Measurement of bi-directional photometric properties of advanced glazing based on digital imaging techniques,” *Proceedings Solar Energy in Buildings CISBAT’99*, pp. 45–50, 1999.
- [104] M. Andersen, C. Roecker, and J.-L. Scartezzini, “Design of a time-efficient video-goniophotometer combining bidirectional functions assessment for transmission and reflection,” *Solar Energy Materials and Solar Cells*, vol. 88, no. 1, pp. 97–118, 2005.

-
- [105] M. Andersen, M. Rubin, and J.-L. Scartezzini, "Comparison between ray-tracing simulations and bi-directional transmission measurements on prismatic glazing," *Solar Energy*, vol. 74, no. 2, pp. 157–173, 2003.
- [106] F. Bartell, E. Dereniak, and W. Wolfe, "The theory and measurement of bidirectional reflectance distribution function (brdf) and bidirectional transmittance distribution function (btdf)," in *Radiation scattering in optical systems*, vol. 257, pp. 154–161, International Society for Optics and Photonics, 1981.
- [107] CIE No. 86, "CIE 1988 2° spectral luminous efficiency function for photopic vision," (Vienna, Austria), International Commission on Illumination, 1990.
- [108] J. H. Klems and J. L. Warner, "Measurement of bidirectional optical properties of complex shading devices," *ASHRAE Transactions*, vol. 101, Part 1, 1995.
- [109] R. Chiabrando, E. Fabrizio, and G. Garnerò, "The territorial and landscape impacts of photovoltaic systems: Definition of impacts and assessment of the glare risk," *Renewable and Sustainable Energy Reviews*, vol. 13, no. 9, pp. 2441 – 2451, 2009.
- [110] R. D. Keyser and C. Ionescu, "Modelling and simulation of a lighting control system," *Simulation Modelling Practice and Theory*, vol. 18, no. 2, pp. 165 – 176, 2010.
- [111] E. S. Lee, D. Geisler-Moroder, and G. Ward, "Modeling the direct sun component in buildings using matrix algebraic approaches: Methods and validation," *Solar Energy*, vol. 160, pp. 380–395, 2018.
- [112] S. L. Chellappa, R. Steiner, P. Blattner, P. Oelhafen, T. Götz, and C. Cajochen, "Non-visual effects of light on melatonin, alertness and cognitive performance: can blue-enriched light keep us alert?," *PLOS ONE*, vol. 6, no. 1, p. e16429, 2011.
- [113] G. Ward, M. Kurt, and N. Bonneel, "A practical framework for sharing and rendering real-world bidirectional scattering distribution functions," tech. rep., Lawrence Berkeley National Lab.(LBNL), Berkeley, CA (United States), 2012.
- [114] P. Shirley and K. Chiu, "A low distortion map between disk and square," *Journal of graphics tools*, vol. 2, no. 3, pp. 45–52, 1997.
- [115] P. Schröder and W. Sweldens, "Spherical wavelets: Efficiently representing functions on the sphere," in *Proceedings of the 22nd annual conference on Computer graphics and interactive techniques*, pp. 161–172, ACM, 1995.
- [116] W. Sweldens, "The lifting scheme: A custom-design construction of biorthogonal wavelets," *Applied and computational harmonic analysis*, vol. 3, no. 2, pp. 186–200, 1996.
- [117] P. Lalonde and A. Fournier, "A wavelet representation of reflectance functions," *IEEE Transactions on Visualization and Computer Graphics*, vol. 3, no. 4, pp. 329–336, 1997.

References

- [118] A. D. Galasiu and J. A. Veitch, "Occupant preferences and satisfaction with the luminous environment and control systems in daylit offices: a literature review," *Energy and Buildings*, vol. 38, no. 7, pp. 728–742, 2006.
- [119] A. Tzempelikos and A. K. Athienitis, "The impact of shading design and control on building cooling and lighting demand," *Solar Energy*, vol. 81, no. 3, pp. 369 – 382, 2007.
- [120] T. INOUE, "The development of an optimal control system for window shading control system for window shading devices based on investigation in office buildings," *ASHRAE Transactions*, vol. 94, pp. 94–2, 1988.
- [121] E. Rubinstein, R. Verderber, and G. Ward, "Photoelectric control of daylighting systems," *Electric Power Research Institute, Final Report*, 1989.
- [122] E. Rubinstein, D. Avery, J. Jennings, and S. Blanc, "On the calibration and commissioning of lighting controls," in *Proceedings of the Right Light*, vol. 50, p. 207, 1997.
- [123] A. Guillemain and N. Morel, "Experimental results of a self-adaptive integrated control system in buildings: a pilot study," *Solar Energy*, vol. 72, no. 5, pp. 397–403, 2002.
- [124] J. Hu and S. Olbina, "Illuminance-based slat angle selection model for automated control of split blinds," *Building and Environment*, vol. 46, no. 3, pp. 786–796, 2011.
- [125] S. Y. Koo, M. S. Yeo, and K. W. Kim, "Automated blind control to maximize the benefits of daylight in buildings," *Building and Environment*, vol. 45, no. 6, pp. 1508–1520, 2010.
- [126] G. Newsham and C. Arsenault, "A camera as a sensor for lighting and shading control," *Lighting Research & Technology*, vol. 41, no. 2, pp. 143–163, 2009.
- [127] A. Motamed, L. Deschamps, and J.-L. Scartezzini, "On-site monitoring and subjective comfort assessment of a sun shadings and electric lighting controller based on novel high dynamic range vision sensors," *Energy and Buildings*, vol. 149, pp. 58–72, 2017.
- [128] T. E. Kuhn, "Solar control: Comparison of two new systems with the state of the art on the basis of a new general evaluation method for facades with venetian blinds or other solar control systems," *Energy and Buildings*, vol. 38, no. 6, pp. 661–672, 2006.
- [129] L. Karlsen, P. Heiselberg, and I. Bryn, "Occupant satisfaction with two blind control strategies: Slats closed and slats in cut-off position," *Solar Energy*, vol. 115, pp. 166–179, 2015.
- [130] C. Goovaerts, F. Descamps, and V. Jacobs, "Shading control strategy to avoid visual discomfort by using a low-cost camera: A field study of two cases," *Building and Environment*, vol. 125, pp. 26–38, 2017.
- [131] Y.-C. Chan and A. Tzempelikos, "Efficient venetian blind control strategies considering daylight utilization and glare protection," *Solar Energy*, vol. 98, pp. 241–254, 2013.

- [132] L. Bellia, F. Fragliasso, and E. Stefanizzi, "Why are daylight-linked controls (dlcs) not so spread? a literature review," *Building and Environment*, vol. 106, pp. 301–312, 2016.
- [133] A. Tzempelikos and A. K. Athienitis, "The impact of shading design and control on building cooling and lighting demand," *Solar energy*, vol. 81, no. 3, pp. 369–382, 2007.
- [134] R. Sullivan, E. S. Lee, K. Papamichael, M. Rubin, and S. E. Selkowitz, "Effect of switching control strategies on the energy performance of electrochromic windows," in *Optical Materials Technology for Energy Efficiency and Solar Energy Conversion XIII*, vol. 2255, pp. 443–456, International Society for Optics and Photonics, 1994.
- [135] J. Karlsson, B. Karlsson, and A. Roos, "Control strategies and energy saving potentials for variable transmittance windows versus static windows," *Proc. of Eurosun, Copenhagen, Denmark*, 2000.
- [136] E. Lee, D. DiBartolomeo, and S. Selkowitz, "Daylighting control performance of a thin-film ceramic electrochromic window: Field study results," *Energy and Buildings*, vol. 38, no. 1, pp. 30–44, 2006.
- [137] A. Jonsson and A. Roos, "Evaluation of control strategies for different smart window combinations using computer simulations," *Solar Energy*, vol. 84, no. 1, pp. 1–9, 2010.
- [138] F. Gugliermetti and F. Bisegna, "Visual and energy management of electrochromic windows in mediterranean climate," *Building and Environment*, vol. 38, no. 3, pp. 479–492, 2003.
- [139] A. Piccolo and F. Simone, "Effect of switchable glazing on discomfort glare from windows," *Building and Environment*, vol. 44, no. 6, pp. 1171–1180, 2009.
- [140] A. A. Nazzal, "A new daylight glare evaluation method: Introduction of the monitoring protocol and calculation method," *Energy and Buildings*, vol. 33, no. 3, pp. 257–265, 2001.
- [141] W. K. Osterhaus and I. L. Bailey, "Large area glare sources and their effect on visual discomfort and visual performance at computer workstations," in *Industry Applications Society Annual Meeting, 1992., Conference Record of the 1992 IEEE*, pp. 1825–1829, IEEE, 1992.
- [142] R. Clear, V. Inkarojrit, and E. Lee, "Subject responses to electrochromic windows," *Energy and Buildings*, vol. 38, no. 7, pp. 758–779, 2006.
- [143] L. Fernandes, E. S. Lee, and G. Ward, "Lighting energy savings potential of split-pane electrochromic windows controlled for daylighting with visual comfort," *Energy and Buildings*, vol. 61, pp. 8–20, 2013.
- [144] L. L. Fernandes, E. S. Lee, and A. Thanachareonkit, "Electrochromic window demonstration at the donna land port of entry," tech. rep., 05/2015 2015.

References

- [145] Y. Wu, J. H. Kämpf, and J.-L. Scartezzini, "Design and validation of a compact embedded photometric device for real-time daylighting computing in office buildings," *Building and Environment*, vol. 148, pp. 309–322, 2019.
- [146] S. A. Green and D. J. Paddon, "Exploiting coherence for multiprocessor ray tracing," *IEEE Computer Graphics and Applications*, vol. 9, pp. 12–26, Nov 1989.
- [147] T. Perhavec, A. Gorkič, D. Bračun, and J. Diaci, "A method for rapid measurement of laser ablation rate of hard dental tissue," *Optics & Laser Technology*, vol. 41, no. 4, pp. 397–402, 2009.
- [148] R. S. Reyes, C. M. Oppus, J. C. N. Monje, N. S. Patron, R. C. Guerrero, and J. T. B. Fajardo, "Fpga implementation of a telecommunications trainer system," *International Journal of Circuits, Systems and Signal Processing*, vol. 2, no. 2, pp. 174–180, 2008.
- [149] P. J. Pingree, J.-F. L. Blavier, G. C. Toon, and D. L. Bekker, "An fpga/soc approach to on-board data processing enabling new mars science with smart payloads," in *Aerospace Conference, 2007 IEEE*, pp. 1–12, IEEE, 2007.
- [150] A. D. Broadbent, "A critical review of the development of the cie1931 rgb color-matching functions," *Color Research & Application*, vol. 29, no. 4, pp. 267–272, 2004.
- [151] T. Poikonen, P. Kärhä, P. Manninen, F. Manoocheri, and E. Ikonen, "Uncertainty analysis of photometer quality factor," *Metrologia*, vol. 46, no. 1, p. 75, 2008.
- [152] Commission Internationale de l'Eclairage, "Methods of characterizing illuminance meters and luminance meters: Performance, characteristics and specifications," *Publication CIE*, pp. 69–1987, 1987.
- [153] DIN 5032 part 7, "Lichtmessung-klasseneinteilung von beleuchtungsstärke- und leuchtdichtemessgeräten [photometry: classification of illuminance meters and luminance meters." Deutsches Institut für Normung e.V., Dec 1985.
- [154] D. B. Goldman and J.-H. Chen, "Vignette and exposure calibration and compensation," in *Computer Vision, 2005. ICCV 2005. Tenth IEEE International Conference on*, vol. 1, pp. 899–906, IEEE, 2005.
- [155] G. W. Larson and R. Shakespeare, *Rendering with Radiance: the art and science of lighting visualization*. Booksurge Llc, 2004.
- [156] P. R. Tregenza, "Subdivision of the sky hemisphere for luminance measurements," *Lighting Research & Technology*, vol. 19, no. 1, pp. 13–14, 1987.
- [157] S. Darula, R. Kittler, and C. A. Gueymard, "Reference luminous solar constant and solar luminance for illuminance calculations," *Solar Energy*, vol. 79, no. 5, pp. 559–565, 2005.
- [158] R. Szeliski, *Computer vision: algorithms and applications*. Springer Science & Business Media, 2010.

- [159] D. L. DiLaura, K. W. Houser, R. G. Mistrick, and G. R. Steffy, *The lighting handbook: Reference and application*. Illuminating Engineering Society of North America New York (NY), 2011.
- [160] A. McNeil, “The five-phase method for simulating complex fenestration with radiance,” *Lawrence Berkeley National Laboratory, Berkeley, CA, USA*, pp. 1–23, 2013.
- [161] C. B. R. Ferreira and D. L. Borges, “Analysis of mammogram classification using a wavelet transform decomposition,” *Pattern Recognition Letters*, vol. 24, no. 7, pp. 973–982, 2003.
- [162] A. S. Lewis and G. Knowles, “Image compression using the 2-d wavelet transform,” *IEEE Transactions on image Processing*, vol. 1, no. 2, pp. 244–250, 1992.
- [163] I. Daubechies, “The wavelet transform, time-frequency localization and signal analysis,” *IEEE transactions on information theory*, vol. 36, no. 5, pp. 961–1005, 1990.
- [164] I. Daubechies, *Ten lectures on wavelets*. SIAM, 1992.
- [165] M. Vetterli and J. Kovačević, *Wavelets and subband coding*. Citeseer, 2007.
- [166] R. W. Hamming, *Coding and Theory*. Prentice-Hall, 1980.
- [167] I. Daubechies, “Orthonormal bases of compactly supported wavelets,” *Communications on pure and applied mathematics*, vol. 41, no. 7, pp. 909–996, 1988.
- [168] A. Cohen, I. Daubechies, and P. Vial, “Wavelets on the interval and fast wavelet transforms,” *Applied and computational harmonic analysis*, vol. 1, no. 1, pp. 54–81, 1993.
- [169] P. N. Heller, “Rank m wavelets with n vanishing moments,” *SIAM Journal on Matrix Analysis and Applications*, vol. 16, no. 2, pp. 502–519, 1995.
- [170] M. Andersen, “Validation of the performance of a new bidirectional video-goniophotometer,” *Lighting Research & Technology*, vol. 38, no. 4, pp. 295–311, 2006.
- [171] F. Linhart and J.-L. Scartezzini, “Evening office lighting–visual comfort vs. energy efficiency vs. performance?,” *Building and Environment*, vol. 46, no. 5, pp. 981–989, 2011.
- [172] J. Wienold, “Dynamic daylight glare evaluation,” in *Proceedings of Building Simulation*, pp. 944–951, 2009.
- [173] P. Debevec and S. Gibson, “A tone mapping algorithm for high contrast images,” in *13th Eurographics Workshop on Rendering: Pisa, Italy*, Citeseer, 2002.
- [174] Commission Internationale de l’Eclairage, “CIE Proceedings 1924,” 1926.
- [175] J. Jakubiec and C. Reinhart, “Diva-for-rhino 2.0: Environmental parametric modeling in rhinoceros/grasshopper using radiance, daysim and energyplus,” in *Conference proceedings of building simulation*, 2011.

References

- [176] J. H. Klems and J. L. Warner, "Measurement of bidirectional optical properties of complex shading devices," *ASHRAE Transactions*, vol. 101-1, 1995.
- [177] G. Ward, R. Mistrick, E. S. Lee, A. McNeil, and J. Jonsson, "Simulating the daylight performance of complex fenestration systems using bidirectional scattering distribution functions within radiance," *Leukos*, vol. 7, no. 4, pp. 241–261, 2011.
- [178] Y. Wu, J. H. Kämpf, and J.-L. Scartezzini, "An embedded system for quasi real-time lighting computation based on sky monitoring," in *Building Simulation*, IBPSA San Francisco, California, 2017.
- [179] Y. Wu, J. H. Kämpf, and J.-L. Scartezzini, "Daylighting simulation for external venetian blinds based on hdr sky luminance monitoring with matrix algebraic approach," in *The 10th International Conference on Applied Energy*, (Hong Kong, China), ICAE2018, Aug. 22-25 2018.
- [180] Y. Wu, J. H. Kämpf, and J.-L. Scartezzini, "Lighting simulation for external venetian blinds based on btdf and hdr sky luminance monitoring," in *7th International Building Physics Conference*, (Syracuse, NY, USA), IBPC2018, Sept. 23-26 2018.
- [181] M. T. Imam, J. Gleason, S. Mishra, and M. Oishi, "Estimation of solar heat gain using illumination sensor measurements," *Solar Energy*, vol. 174, pp. 296 – 304, 2018.
- [182] G. W. Larson and R. Shakespeare, *Rendering with Radiance: the art and science of lighting visualization*. Booksurge Llc, 2004.
- [183] M. Pharr, W. Jakob, and G. Humphreys, *Physically based rendering: From theory to implementation*. Morgan Kaufmann, 2016.
- [184] A. Nabil and J. Mardaljevic, "Useful daylight illuminance: a new paradigm for assessing daylight in buildings," *Lighting Research & Technology*, vol. 37, no. 1, pp. 41–57, 2005.

WU Yujie

Personal Details:

Gender: Male

Nationality: China

Email: yujie.wu@epfl.ch or wuyujiefreddy@gmail.com Phone: +41 789 32 42 85

Language: Chinese (native language), English (full professional proficiency), French (basic)

Address: LE 2 200, LESO-PB, EPFL, Station 18, CH-1015 Lausanne, Switzerland

Academic Background

- 03/2015-04/2019 **PhD** student at Solar Energy and Building Physics Laboratory,
Department of Energy, **EPFL** (Switzerland)
Research field: Automated shading system
- 07/2018-11/2018 **Visiting** Researcher at Building Technologies and Urban Systems Division,
Lawrence Berkeley National Laboratory (**LBNL**), Berkeley, CA, USA
- 01/2014-01/2015 Research **Assistant** with Prof. Richard Syms,
Department of Electrical and Electronic Engineering,
Imperial College London (UK)
- 09/2012-09/2013 **MSc** in Analog and Digital Integrated Circuit Design (with **Distinction**)
Department of Electrical and Electronic Engineering (GPA: 3.78/4.0)
Imperial College London (UK)
- 09/2007-06/2011 **BSc** in Measuring and Testing Technology & Instruments (**Top 6.3%**)
School of Optoelectronic Engineering, *Chongqing University* (China)

Honors & Awards

1. **First Prize** in National High School Mathematical Olympiad (2006, Equivalent rate: top 1/5000)
2. “**Excellent Student** of Optoelectronic Engineering School” Award (2008)
3. The BMW China Song Ching Ling Foundation **Scholarship** (2009)
4. **Outstanding Individual** of Youth Volunteer Award of the Chongqing City (2010, State Level)
5. Departmental Fees **Scholarship** from Imperial College London (2013, for 3 years)
6. Doctoral Exchange Grant from Zeno Karl Schindler Foundation (2018)

Journal Publication:

1. **Yujie Wu** ; J. H. Kämpf; J. Scartezzini : Design and Validation of a Compact Embedded Photometric Device for Real-time Daylighting Computing in Office Buildings; *Building and Environment*. 148 (2019) 309-32. <https://doi.org/10.1016/j.buildenv.2018.11.016> 167

2. Shenjun Zhu, Jiamin Liu, Zhaochun Qiu, Wenhao Xiong, **Yujie Wu**, Ear Edge Detection in Complex Background Based on Wavelet Modulus Maxima, 2009, Chinese Journal of Lasers 0258-7025 (Supplement 2-0158-05)

Conference in Proceedings:

1. **Yujie Wu** ; J. H. Kämpf; J. Scartezzini: “Lighting simulation for External Venetian blinds based on BTDF and HDR sky luminance monitoring”, 7th International Building Physics Conference, IBPC2018, Syracuse, NY, USA, Sept. 23-26, 2018.
2. **Yujie Wu** ; J. H. Kämpf; J. Scartezzini: “Daylighting simulation for external Venetian blinds based on HDR sky luminance monitoring with matrix algebraic approach”, The 10th International Conference on Applied Energy, ICAE2018, Hongkong, China, Aug. 22-25, 2018.
3. **Yujie Wu**, J. H. Kämpf and J.-L. Scartezzini, An Embedded System for Quasi Real-time Lighting Computation based on Sky Monitoring, 15th IBPSA Building Simulation 2017, San Francisco, USA, August 7-9, 2017
4. **Yujie Wu**, J. H. Kämpf and J.-L. Scartezzini, Characterization of a quasi-real-time lighting computation system based on HDR imaging, CISBAT 2017, Lausanne, Switzerland, September 6-8, 2017

Patents:

1. **Yujie Wu**, J. H. Kämpf and J.-L. Scartezzini, Sky Monitoring System (PCT/IB2018/055889, pending)
2. **Yujie Wu**, J. H. Kämpf and J.-L. Scartezzini, Shading Device (Patent, pending)

